



Investigation of megakaryopoiesis and the acute phase of ischemic stroke by advanced fluorescence microscopy

Untersuchungen der Megakaryopoese und der akuten Phase des ischämischen Schlaganfalls mit Hilfe von hochentwickelter Fluoreszenzmikroskopie

Doctoral thesis for a doctoral degree
at the Graduate School of Life Sciences,
Julius-Maximilians-Universität Würzburg,
Section Biomedicine

submitted by

Maximilian Georg Gorelashvili

from Kutaisi, Georgia

Würzburg 2018

Submitted on:

Members of the *Promotionskomitee*:

Chairperson:	Prof. Dr. Alma Zerneck-Madsen
Primary supervisor:	Dr. David Stegner
Supervisor (Second):	Prof. Dr. Katrin Heinze
Supervisor (Third):	Prof. Dr. Guido Stoll
Supervisor (Fourth):	Prof. Dr. Bernhard Nieswandt

Date of Public Defense:

Date of Receipt of Certificates:

"Dubium sapientiae initium."

René Descartes

Summary

In mammals, anucleate platelets circulate in the blood flow and are primarily responsible for maintaining functional hemostasis. Platelets are generated in the bone marrow (BM) by megakaryocytes (MKs), which mainly reside directly next to the BM sinusoids to release proplatelets into the blood. MKs originate from hematopoietic stem cells and are thought to migrate from the endosteal to the vascular niche during their maturation, a process, which is, despite being intensively investigated, still not fully understood.

Long-term intravital two photon microscopy (2PM) of MKs and vasculature in murine bone marrow was performed and mean squared displacement analysis of cell migration was performed. The MKs exhibited no migration, but wobbling-like movement on time scales of 3 h. Directed cell migration always results in non-random spatial distribution. Thus, a computational modelling algorithm simulating random MK distribution using real 3D light-sheet fluorescence microscopy data sets was developed. Direct comparison of real and simulated random MK distributions showed, that MKs exhibit a strong bias to vessel-contact. However, this bias is not caused by cell migration, as non-vessel-associated MKs were randomly distributed in the intervascular space. Furthermore, simulation studies revealed that MKs strongly impair migration of other cells in the bone marrow by acting as large-sized obstacles. MKs are thought to migrate from the regions close to the endosteum towards the vasculature during their maturation process. MK distribution as a function of their localization relative to the endosteal regions of the bones was investigated by light sheet fluorescence microscopy (LSFM). The results show no bone-region dependent distribution of MKs. Taken together, the newly established methods and obtained results refute the model of MK migration during their maturation.

Ischemia reperfusion (I/R) injury is a frequent complication of cerebral ischemic stroke, where brain tissue damage occurs despite successful recanalization. Platelets, endothelial cells and immune cells have been demonstrated to affect the progression of I/R injury in experimental mouse models 24 h after recanalization. However, the underlying Pathomechanisms, especially in the first hours after recanalization, are poorly understood.

Here, LSFM, 2PM and complementary advanced image analysis workflows were established for investigation of platelets, the vasculature and neutrophils in ischemic brains. Quantitative analysis of thrombus formation in the ipsilateral and contralateral hemispheres at different time points revealed that platelet aggregate formation is minimal during the first 8 h after recanalization and occurs in both hemispheres. Considering that maximal tissue damage already is present at this time point, it can be concluded that infarct progression and neurological damage do not result from platelet aggregated formation. Furthermore, LSFM allowed to confirm neutrophil infiltration into the infarcted hemisphere and, here, the levels of endothelial cell marker PECAM1 were strongly reduced. However, further investigations must be carried out to clearly identify the role of neutrophils and the endothelial cells in I/R injury.

Zusammenfassung

In Säugetieren zirkulieren kernlose Thrombozyten im Blutstrom und sind primär für die Aufrechterhaltung der funktionellen Hämostase verantwortlich. Thrombozyten werden im Knochenmark durch Megakaryozyten gebildet, die sich hauptsächlich in direkter Nähe zu Knochenmarkssinusoiden befinden, um Proplättchen in das Blut freizusetzen. Megakaryozyten stammen von hämatopoetischen Stammzellen ab und man glaubt, dass sie während ihres Reifungsprozesses von der endostalen in die vaskuläre Nische wandern – ein Prozess, der trotz intensiver Forschung noch nicht vollständig verstanden ist.

Langzeit-Zwei-Photonen-Mikroskopie von Megakaryozyten und des Gefäßbaums wurde in murinem Knochenmark von lebenden Tieren in Kombination mit der Analyse der mittleren quadratischen Verschiebung der Zellmigration durchgeführt. Die Megakaryozyten zeigten keine Migration, sondern eine wackelartige Bewegung auf Zeitskalen von 3 Stunden. Die gerichtete Zellmigration führt stets zu einer nicht zufälligen räumlichen Verteilung der Zellen. Daher wurde ein Computermodellierungsalgorithmus entwickelt, der eine zufällige Megakaryozytenverteilung unter Verwendung von realen 3D-Lichtblatt-Fluoreszenzmikroskopie-Datensätzen simuliert. Der direkte Vergleich realer und simuliert zufälliger Megakaryozytenverteilungen zeigte, dass MKs stark mit Knochenmarksgefäßen assoziiert sind. Dieses wird jedoch nicht durch Zellmigration verursacht, da nicht-Gefäß-assoziierte MKs zufällig im intervaskulären Raum verteilt waren. Darüber hinaus zeigten Simulationsstudien, dass Megakaryozyten die Migration anderer Zellen im Knochenmark stark beeinträchtigen, da sie als sterische Hindernisse wirken. Es wird angenommen, dass MKs während ihres Reifeprozesses von den Regionen in der Nähe des Endosteums in Richtung des Gefäßsystems wandern. Die Megakaryozytenverteilung als Funktion ihrer Lokalisierung relativ zu den endostalen Regionen des Knochens wurde durch Lichtblattmikroskopie untersucht. Die Ergebnisse zeigen keine knochenregionabhängige Verteilung von Megakaryozyten. Zusammengekommen widerlegen die neu etablierten Methoden und erzielten Ergebnisse das Modell der Megakaryozytenmigration während ihrer Reifung.

Ischämie-Reperfusionsschaden (I/R) ist eine häufige Komplikation des zerebralen ischämischen Schlaganfalls, bei dem trotz erfolgreicher Rekanalisierung eine Schädigung des Hirngewebes auftritt. Es wurde gezeigt, dass Thrombozyten, Endothelzellen und Immunzellen das Fortschreiten der I/R-Verletzung in experimentellen Mausmodellen 24 Stunden nach der Rekanalisierung beeinflussen. Die zugrundeliegenden Pathomechanismen, insbesondere in den ersten Stunden nach der Rekanalisierung, sind jedoch kaum verstanden.

Hier wurden Lichtblattmikroskopie, Zwei-Photonen-Mikroskopie und ergänzende hochkomplexe Bildanalyse-Workflows zur Untersuchung von Thrombozyten, der Gefäße und Neutrophilen in ischämischen Gehirnen etabliert. Die quantitative Analyse der Thrombusbildung in der ipsilateralen und kontralateralen Hemisphäre zu verschiedenen Zeitpunkten zeigte, dass

die Thrombozytenaggregationsbildung während der ersten 8 Stunden nach der Rekanalisierung minimal ist und in beiden Hemisphären auftritt. In Anbetracht dessen, dass zu diesem Zeitpunkt bereits eine maximale Gewebeschädigung vorliegt, kann geschlossen werden, dass die Infarktprogression und der neurologische Schaden nicht aus der Bildung von Thrombozytenaggregaten resultieren. Darüber hinaus erlaubte Lichtblattemikroskopie die Neutrophileninfiltration in die infarzierte Hemisphäre zu bestätigen und hier waren die Spiegel des Endothelzellmarkers PECAM1 stark reduziert. Es müssen jedoch weitere Untersuchungen durchgeführt werden, um die Rolle von Neutrophilen und Endothelzellen bei I/R-Verletzungen klar zu identifizieren.

Table of Content

1	Introduction	1
1.1	Hematopoietic stem cells and bone marrow niches	1
1.2	Megakaryocytes and their development	3
1.3	Thrombopoiesis.....	6
1.4	Platelets	7
1.4.1	Platelet activation and thrombus formation.....	7
1.4.2	The role of platelets in inflammatory processes.....	10
1.5	Ischemic stroke and reperfusion injury	11
1.5.1	Brain anatomy and cerebral blood flow	11
1.5.2	Early phase of ischemic stroke and reperfusion injury in the brain	12
1.5.3	The role of platelets in the thrombo-inflammatory model of the acute phase of the reperfusion injury.....	14
1.5.4	The role of immune cells and the endothelial cells in the acute phase of the reperfusion injury.....	16
1.6	Advanced fluorescence imaging techniques.....	18
1.6.1	Two-photon intravital microscopy	18
1.6.2	Optical clearing methods.....	20
1.6.3	Light sheet fluorescence microscopy.....	21
2	Aim of the study	24
3	Materials and methods	25
3.1	Materials	25
3.1.1	Reagents and chemicals	25
3.1.2	Materials	26
3.1.3	Labeling kits and fluorophores.....	26
3.1.4	Antibodies	26
3.1.5	Buffers and solutions.....	27
3.1.6	Mice	28
3.1.7	Software.....	29
3.2	Methods	29
3.2.1	Mouse genotyping by PCR.....	29
3.2.2	Transient middle cerebral artery occlusion (tMCAO)	31
3.2.3	Mouse preparation for intravital imaging.....	31
3.2.4	Intravital imaging of mice by multi-photon microscopy.....	32
3.2.5	Light sheet fluorescence microscopy (LSFM) of cleared tissue	33

3.2.6	Image preprocessing, segmentation and quantitative analysis	34
3.2.7	Statistical analysis	36
4	Results	37
4.1	Investigation of megakaryocyte presence, migration and spatial distribution	37
4.1.1	Long-term intravital imaging of megakaryocyte motility	37
4.1.2	Investigation of megakaryocyte distribution in the bone marrow by computational modelling.....	40
4.1.3	Quantitative analysis of megakaryocyte distribution throughout the bone in different bone types.....	46
4.1.4	Megakaryocytes in the murine lung	50
4.1.5	Impact of MKs on cell migration in the bone marrow in simulation studies.....	51
4.2	Investigation of ischemic stroke and reperfusion injury	57
4.2.1	Investigation of thrombus formation during I/R injury	57
4.2.2	Investigation of the early phase of I/R injury after ischemic stroke.....	66
5	Discussion and outlook	74
5.1	Megakaryocyte distribution in the bone marrow.....	74
5.2	Thrombopoiesis in healthy pulmonary tissue	76
5.3	Microscopy and image processing techniques for investigation of ischemic stroke	77
5.4	Thrombus formation during the acute phase of I/R injury after ischemic stroke	79
5.5	Neutrophils and the endothelium in the acute phase of I/R injury	81
5.6	Future perspectives.....	83
6	References.....	86
7	Appendix	101
7.1	Abbreviations	101
7.2	Algorithm codes	106
7.2.1	Original algorithm code for static simulation of spatial cell distribution.....	106
7.2.2	Original algorithm code for dynamic simulation of cell migration.....	110
7.3	Acknowledgements	115
7.4	Publications.....	117
7.4.1	Original articles	117
7.4.2	Oral presentations.....	117
7.4.3	Poster presentations	117
7.5	Curriculum vitae	118

1 Introduction

1.1 Hematopoietic stem cells and bone marrow niches

Hematopoiesis is the process of forming blood cells. During this process, hematopoietic stem cells (HSCs) undergo lineage restriction and differentiate to restricted hematopoietic progenitors, which then give rise to blood cells by proliferation and further differentiation^{1,2}.

In healthy adult humans, HSCs mainly reside in the red bone marrow (BM) which is the primary site of hematopoiesis and which is mainly present in flat trabecular (spongy) bones such as cranium, sternum or ribs and in the epiphyseal parts of long bones. In mice, the red bone marrow is also present in the long bones, such as diaphysis of femora or tibiae, filling the entire marrow cavity. Oxygen and nutrient supply of the BM is provided by small arterioles, while the venous vasculature consists of a network of specialized bigger sinusoids of fenestrated structure, allowing intravasation or extravasation of different cells. At the interface of bone marrow and bone – the endosteum – arterioles and sinusoids are connected by transition zone vessels¹.

Within the bone marrow, the HSCs are localized in specialized niches as first proposed by Schofield in 1978³. Especially in the past five years, development of new HSC markers, genetically modified mouse strains and microscopy techniques enabled the identification and intensive investigation of the perivascular niche as the major site of HSC localization and activity, where 80% of HSCs were found to be associated with sinusoids, 10% with arterioles and further 10% with transition zone vessels⁴⁻⁷. Despite the common theory of endosteum-associated localization of HSCs proposed by Lord *et al.*⁸ decades ago, only a very small part of these cells could be found in close proximity of the bone¹. The perivascular niche has been determined to be a microenvironment containing different cell types and signaling molecules, together regulating HSC maintenance, quiescence, proliferation, differentiation and migration^{1,9-11}, but perisinusoidal and periarteriolar niches affect the HSC pool differently since oxygen tension, vessel wall permeability and cell intravasation capacity vary. Furthermore, perisinusoidal stromal cells surrounding the bone marrow sinusoid endothelial cells regulate the hematopoietic stem cell pool by expression of stem cell factor (SCF) and the C-X-C-chemokine ligand 12 (CXCL12), which directly interact with SCF receptor (SCFR)/c-Kit and C-X-C-chemokine receptor type 4 (CXCR4) on the HSCs^{1,9}. Inhibition of CXCL12 production in stromal cells frequently leads to HSC mobilization without affecting the cell numbers in the BM, while absence of SCF causes HSC depletion⁹. The effect of periarteriolar stromal cells also

expressing SCF and CXCL12 is still not fully understood, but the periarteriolar niche has been shown to be an important regulator of HSC quiescence¹². The role of osteolineage cells in maintenance of the HSC pool has been controversially discussed. While they are able to negatively regulate the pool by osteopontin expression, N-cadherin, CXCL12 and SCF originating from these cells have no effect on the HSCs. Furthermore, no spatial association of HSCs and osteolineage cells has been detected⁹. Further components of the stem cell niche such as endothelial cells, macrophages, neurons and megakaryocytes are also able to strongly affect the HSC pool, while the latter was shown to be associated with HSCs and lead to their quiescence by CXCR4 or TGF- β 1 expression (Figure 1)^{1,9,13}.

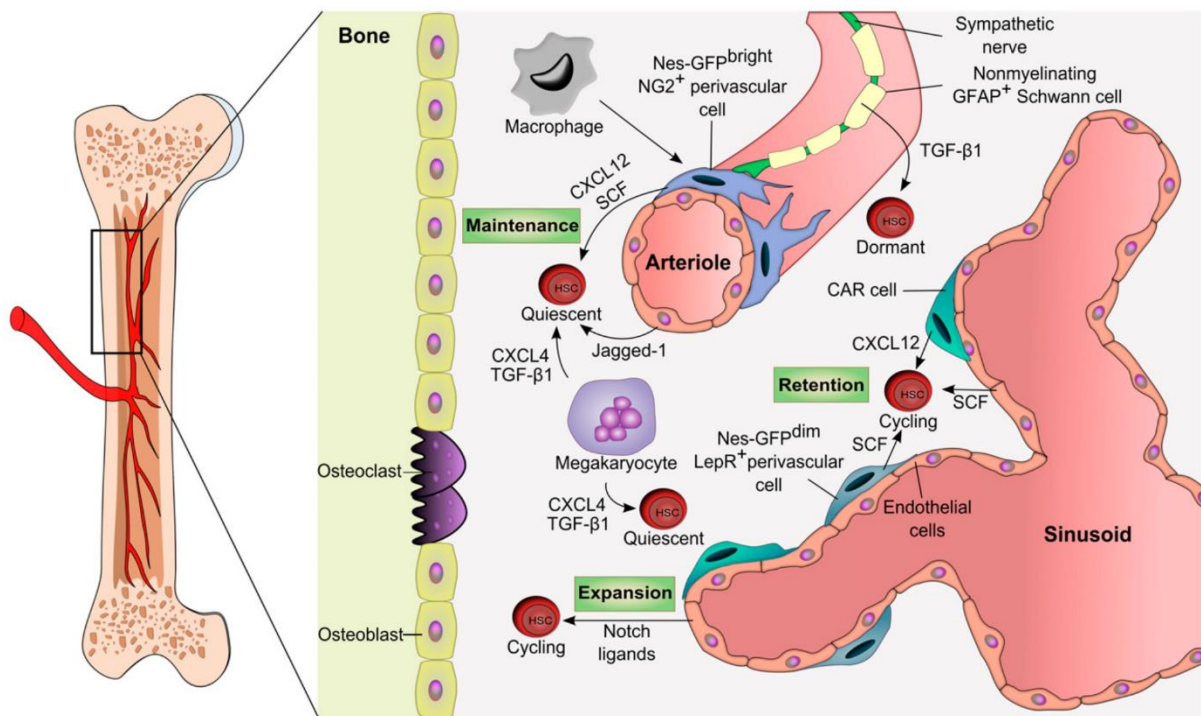


Figure 1. Hematopoietic stem cell (HSC) niche in the adult bone marrow. In the bone marrow HSCs are mainly associated with the vasculature. These perivascular areas, which also contain macrophages, megakaryocytes, neurons, Schwann cells and CAR cells, are termed HSC niches. In the periarteriolar niche, Nes-GFP^{bright} NG2⁺ cells, Schwann cells and endothelial cells induce positively regulate HSC maintenance via CXCL12, SCF and TGF- β 1 expression. The perisinusoidal niche contains less quiescent HSCs. Here, Nes-GFP^{dim} LepR⁺ cells, CAR cells and endothelial cells positively influence HSC self-renewal, proliferation and differentiation. Furthermore, megakaryocytes express CXCR4 and TGF- β 1 leading to HSC quiescence. The osteolineage cells are not spatially associated with HSCs in the bone marrow. CAR cell: Cxcl12-abundant Reticular cell; GFAP: glial fibrillary acidic protein; SCF: stem cell factor; TGF- β 1: transforming growth factor beta-1; Figure modified from Boulais *et al.*¹¹

Blood cells differentiated from HSCs leave the bone marrow by migrating towards the sinusoids to enter the circulation. In general, many of these migratory processes are chemotactic, i.e. driven by chemoattractants. Fully differentiated neutrophils, which constantly enter the circulation, are one of the most abundant cell types in the BM. In case of ongoing inflammatory processes in the organism, the neutrophils are strongly mobilized from the BM to enter the circulation following chemical stimuli such as macrophage inflammatory protein 2 and ELR-containing CXC chemokine KC sensed by CXCR2 receptors^{14,15}. Beside neutrophil migration, also chemically induced HSC mobilization towards the circulation is an important process of medical relevance. For clinical stem cell transplantation, HSC numbers in the blood are increased using different drugs such as granulocyte colony-stimulating factor (G-CSF), acting via reduction of BM SDF1 concentrations, and the cells are subsequently harvested¹⁶. For certain cell types the migration processes have been investigated from the biochemical point of view, but the biophysical aspects of migration are less studied. Especially, the influence of the bone marrow crowdedness and of chemotactic gradient strengths on cell migration is still poorly understood due to limitations in experimental approaches. Here, alternative investigation methods such as *in silico* simulations can provide important insights.

1.2 Megakaryocytes and their development

Megakaryocytes (MKs) are derived from multipotent hematopoietic stem cells and belong to the myeloid cell lineage. MKs mainly reside in the bone marrow, mostly in a close proximity to the vasculature¹⁷, and are here with a size of up to 50 μm in mice and 50-100 μm in humans the largest cells. At the beginning of HSC differentiation to MKs common myeloid progenitor (CMP) cells appear, which later develop into common megakaryocyte-erythrocyte progenitors (MEP). Recent studies even suggest a direct differentiation step from HSC to MEP. These cells further differentiate into the direct MK precursors and subsequently into MKs^{18,19}. Due to uncertainties concerning the early differentiation phases of MKs, a reliable immunostaining and detection of the precursor cells in the bone marrow is still not possible. The whole maturation process is driven by a number of transcription factors, cytokines and chemokines (Figure 2). The most important regulator of megakaryopoiesis is the cytokine thrombopoietin (TPO), which increases platelet production. TPO is constantly expressed and released into the circulation where it is bound by myeloproliferative leukemia virus oncogene (Mpl) receptors on platelets. In case of reduced platelet numbers, TPO concentration increases and leads to enhanced platelet production. The TPO/Mpl axis can activate transcription factors (Friend

leukemia integration 1 transcription factor (FLI1), GATA1/FOG1 complex, GATA2 and others), leading to expression of megakaryocyte specific glycoproteins (GPs) such as GPIb-V-IX complex or GPIIb. At a later timepoint MK/platelet specific tubulin isoform $\beta 1$ is expressed.

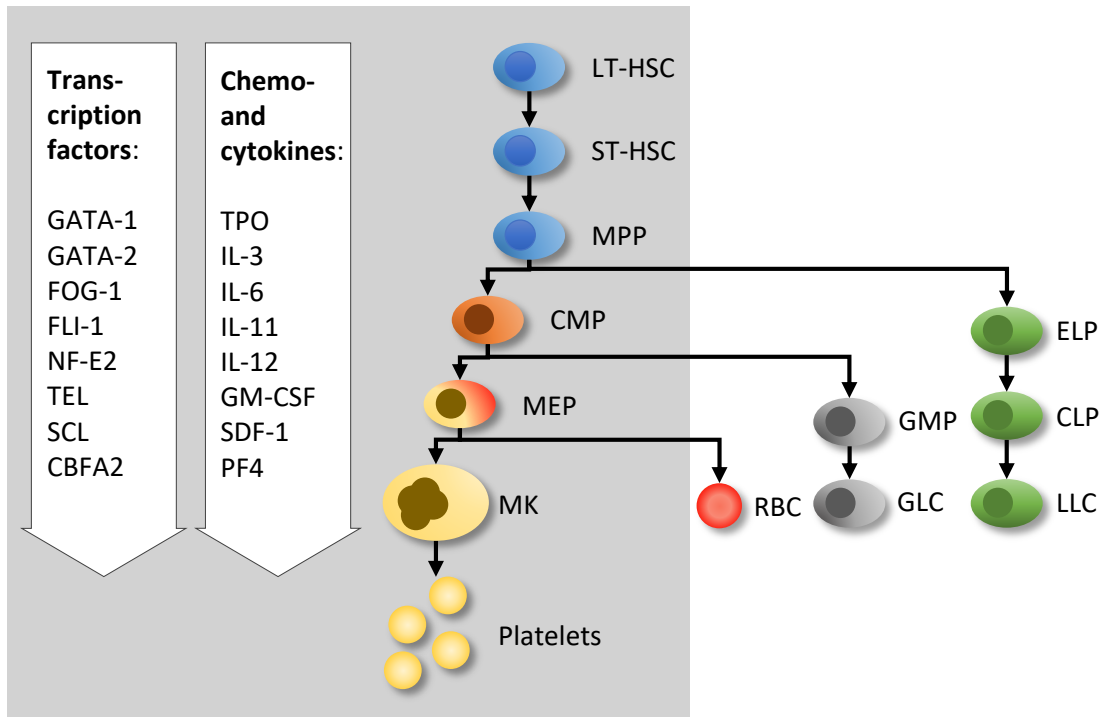


Figure 2. Megakaryocyte maturation pathway. LT-HSCs develop to ST-HSCs, which further differentiate to multipotent progenitors (MPP). MPP give rise to common progenitors (CMPs) and early lymphoid progenitors (ELPs), which subsequently develop to common lymphoid progenitors (CLPs) and finally to lymphoid lineage cells (LLCs). The CMPs further differentiate into megakaryocyte-erythroid progenitors (MEP) and granulocyte/monocyte progenitors (GMP). GMPs give rise to all granulocyte lineage cells (GLCs). MEP develops to either megakaryocytes (MKs) or red blood cells (RBC). Mature MKs release platelets into the blood flow. MK maturation process (grey box) is influenced by different transcription factors, chemokines and cytokines. LT-HSC: long-term HSC; ST-HSC: short-term HSC; FOG-1: friend of GATA protein 1; TPO: Thrombopoietin; FLI1: Friend leukemia integration 1 transcription factor; Figure modified from Yo *et al.* and Pang *et al.*^{18,20}

Nevertheless, mice deficient in TPO or *Mpl* are still able to produce platelets, indicating that different, TPO independent, pathways inducing platelet formation exist. Soluble SDF1 and its receptor CXCR4 expressed by MKs is such a TPO independent regulator of megakaryopoiesis^{18,21}, while it also regulates HSC activity in the bone marrow. During their maturation process, MKs are thought to migrate from the endosteal niche to the vascular niche²². The differences in extracellular matrix protein content and in the concentrations of chemoattractants at the niches are supposed to play a major role in the migration process. In

TPO-deficient mice, SDF1 and fibroblast growth factor 4 (FGF4) induce increased MK motility and transendothelial migration²¹. Furthermore, SDF1 is supposed to guide the MKs towards the BM sinusoids and increase platelet production²³. Nevertheless, short-term intravital imaging of MKs in the bone marrow did not reveal directed migration of the cells towards the vasculature and the concept of the migration was further challenged by volumetric imaging of the bone marrow (Figure 3)^{24,25}.

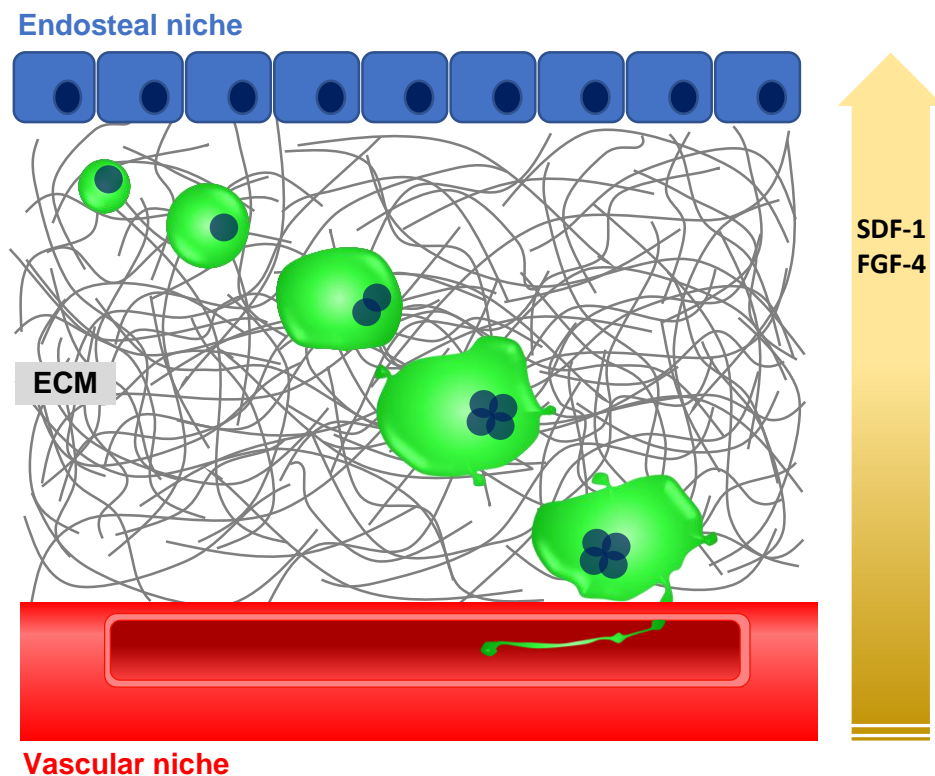


Figure 3. Current model of megakaryocyte migration during its maturation. According to the current model of megakaryocyte maturation, MKs migrate from the bone-associated endosteal niche to the vascular niche during maturation. MKs are guided by concentration gradients of different chemokines, such as SDF-1 and FGF-4, towards the bone marrow vessels. SDF-1: stromal cell-derived factor 1; FGF-4: fibroblast growth factor 4; Figure modified from Bluteau *et al.*²²

Besides the bone marrow, MKs are also found in different other organs such as liver, spleen, kidney, heart and lung and, importantly, the MK number positively correlates with the severity of different diseases²⁶⁻³¹. The MKs are thought to be transported by venous blood flow from the BM to the lungs (or further to other organs), which is the major filtration site for these large cells^{27,32}. Nevertheless, recently Lefrançois *et al.* claimed that MK progenitors are also present in the pulmonary tissue and concluded that the lung is a site of megakaryopoiesis³³.

1.3 Thrombopoiesis

The major role of MKs is the production of blood platelets (about 5000 platelets per MK)³⁴, a process preceded by a complex maturation process during which the MKs gain high ploidy of up to N=256 by endomitosis (DNA replication without anaphase or cytokinesis). The cellular maturation state of a MK is defined by expression of characteristic markers, by production of a demarcation membrane system (DMS) and presence of distinctive platelet organelles such as α -granules and dense granules³⁵. Prior to platelet production the cytoskeleton of a MK undergoes remodeling and cytoskeleton reorganization takes place. Although the process of platelet formation is not fully understood yet due to the high complexity of its underlying cytoskeletal and biochemical mechanisms, the major steps could be identified during the last decades. In general, platelet formation has been investigated in *in vivo* and *ex vivo* experiments, leading to slightly different observations. Mature vessel associated extravascular megakaryocytes form protrusions, also named proplatelets, which are introduced into the sinusoidal lumen of the bone marrow vasculature^{36,37}. While cultured MKs build protrusions in all directions, in the bone marrow mostly only one proplatelet at a time is introduced into the vessel lumen. The proplatelets are filled with bundles of antiparallely arranged microtubules enabling molecular motor induced elongation³⁸. The ends of proplatelets are the sites of final platelet formation, since here the platelet cytoskeleton (including polymerized actin and actin-spectrin skeleton rich membrane) is formed and internal components such as organelles and granules are located. In a final step, dissociation and coiling of one microtubule, most likely due to shear forces in the lumen of the blood vessel^{19,24,39}, lead to separation of the platelet from the proplatelet and to the typical discoid shape³⁸. While this platelet generation mechanism is sufficient for regulation of cell numbers in healthy organisms, it might fail during severe platelet loss. Recent investigations have proposed an alternative mechanism of platelet production by interleukin 1 alpha (IL-1 α) induced MK rupture, which is TPO independent⁴⁰.

Different groups have demonstrated thrombopoiesis in the BM by direct *in vivo* microscopy, leading to the conclusion that bone marrow MKs are the main source of blood platelets^{24,41,42}. But besides the thrombopoiesis in the BM, platelet generation can also take place in the pulmonary tissue^{43,44,33,45}. Nevertheless, clear experimental evidence for significant pulmonary thrombopoiesis in healthy mammals has not been provided yet. The recent publication by Lefrançois *et al.*, stating that pulmonary MKs contribute to 50% of the total platelet numbers, has been positively discussed by different groups, although the study reveals major

experimental weaknesses in terms of evaluation of microscopy data underlying the estimation of thrombopoiesis^{30,46}.

Besides platelet generation, megakaryocytes also have additional functions in the bone marrow. As already mentioned in the previous chapter, MKs are spatially associated with HSCs and regulate their activity by secretion of platelet factor 4 (Pf4 or CXCL4) and transforming growth factor β 1, both leading to HSC quiescence, while in response to stress they enhance HSC activity by expression of FGF1^{13,47}. Due to their size, MKs could potentially affect other processes such as chemokine gradients or cell migration. Nevertheless, this aspect has not been addressed in the literature so far.

1.4 Platelets

1.4.1 Platelet activation and thrombus formation

Platelets are small anucleate blood cells with a discoid shape and a diameter of 3-4 μm in humans and 1-2 μm in mice. They are produced by megakaryocytes in a process termed thrombopoiesis already described above. After being released, platelets have a life span of 7-10 or approximately 5 days in the human or murine circulation, respectively. Despite the considerably short life span, platelets are the second most abundant cells in the circulation (150 x 10³ – 400 x 10³ platelets/ μl in humans and ca. 1000 x 10³ platelets/ μl in mice). Aged platelets cleared by resident macrophages in the spleen or the liver. Since platelets lack a nucleus, *de novo* protein synthesis is strongly limited in these cells.

The platelets contain organelles such as mitochondria, open canalicular and dense tubular systems, peroxisomes and granules (α -granules, dense granule and lysosomes) storing different proteins. More precisely, the highly abundant are equipped with platelet adhesion proteins (e.g. fibrinogen, fibronectin, von Willebrand factor (vWF), P-selectin), coagulation factors, chemokines and glycoproteins, while the smaller and scarcer dense granules contain inorganic molecules (adenosine diphosphate (ADP), adenosine triphosphate (ATP), thromboxane A₂ (TxA₂), calcium ions [Ca²⁺] etc.)⁴⁸.

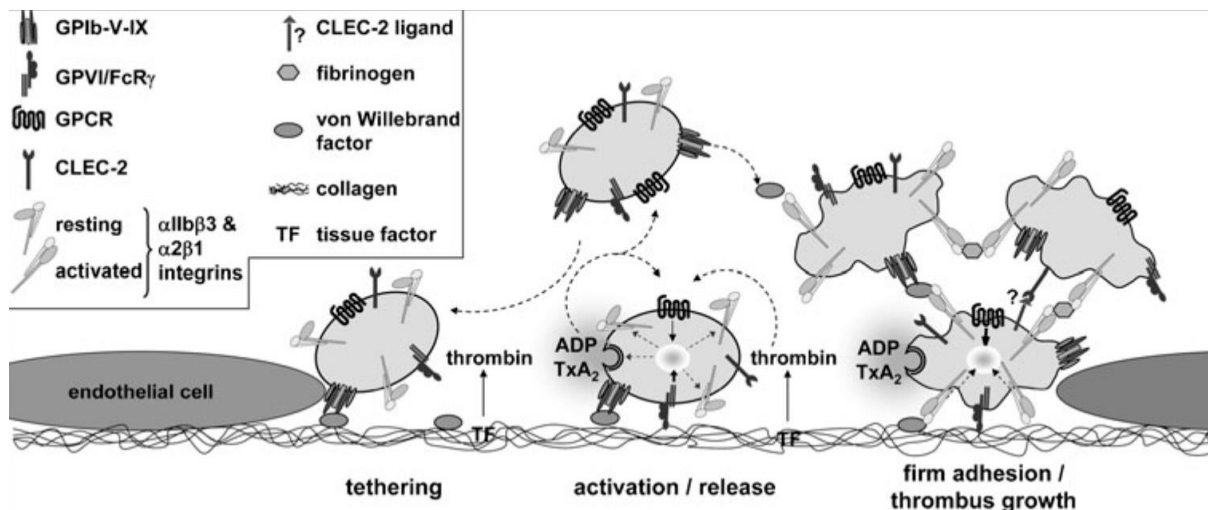


Figure 4. Platelet activation and thrombus formation. Upon vascular lesion, platelets undergo an initial tethering predominantly via binding of GPIb α to the exposed von Willebrand factor. In the next step, platelets become activated mainly due to binding of GPVI to collagen, leading to integrin activation and platelet degranulation. Platelet granules contain different second-wave agonists, which ameliorate the activation process via GPCR signaling. Coincidentally, exposed tissue factor leads to generation of thrombin, which is a strong platelet agonist. Finally, firm adhesion of platelets is achieved by binding of platelet integrins to the extracellular matrix leading to maintenance of GPVI signaling, enhanced degranulation and, in consequence, to activation of further platelets. The stabilization of the growing thrombus is mediated via CLEC-2, the ligand of which is still not identified. Figure from Stegner *et al.*⁴⁸

The primary function of platelets is activation and thrombus formation during hemostasis in upon vascular lesion and, thus, they are essential for preventing extensive blood loss. Thrombus formation process can be subdivided in three major steps: platelet tethering, activation and firm adhesion leading to thrombus growth^{48–50}. Upon vascular damage, subendothelial extracellular matrix proteins such as fibrillar collagen and laminin get exposed. Under intermediate or high shear conditions (1000 – 10000 1/s) platelet glycoprotein GPIb α , which is a part of the receptor complex GPIb-V-IX, weakly binds to collagen-associated vWF leading to a rapid deceleration and rolling of platelets along the vessel wall^{51–54}. This initial tethering is not a firm adhesion, but rather serves for enabling the second step of the process where platelet GPVI receptor binds to its major ligand collagen^{55,56}. GPVI-collagen interaction induces an immunoreceptor tyrosine-based activation motif (ITAM) signaling cascade resulting in increased intracellular [Ca²⁺] concentrations. It is important to note that besides GPVI signaling pathway, C-type lectin-like receptor 2 (CLEC-2) mediated platelet activation via hem-ITAM signaling is also highly relevant for thrombosis and hemostasis. Nevertheless, the natural ligand of platelet CLEC2 during thrombosis and hemostasis has not been identified yet⁵⁷. Upon activation, platelet membrane becomes negatively charged by surface exposure of

procoagulant phosphatidylserine (PS) and the cytoskeleton undergoes rearrangements. Subsequent α - and dense granule mobilization culminates in release of their content, including the so called second wave mediators such as ADP and TxA₂. Released second wave mediators ADP, TxA₂ and the generated thrombin act as platelet activators by binding to G protein-coupled receptors (GPCRs) (G_q, G_{12/13} and G_i) and induce additional recruitment of further platelets to the growing thrombus^{56,58}.

During firm adhesion integrins undergo a conformation change from low to high affinity state due to the inside-out-signaling enabling interaction with their ligands (outside-in-signaling)^{59,60}. The most abundant platelet integrin GPIIb/IIIa on one side induces platelet-platelet bridging by binding to fibrinogen and this leads to thrombus growth. On the other side it binds to extracellular matrix (ECM) components (collagen-bound vWF, fibronectin, vitronectin) resulting in firm platelet adhesion. Further activated integrin-ECM (α 2 β 1-collagen, α 5 β 1-fibronectin, α 6 β 1-laminin and α v β 3-vitronectin) interactions enhance the platelet adhesion to the site of injury⁵⁴. Hence, platelet activation leads to pronounced cytoskeleton rearrangement manifesting itself in changed flat cell shape and formation of filopodia and lamellipodia.

Besides primary hemostasis leading to platelet aggregate formation, the secondary hemostasis (coagulation cascade) culminating in fibrin clot formation takes place. The extrinsic pathway of the secondary hemostasis is initiated by the interaction of plasma factor VII with the tissue factor. The intrinsic pathway (contact activation pathway) is induced by activation of factor XII (FXII) upon its contact with negatively charged molecules. Both the extrinsic and the intrinsic pathways of the coagulation cascade lead to thrombin formation and subsequent cleavage of fibrinogen to fibrin⁴⁸.

Platelets are essential for maintaining vascular integrity upon vessel injuries. Nevertheless, they are also involved in different other processes, e.g. under pathological conditions, such as rupture of an atherosclerotic plaque, platelets may induce uncontrolled occlusive thrombus formation. The occlusive thrombus obstructs the blood flow in the vessel or may be transported to another organ. Embolization of such thrombi results in severe diseases like myocardial infarction, ischemic stroke or pulmonary embolism, which are one of the major causes of death and morbidity worldwide^{61,62}. It is important to note, that although hemostasis and thrombosis do share signaling pathways and are closely related, they are two mechanistically separated processes. Different studies could demonstrate that absence of surface proteins involved in occlusive thrombus formation (such as FXII, plasma fibronectin, GPVI or CLEC-2) lead to no or only mild reduction in hemostatic functionality (assessed as tail bleeding times) in mice⁶²⁻⁶⁴.

Prevention of thrombus formation without the risk of bleeding complications is the major aim of pharmaceutical research targeting thromboembolic diseases.

1.4.2 The role of platelets in inflammatory processes

Besides thrombosis and hemostasis, platelets play an important role in different other (patho) physiological processes such as embryonal angiogenesis^{65,66}, cancer metastasis^{67,68} and inflammation. During inflammatory processes platelets play multiple roles, including the recruitment of immune cells and the maintenance of vascular integrity after their extravasation.

During inflammation, immune cells are recruited to the affected site and they extravasate which causes vascular damage. Platelets prevent inflammatory bleeding in different mouse models including immune complex-induced and irritant contact dermatitis, lung inflammation, viral infection, solid tumors and ischemic stroke. Nevertheless, the underlying mechanisms are strongly organ and inflammation type dependent. It is remarkable that platelet activation by GPVI via ITAM signaling but not degranulation and aggregate formation are involved in prevention of bleeding in skin and lung inflammation models. On the other side, for avoiding hemorrhages during the inflammatory processes resulting from ischemic stroke or viral infection the platelet integrin GPIIb/IIIa is indispensable (reviewed in ^{69,70}).

Platelets contain a big number of proteins associated with the immune response which are secreted upon platelet activation and degranulation. Secreted inflammatory modulators (histamine, serotonin (5-HT)) or lipids (TxA₂), chemokines (CXCL4, CXCL7, CXCL1, CXCL12 etc.) and cytokines (IL-1 β , IL-1 α) can recruit and activate immune cells such as neutrophils, macrophages or B and T cells^{68,71}. In addition, P-selectin expressed on platelet membrane, upon activation, can bind to the P-selectin glycoprotein ligand 1 (PSGL1) of immune cells (neutrophils, T cells) and potentially facilitate their recruitment to the site of inflammation and the subsequent extravasation⁷²⁻⁷⁴. Decreased platelet numbers or GPIb blockade are associated with reduction of neutrophil infiltration into the brain in an inflammation model⁷⁵. On the other hand, the GPIb-V-IX complex seems to have an anti-inflammatory effect during sepsis in mice. Interestingly, the anti-inflammatory pathway is independent of vWF, but seems to act via binding to macrophage-1 antigen (Mac1) of neutrophils⁷⁶. In humans, platelets are not only able to recruit immune cells, but also sense pathogens present in the circulation via toll-like receptors (TLRs) 1, 2, 4-7 and 9⁷⁷.

1.5 Ischemic stroke and reperfusion injury

1.5.1 Brain anatomy and cerebral blood flow

The brain is, together with the spinal cord, a part of the central nervous system (CNS) and is located under the skull. The organ is covered by three meninges: dura mater, arachnoid mater and pia mater. The area between the arachnoid and pia mater is also called subarachnoid space and contains the cerebrospinal fluid (CSF) which is produced in the ventricular system of the brain.

The brain can be divided in three main parts: the cerebrum (anterior), the cerebellum (posterior) and the brainstem (inferior). The cerebrum consists of the left and the right hemispheres which are the largest compartments of the brain. The outer region of the cerebrum is termed cortex and mainly contains neuron bodies while the white matter beneath is made up of neuronal axons⁷⁸.

The brain is the organ with the highest energy consumption, thus it requires extensive nutrient and oxygen supply. In consequence, the organ is strongly vascularized. The arterial blood supply is provided by two common carotid arteries, which divide into internal carotid (anteriorly) and vertebral (posteriorly) arteries. The circle of Willis connects the left and right anterior and posterior arteries. From the circle of Willis three big arteries on each side emerge: the anterior cerebral artery, middle cerebral artery and the posterior cerebral artery. The middle cerebral artery (MCA) provides blood supply mainly for the cerebrum and most of ischemic stroke cases are caused by the occlusion of this vessel. Partially, the brain arteries and veins cover the surface of the organ and are termed pial. The vessels of the pial arteriolar and venous networks enter the cortex perpendicularly to the surface and further branch into smaller capillaries⁷⁹.

The endothelium of the brain vasculature has unique features compared to vessels in other organs. The endothelial cells of the CNS have continuous tight junctions limiting cell extravasation and exchange of molecules. The latter is closely regulated by specific transporters. In this manner, the brain tissue is separated from the peripheral blood flow resulting in increased protection from neuron damage. This multicellular vascular structure is also referred to as the blood brain barrier (BBB)⁸⁰.

1.5.2 Early phase of ischemic stroke and reperfusion injury in the brain

Stroke is a leading cause of death and permanent disability worldwide, especially in the aging population. Stroke can occur as a result of intracerebral hemorrhage or of cerebral ischemia, while the latter accounts for more than two thirds of all cases. As advanced age is a significant risk factor for stroke development, it is expected that number of patients will increase in the next years due to increase of mean age of the population⁸¹. In general, during cerebral ischemia one major and/or many smaller vessels are occluded due to a cardiogenic or atherosclerotic thromboembolism. The vessel occlusion leads to undersupply of the affected brain region with oxygen and nutrients leading to tissue death. At early stage of ischemic stroke only a small area of the brain, the ischemic core, is irreversibly damaged. A larger volume surrounding the ischemic core, also termed penumbra, shows reduced blood flow. Rescuing the ischemic penumbra from irreparable damage is the major aim of clinical treatment of patients with acute ischemic stroke⁸².

For many decades, the only treatment available for ischemic stroke has been its prevention by application of anticoagulants, but no curative steps could be taken. The main goal after occurrence of an ischemic stroke is recanalization – the removal of the occlusive thrombus from the affected major vessel⁸⁴. Since 1995 thrombolysis via intravenous injection of recombinant tissue-type plasminogen activator (rt-PA) has been available as a curative treatment. Nevertheless, thrombolysis is only beneficial if applied during the first 4.5 h after ischemic stroke and is, in many cases, not successful in terms of reperfusion injury. A novel method termed thrombectomy using stent retriever systems to mechanically remove the occlusive thrombus in the early phase (4.5-6 h) after stroke has been found to be superior to thrombolysis⁸⁵. In many cases, successful recanalization leads to the return of the blood flow into the downstream capillaries, a process termed reperfusion⁸⁴. But, often reperfusion does not take place (no-reflow phenomenon) or induces a severe ischemia reperfusion (I/R) injury^{84,86,87}. Despite these important developments in the treatment of ischemic stroke, powerful pharmacological agents usable even during an extended treatment window and preventing the reperfusion injury without an increased risk of bleeding complications are still lacking. For development of such drugs, a deeper understanding of the pathomechanisms underlying reperfusion injury is essential. Different groups could demonstrate that the immune system, platelets and the neuronal unit are involved in these processes in a highly complex manner^{81,88}. Nevertheless, the interaction of the various components of the process is still poorly understood.

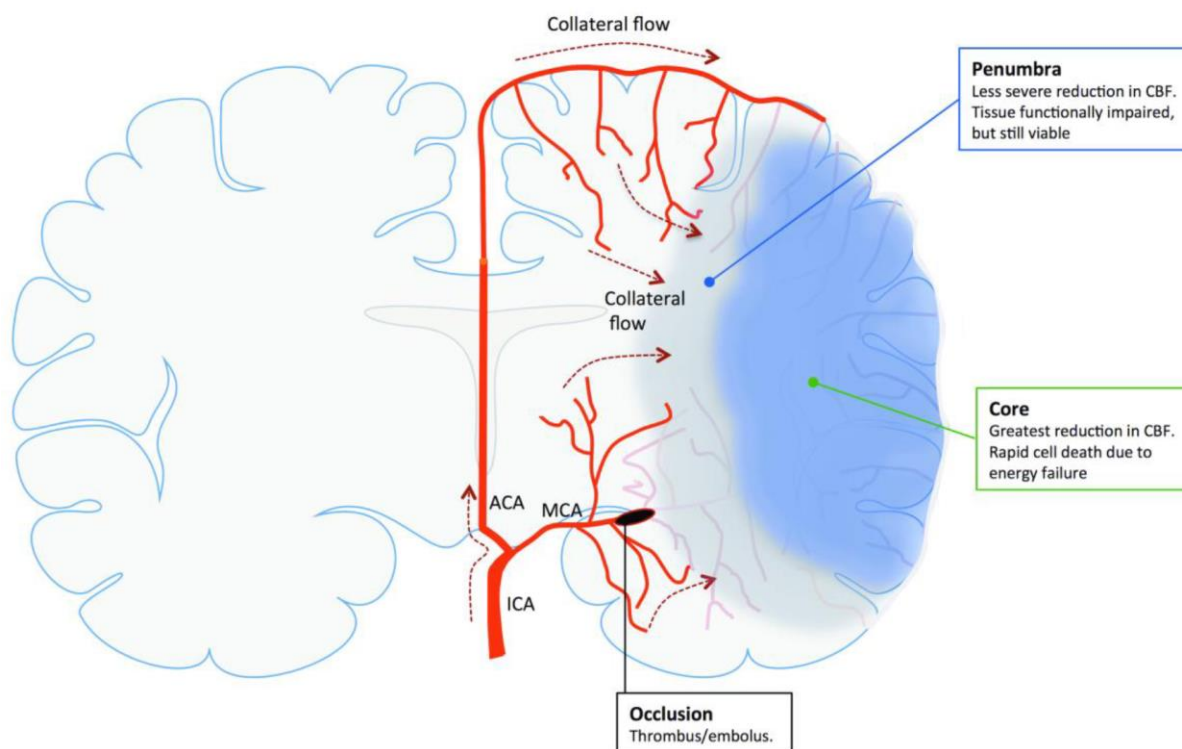


Figure 5. Development of ischemia reperfusion injury after ischemic stroke. After formation or embolization of a thrombus in a brain artery, certain brain regions, termed “the core”, cannot be supplied with oxygen and nutrients due to inhibited blood flow. Most frequently, the middle cerebral artery is the origin of the ischemic stroke. The core region is in most cases irreversibly damaged after a very short period of time. The surrounding region of the core (penumbra) has decreased nutrient and oxygen supply due to collateral blood flow. The penumbral tissue is functionally impaired and can be prevented from death by rapid thrombus lysis. Nevertheless, even in cases of fast medical treatment, patients develop progredient infarction where the penumbra undergoes tissue death despite successful recanalization. ACA: anterior cerebral artery; MCA: middle cerebral artery; ICA: internal cerebral artery. Figure from Jackman and Iadecola⁸³.

Experimental animal models of ischemic stroke have strongly increased the knowledge on the underlying mechanisms of reperfusion injury. In most cases, the studies are performed with small rodents, such as rats and mice⁸⁹. Especially, targeting specific proteins due to availability of different genetically modified mice has strongly contributed to the stroke research in the last two decades⁸⁹. Cerebral ischemia can be experimentally induced by 1) intraluminal mechanical occlusion of the middle cerebral artery using a thread or filament (which is the most frequently used technique in the literature), 2) application of a vasoconstrictor or 3) photochemically triggered thrombus formation in the cerebral vasculature^{89–91}. The duration of the occlusion is mostly kept between 30-90 min or over 3 h for transient and permanent ischemic stroke modelling, respectively⁸⁹. For studying the reperfusion injury only transient

models can be used, where the transient middle cerebral occlusion (tMCAO) is the most prominent model.

The established models of the thrombo-inflammatory processes of the reperfusion injury can, to a significant extent, be translated into or confirmed by clinical studies. In respect of the thrombo-inflammatory processes, the cerebral I/R injury after ischemic stroke can be subdivided in three phases: the acute phase (minutes to hours), the subacute phase (hours to days) and the chronic phase (days). In the following chapters, the pathomechanisms involved in the acute phase of I/R injury are discussed.

1.5.3 The role of platelets in the thrombo-inflammatory model of the acute phase of the reperfusion injury

The role of platelets in the prevention and treatment of ischemic stroke is widely investigated and discussed. While the inhibition of platelet aggregation has been proven to be beneficial for avoiding primary or secondary ischemic stroke⁹², their role during the reperfusion injury is still not fully understood. Lack or inhibition of platelet GPIIb/IIIa and GPVI were demonstrated to be beneficial for the outcome in an experimental ischemic stroke model, while GPIIb/IIIa was found to prevent intracerebral bleeding⁹³. Later, reduction of platelet counts down to 10% of initial values was shown to improve neurological outcome and reduce infarct volumes in mice⁹⁴. Nevertheless, the exact mechanisms of their action can only be provided by experimental studies on genetically modified or pharmaceutically treated mice.

Platelet tethering via GPIIb-vWF binding is an important mediator of I/R injury after stroke. The inhibition of the vWF binding site on GPIIb by p0p/B Fab injection reduces tissue death and leads to better neurological outcome after induction of ischemic stroke when applied before or shortly after the tMCAO model in mice⁹³. Despite the reduced hemostatic function of platelets after GPIIb blockade, which results in prolonged tail bleeding times, no intracerebral bleeding complications were registered after tMCAO⁹³. Moreover, p0p/B Fab treatment reduces leukocyte infiltration into the ischemic brain, indicating that platelets are actively involved in the inflammatory processes during I/R injury⁹⁵. The major binding partner of GPIIb – the vWF – is also actively involved in development of I/R injury after stroke. Recent studies showed that plasma and platelet derived vWF plays different roles in hemostasis, thrombus formation and cerebral thrombo-inflammation⁹⁶. While only plasma vWF is indispensable for hemostasis and thrombosis, both types of vWF mediate post-ischemic reperfusion injury in a GPIIb but not in GPIIb/IIIa dependent manner. Similar to p0p/B Fab treated animals, despite the significantly

increased tail bleeding times, the lack of vWF does not lead to intracranial hemorrhages after ischemic stroke^{97–99}. In summary, the inhibition of the initial platelet tethering can provide a new and safe preventive or curative treatment for stroke patients.

Glycoprotein VI (GPVI) which initiates platelet activation by collagen binding also plays an important role during thrombo-inflammatory processes of the I/R injury. Mice lacking GPVI show improved outcome in the tMCAO model compared to wild type animals. Nevertheless, the protective effect is here milder than that achieved by inhibition of the GPIIb-vWF interaction, possibly due to platelet activation via GPCR signaling^{100,93}. Absence or pharmaceutical inhibition of the signaling molecules downstream of GPVI is also beneficial in the tMCAO model as recently demonstrated¹⁰¹, while GPVI hyper-reactivity aggravates stroke outcome¹⁰². Secretion of α - and dense granules upon platelet activation allows release of different proteins and inorganic chemicals many of which lead to further recruitment and activation of platelets or act on the vasculature and the immune cells. In mice lacking α -granules (*Nbeaf1*^{-/-}) or mice, which are unable of dense granule secretion (*Unc13d*^{-/-}) were protected in an experimental stroke model^{103,104}. Further, lack of platelet IL-1 α was shown to be beneficial in ischemic stroke¹⁰⁵. In summary, GPVI and its downstream ITAM signaling cascade as well as platelet degranulation are potential candidates for pharmaceutical treatment of thrombotic diseases although the effect in experimental ischemic stroke is milder compared to blockade of platelet tethering^{93,100}.

The last step of thrombus formation which is mediated by platelet integrin activation was thought to play a major role in the development of irreversible tissue damage after stroke^{106,107}. However, recent studies challenge this hypothesis. Mice treated with anti-GPIIb/IIIa antibody JON/A-Fab₂ fully inhibited platelet aggregate formation without altering the platelet counts¹⁰⁸. In the experimental stroke model, the majority of these animals died of intracerebral hemorrhages. Surprisingly, the few survivors did not show improved outcome after tMCAO⁹³. In contrast to GPIIb/IIIa blockade, genetic deficiency of GPIIb results in reduced cerebral infarct size¹⁰⁹. The mechanistic differences between pharmaceutical inhibition and genetic deficiency of the GPIIb/IIIa during ischemic stroke are currently not clear and, thus, the role of platelet aggregation in the development of I/R injury cannot be precisely defined. Nevertheless, clinical studies confirm the severe increase of intracerebral hemorrhage upon GPIIb/IIIa blockade in stroke patients^{110,111}.

Factor XII – the initiator of the contact activation pathway –strongly affects the outcome of I/R injury after stroke. Mice deficient in FXII or treated with FXII inhibitor rHA-Infestin4 are

protected in the tMCAO model without inducing bleeding complications¹¹². FXII is not only involved in the coagulation cascade, but also in inflammatory processes. FXII induces the generation of kallikrein and thus is a major regulator of the kinin-kallikrein system, which is strongly involved in inflammation. It is not fully clear which of the multiple functions of factor XII is crucial for the progression of infarction^{113,114}. However, FXII could be one of many links between the signaling pathways of platelets and immune cells during cerebral I/R injury.

1.5.4 The role of immune cells and the endothelial cells in the acute phase of the reperfusion injury

Upon cerebral ischemia, neurons in the hypoxic region release danger associated molecular patterns (DAMPs) which activate the resident microglia within minutes. Microglia, which are specialized macrophages resident in the brain, are the first immune cells to become activated during the early phase of acute stroke. As a consequence, sterile inflammation develops in the core and the penumbra upon I/R injury¹¹⁵. Interestingly, macrophages from the peripheral blood flow infiltrate the ischemic brain only days after the initial reperfusion injury¹¹⁶. Microglia activation is followed by release of cytokines (IL-1, tumor necrosis factor (TNF), IL-6) and proinflammatory chemokines (CCL2, CCL3, CCL5) resulting in BBB damage and recruitment of immune cells from the peripheral blood^{90,117}. Despite the role of microglia as the initiators of the reperfusion injury, their absence leads to a deteriorated outcome¹¹⁸.

Proinflammatory cytokines induce increased expression of adhesion molecules on the surface of endothelial cells (ECs) resulting in enhanced leucocyte rolling and their subsequent transmigration¹¹⁷. Levels of P-selectin expression, which mediates the initial low-affinity binding and rolling of leukocytes at the vessel walls, is increased upon ischemic stroke and mice genetically deficient of P-selectin seem to be protected in tMCAO⁸¹. Nevertheless, it is unclear whether the missing leukocyte-EC or leukocyte-platelet interactions provide the protective effect during I/R injury. Members of the immunoglobulin superfamily such as the intercellular adhesion molecule 1 (ICAM1), the vascular cell adhesion molecule 1 (VCAM1), the carcinoembryonic antigen-related cell adhesion molecule 1 (CEACAM1) and the platelet-endothelial cell adhesion molecule 1 (PECAM1), which are responsible for leukocyte-EC binding, play a major role during stroke^{81,119}. PECAM1 is expressed on both endothelial cells and platelets and mainly mediates adhesion of leukocytes to the endothelium and their extravasation. Nevertheless, during EC apoptosis it is shed from the cell surface via metalloproteinase-dependent cleavage and, in the soluble state, is thought to act in an anti-

inflammatory manner also during the ischemic stroke^{120–122}. Indeed, patient suffering from ischemic stroke show elevated levels of sPECAM1¹²³. The role of a further EC marker – CD105 (endoglin) – is still not understood for tMCAO, but during permanent ischemic stroke it acts protective. Here, *Eng*^{+/-} mice (where *Eng* is the gene encoding CD105) were more susceptible to permanent model of experimental stroke compared to wild type animals¹²⁴. It is important to note that even when tight junction functionality of the endothelium is impaired 6 h after tMCAO by the presence of leukocytes and proinflammatory cytokines, the severe structural damage occurs only 2 d after reperfusion¹²⁵.

Neutrophils, T cells and dendritic cells (DCs) of the peripheral blood have been detected in the ischemic brain during the first 24 h after stroke¹²⁶. However, DC infiltration occurs only later (approximately after 1d) during the acute or subacute phase and depletion of these cells has no impact on the outcome of tMCAO^{117,127}. Mast cells accumulate in the brain during the acute phase and induce brain swelling and neutrophil recruitment to the ischemic regions already 4 h after I/R^{90,117}.

The adaptive immune system is strongly involved in the progression of I/R injury after stroke. *Rag1*^{-/-} mice, which are deficient of T and B cells, are protected in transient ischemic stroke^{128,129}. Previous studies could demonstrate that B cells are not involved in the pathomechanism of acute stroke¹³⁰, but T cells enhance the thrombo-inflammatory process. CD4⁺ and CD8⁺, but also regulatory T cells (Treg), were shown to play a harmful role in ischemic stroke^{131,132}. Nevertheless, the role of regulatory T cells is still under discussion as in other studies a protective effect of Treg transfusion has been detected^{133,134,135}. Further, IL-17, which is mainly produced by $\gamma\delta$ T cells, also negatively affects the outcome of stroke¹³⁴. Interestingly, antigen recognition or T cell receptor co-stimulation do not play a role in T cell mediated I/R injury¹³¹.

The infiltration of neutrophils into injured areas after cerebral I/R has been demonstrated in both experimental and clinical studies^{117,126}. However, the exact role of neutrophils in the acute phase of ischemic stroke is still under controversial discussion^{81,117}. Most experimental studies show an accumulation of neutrophils at the site of infarction during the first hours after I/R and genetic deficiency or antibody blockade of neutrophil adhesion proteins lead to tissue protection¹¹⁶. Nevertheless, the protective effects are more pronounced in transient compared to the permanent MCAO models^{90,134,136}. During the acute phase of tMCAO neutrophils accumulate within the brain vasculature and the actual extravasation is observed only at later time points, but it is still not clear, whether it always takes place^{133,90}. However, in experimental

models of permanent ischemic stroke neutrophil extravasation occurred earlier compared to the transient MCAO, but the mechanistic impact of this process is fully unclear^{137,138}. Importantly, neutrophil localization does not correlate with increased BBB permeability, neutrophil extracellular trap (NET) formation or platelet aggregation¹³⁹. Neutrophil-platelet interaction is a further factor in ischemic stroke. During stroke, elevation of platelet-bound neutrophil numbers in the peripheral blood flow is positively correlates with a poor outcome in stroke patients. During inflammatory processes, neutrophils can bind to platelets via P-selectin-PSGL1 interaction, but it is unclear whether this interaction also affects the progression of the I/R injury⁷³.

1.6 Advanced fluorescence imaging techniques

Microscopy is one of the most powerful tools for investigation of physiological processes, giving information about spatial distribution of different subjects of interest. Especially fluorescence microscopy has become a major tool for biological research as it not only gives spatial information, but also allows for detection of specifically stained proteins, thus combining structural and mechanistic studies.

1.6.1 Two-photon intravital microscopy

Fluorescence microscopy of cell monolayers or thin tissue sections is often used for the investigation of physiological questions. Nevertheless, for a number of processes intravital microscopy of model organisms such as mice or rats is essential. During intravital microscopy the light must penetrate the tissue to visualize the organs of interest such as brain, bone marrow, tumor and others. But light absorption and scattering by biological samples limit the imaging depth down to 80-100 μm , which in many cases is not sufficient for microscopic investigation.

Light absorption and scattering by the tissue is strongly dependent on the light wavelength, more precisely, tissue is more transparent for photons with lower energy. I.e. in terms of higher light penetration depth near-infrared or infrared fluorophores are advantageous compared to dyes of visible wavelength. Nevertheless, this ideal approach is limited by inability of synthesis of stable infrared fluorophores which would reliably stain targeted proteins.

Almost three decades ago, a new scanning microscopy technique using two-photon excitation was developed, which partially circumvented the limitations mentioned above¹⁴⁰. The underlying theory was already presented by Maria Göppert-Mayer 1931¹⁴¹, but the experimental realization was first described after development of complex laser systems¹⁴⁰. Two-photon excitation uses a non-linear quantum mechanical process, where two photons, which nearly simultaneously reach a fluorophore, are able to excite it together, while their energies add (in a good approximation). Thus, excitation of fluorophores in the visible spectrum become possible with near-infrared photons. The process of two-photon excitation takes place with very low probability. Thus, a high density of photons is required to realize durable excitation of the sample, which can be achieved with pulsed lasers. In this case, the photon density is sufficiently high only in a very small imaging volume making the two-photon microscopy intrinsically confocal. Due to the low energy of the used photons the technique also shows relatively low phototoxicity and photobleaching effects¹⁴².

During two-photon microscopy (2PM) also the detection wavelength has to be taken into consideration. While a long wavelength excitation light can penetrate the tissue, the emitted light still has high energy despite the Stokes shift and, thus, limits the imaging depth. As a consequence, red fluorophores are beneficial to achieve an imaging depth of up to 1 mm. Nevertheless, exciting such dyes requires the usage of pulsed lasers at >1100 nm wavelengths, which can be achieved by an optical parametric oscillator (OPO) able to tune the wavelength to up to 1300 nm^{143,144}.

Since its invention, 2PM has been used for the investigation of various biomedical questions. For investigation of megakaryocytes in murine bone marrow Junt and colleagues were the first to establish the 2PM of these cells and to demonstrate proplatelet formation and low motility of the cells *in vivo*²⁴. Intravital imaging of brain tissue requires removal of the skull, as bones strongly absorb the excitation light. Here, the methods of skull thinning and open cranial window (OCW) have been established for small rodents to enable deep brain imaging, which are reviewed elsewhere¹⁴². Skull thinning, where only a very thin layer of the skull remains in the region of interest, enables imaging only for 1-2 days after the surgery due bone regrowth¹⁴⁵. For OCW, the skull is replaced by a small cover slip, which can remain for up to several months without altering the health condition of the animal^{142,146}. Since in the first days after surgery brain swelling and local inflammatory response take place, investigation of processes including immune response are, in general, performed by using OCW.

Although 2PM enables intravital tissue imaging, it has several limitations. Namely, the imaging speed and the field of view are in the range of typical scanning laser microscopes and the imaging depth in many tissue types cannot exceed 700-1000 μm . At the moment, there is no fluorescence microscopy technique circumventing these limitations. For imaging of whole organs, 2PM has to be combined with optical clearing methods or to be replaced by other microscopy techniques such as light sheet microscopy, which will be discussed in the following chapters.

1.6.2 Optical clearing methods

Many biomedical questions require the fluorescence imaging of whole organs to enable elucidation of the processes in different regions. Since most organisms are not transparent for visible light, mostly thin organ sections are imaged by widefield or laser scanning microscopy. These methods do provide information about different organ regions, but at the same time they are strongly limited due to their small imaging volume and unavoidable cutting artifacts.

To improve light penetration in tissue, it is important to understand the underlying mechanisms of its non-transparency: light absorption and light scattering. Light absorption always occurs in the tissue, but some molecules (e.g. hemoglobin-rich organs such as blood vessels) are better absorbers compared to others. In general, it is almost impossible to prevent light absorption in tissues, but normally increasing the power of the excitation light is sufficient for successful fluorescence imaging. Light scattering is a more challenging limitation for microscopy. The refractive index of different parts of a cell can strongly vary. At the interface of two such regions the propagating light is scattered, i.e. the light is redirected in all directions. Since thick tissue contains a very high number of such interfaces, the excitation light is not capable of reaching deeper tissue regions^{147,148}.

Optical clearing aims at homogenizing the refractive index of the entire tissue and can be achieved by different strategies. The modern clearing techniques can be separated in solvent-based and aqueous-based clearing methods. In solvent-based techniques (such as BABB¹⁴⁹, 3DISCO¹⁵⁰, iDISCO and others¹⁵¹) the tissue is first dehydrated and lipid components are also partially flushed out of the organ. In a second step, the lipids in the proteinaceous tissue are solvated and homogeneously distributed in the tissue by using a second clearing reagent, leading to homogenization of the refractive indices and tissue transparency. The solvent-based

techniques are very robust and achieve high clearing effects in almost all tissue types^{147,148}. Still, in many cases, their use is limited due to quenching of fluorescent proteins.

The aqueous-based techniques preserve the water content of the tissue and use watery solutions of high refractive index to homogenize the optical features of the sample. Here, different sub-groups of these techniques use either 1) passive immersion in a medium with matched refractive index^{152,153} or 2) lipid removal and subsequent hydration of the tissue^{154,155,155,156} or 3) lipid removal and subsequent immersion in refractive index matched medium^{147,157,158}. Although these methods preserve organic fluorescent proteins, the clearing capabilities are in most cases poorer compared to solvent-based techniques¹⁴⁸.

Optically cleared tissue can be imaged by different microscopy techniques, while two-photon microscopy and light sheet microscopy are the most frequently used methods.

1.6.3 Light sheet fluorescence microscopy

Whole organ microscopy of cleared organs is in many cases possible using 2PM, minimizing light absorption and enabling high resolution. Nevertheless, for big samples such as brains the long acquisition time and the resulting high photobleaching can be limiting factors. Although long acquisition times can be reduced using wide-field epifluorescence microscopes (accepting the lower resolution), photobleaching cannot be prevented due to propagation of the excitation light through the entire sample, repeatedly exciting the fluorophores during volumetric imaging and thus leading to fluorophore degradation.

To avoid strong photobleaching during volumetric imaging, the area of excitation has to be minimized for every imaged plane, a feature exclusively provided by light sheet fluorescence microscopy (LSFM)¹⁶⁰. The basic concept of the method is a perpendicular positioning of the excitation and detection paths relative to each other, which was introduced at the beginning of the 20th century by Siedentopf and Zsigmondy¹⁶⁰. The initial implementation of the technique for laser light was presented by Voie *et al.*¹⁶¹, while the paper by Huisken *et al.*¹⁶² was the starting point for increased popularity of the technique^{160,162}. Development of LSFM and the tissue clearing methods synergistically led to a fast advancement of volumetric imaging in the last decade, enabling, for the first time, to image whole organs¹⁶³ and even living organisms¹⁶⁴.

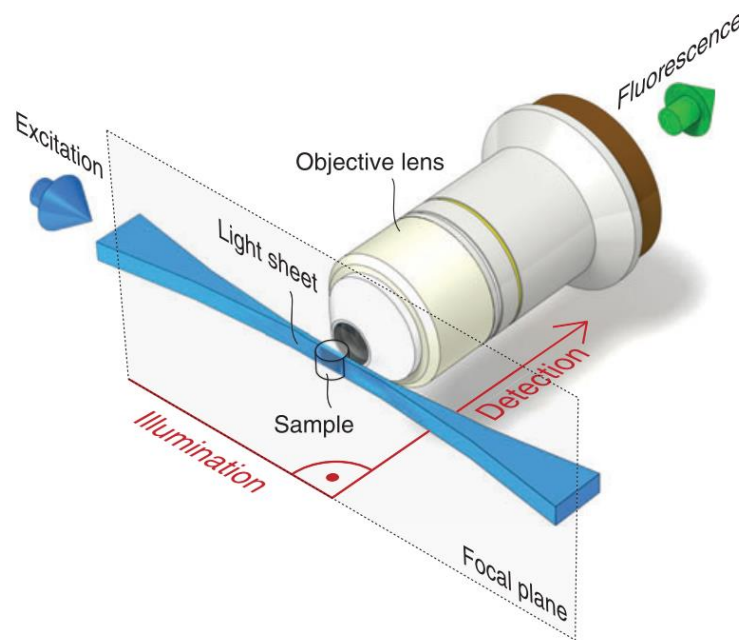


Figure 6. Principle of light sheet fluorescence microscopy. Transparent fluorescent sample is excited by a thin laser light sheet, which is generated either by scanning a laser beam or by using a cylindric lens. The excitation light sheet is focused and illuminates one thin plane of the sample. The detection objective is positioned perpendicular to the excitation light path so that its focal plane colocalizes with the light sheet. Figure from Huisken *et al.*¹⁵⁹

The primary source of excitation light is a Gaussian laser beam, which is transformed into a thin sheet using a cylindric lens or by ultrafast scanning^{159,165}. Focused by an excitation objective, a light sheet of 5-30 μm thickness is guided to the transparent sample. The sample is normally located in a special chamber filled with an immersion medium. 3D scanning is mostly performed by moving the sample perpendicular to the light sheet plane. The emitted fluorescence is detected by another objective perpendicular to the excitation axis and further guided to detectors (Figure 6)¹⁵⁹.

Besides the reduced photobleaching, usage of light sheet excitation is beneficial also for the image resolution, as in contrast to epifluorescence microscopy, no scattered light from the areas below and above the focal plane of the objective adds to the primary emitted signal. To overcome the limitations of light absorption, two-side illumination can be used for big samples. In addition, to avoid shadow generation by obstacles in the sample, the light sheet can be turned around the detection axis using a Pivot scanner (Lightsheet Z.1 by Zeiss) or multiple light sheets can be introduced (UltraMicroscope II by LaVision BioTec). In the last years specialized LSFMs using Bessel beams¹⁶⁶, Airy beams¹⁶⁷ or lattice light sheet¹⁶⁸ as well as

combinations of LSFM and confocal^{169,170} or super-resolution techniques^{171,172} for higher resolution were developed. Furthermore, LSFM could be shown to strongly benefit from the employment of adaptive optics – a technique developed for removing scattering artifacts from astrophysical images¹⁷³.

2 Aim of the study

In order to understand the mechanisms of platelet generation, the spatiotemporal distribution of megakaryocytes in the bone marrow must be investigated. Recently, techniques of intravital microscopy and volumetric imaging of the intact murine bone marrow have challenged but not fully refuted the model of MK migration from the endosteal to the vascular niche. The first part of the thesis aims to provide novel methods and data supporting the model of stationary MK maturation. Intravital microscopy of murine bone marrow has not shown MK migration within the bone marrow. But the experiments were limited in the measurement duration. The present thesis aims to (I) establish long-term intravital two-photon microscopy and quantitatively investigate the megakaryocyte movement by mean squared displacement analysis. A vast majority of MKs in the BM are found in a direct contact with the vasculature. Nevertheless, it is not clear whether directed migration of the cells is the cause of strong vessel-association. A random spatial distribution of MKs in the bone marrow can largely exclude directed migration of these cells towards the vasculature. Thus, this study intends to (II) establish microscopy based computational modelling methods to test the randomness of cell distribution and to apply the technique to the light sheet microscopy images of MKs in the BM. MKs are thought to migrate from the regions close to the endosteum towards the vasculature during their maturation process. As a consequence, the vascularization and the density of mature MKs should differ in the bone associated and non-bone associated regions, the investigation of which is a further aim of this work (III).

Investigation of the acute phase of the ischemic stroke is essential for understanding and treating the reperfusion injury. So far, the reperfusion injury has been investigated by different biochemical and microscopic techniques and has been demonstrated to be a thrombo-inflammatory event, although the underlying mechanisms are still elusive due to limitations in the imaging techniques. Although platelet function strongly affects the outcome of ischemic stroke, there is no direct evidence for a role of thrombus formation during the thrombo-inflammatory processes. The second part of the thesis addresses (IV) the role of thrombus and platelet aggregate formation in the development of the cerebral ischemia reperfusion injury by developing volumetric microscopy and subsequent image analysis workflows for large brain regions. Furthermore, the study intends to (V) perform initial microscopy analysis of the involvement of vasculature and neutrophils in the early phase of the reperfusion injury.

3 Materials and methods

3.1 Materials

3.1.1 Reagents and chemicals

Acetic acid	Roth (Karlsruhe, Germany)
Agarose	Roth (Karlsruhe, Germany)
Antisedan	Orion Pharma (Espoo, Finland)
Atipam	Dechra (Hadnall, The UK)
Benzyl alcohol	Sigma Aldrich (Schnelldorf, Germany)
Benzyl benzoate	Sigma Aldrich (Schnelldorf, Germany)
Bovine serum albumin	AppliChem (Darmstadt, Germany)
Bromophenol blue	Sigma-Aldrich (Schnelldorf, Germany)
Buprenovet	Bayer Pharma (Berlin, Germany)
Cyanoacrylate	Weicon (Münster, Germany)
Disodium phosphate	Roth (Karlsruhe, Germany)
Dental cement	Dentsply (York, The USA)
Dexametasone	Pharma-Partner (Hamburg, Germany)
dNTPs	Fermentas (St.Leon-Rot, Germany)
Ethanol	Sigma Aldrich (Schnelldorf, Germany)
Ethylendiaminetetraacetic acid (EDTA)	AppliChem (Darmstadt, Germany)
Fentanyl	Janssen-Cilag (Neuss, Germany)
Fetal calf serum (FCS)	Perbio (Bonn, Germany)
Flumazenil	AlleMan Pharma (Pfullingen, Germany)
Glycerin	Roth (Karlsruhe, Germany)
Isofluran CP	cp-pharma (Burgdorf, Germany)
Isopropanol	Roth (Karlsruhe, Germany)
Medetomidine	Pfizer (Karlsruhe, Germany)
Methanol	Sigma Aldrich (Schnelldorf, Germany)
Midazolam	Roche Diagnostics (Mannheim, Germany)
Midori Green Advanced DNA stain	Nippon Genetics Europe (Düren, Germany)
Naloxone	AlleMan Pharma (Pfullingen, Germany)
Paraformaldehyde	Sigma Aldrich (Schnelldorf, Germany)
Phenol/chloroform/isoamyl alcohol	Roth (Karlsruhe, Germany)
Phosphate buffered saline (PBS)	Life Technologies (Darmstadt, Germany)

Proteinase K, recombinant, PCR grade	Thermo Fisher (Schwerte, Germany)
Sodium chloride	AppliChem (Darmstadt, Germany)
Sodium dodecyl sulfate (SDS)	Sigma-Aldrich (Schnelldorf, Germany)
2,3,5-triphenyltetrazolium chloride	Sigma Aldrich (Schnelldorf, Germany)
Tris(hydroxymethyl)aminomethane	Roth (Karlsruhe, Germany)
Tween 20	Roth (Karlsruhe, Germany)

3.1.2 Materials

18G x 1 ½", 20G x 1 ½", 26G x 1 ½"	
needlesBD	Biosciences (Heidelberg, Germany)
Glass coverslips (24 x 60 mm)	Roth (Karlsruhe, Germany)
Glass vials	Hartenstein (Würzburg, Germany)
Metal plate skull holder	Boer Metaal en Draad (Deil, The Netherlands)
Perma-Hand silk suture (4-0, 7-0)	Ethicon (Somerville, NJ, USA)
Perfusion pump, Ismatec 2 channels	Cole-Parmer (Wertheim, Germany)
Syringes (1 ml)	Dispomed (Gelnhausen, Germany)

3.1.3 Labeling kits and fluorophores

Alexa fluor 488 protein labeling kit	Life Technologies (Darmstadt, Germany)
Alexa fluor 546 protein labeling kit	Life Technologies (Darmstadt, Germany)
Alexa fluor 647 protein labeling kit	Life Technologies (Darmstadt, Germany)
Alexa fluor 750 SAIVI Rapid	
Antibody labeling kit	Life Technologies (Darmstadt, Germany)

3.1.4 Antibodies

Antibody	Clone	Isotype	Antigen	Company/Reference
p0p6	56F8	IgG2b	GPIX	home-made ¹⁷⁴
Anti-CD31	390	IgG2a	CD31	BioLegend
Anti-CD105	MJ7/18	IgG2a	CD105	home-made ¹⁷⁵
Anti-Ly6G	RB6-8C5	IgG2b	Ly6G	eBiosciences
p0p/B	57E12	IgG2b	GPIIb α	home-made ¹⁷⁶
INU1	11E9	IgG1	CLEC2	home-made ¹⁷⁷

3.1.5 Buffers and solutions

Antagonization against triple anesthesia

Atipamezole	2.5 µg/g BW
Flumazenil	0.05 µg/g BW
Naloxone	1.2 µg/g BW
In NaCl	

Clearing solution (BABB)

Benzyl alcohol	1 part
Benzyl benzoate	2 parts

Decalcification buffer

EDTA	10%
In PBS	

Loading dye solution (6x)

Tris buffer (15 mM)	33%
Glycerol	60%
Bromophenol blue	0.04%
In double-distilled water	

Lysis buffer for DNA isolation

Tris base	100 mM
EDTA	5 mM
NaCl	200 mM
SDS	0.2%
Proteinase K (20 mg/ml)	100 µg/ml

Paraformaldehyde, pH 7.2

PFA	4%
In PBS	

Phosphate buffered saline, pH 7.14

NaCl	137 mM
KCl	2.7 mM
KH ₂ PO ₄	1.5 mM
Na ₂ HPO ₄ (DSP)	8 mM

TAE buffer (50x)

Tris base	0.2 M
Acetic acid	5.7%
EDTA (0.5 M, pH 8.0)	10%

TE buffer, pH 8.0

Tris base	10 mM
EDTA	mM

Triple anesthesia

Medetomidine	0.5 µg/g BW
Midazolam	5 µg/g BW
Fentanyl	0.05 µg/g BW
In 0.9% NaCl	

3.1.6 Mice

C57BL/6JRj mice were obtained from Janvier Labs (Saint-Berthevin, France) and further held in the animal facility of the Rudolf Virchow Center Würzburg. *Rag1^{-/-}* mice¹⁷⁸ were held in the animal facility of Center of Molecular Medicine of University Würzburg. The temperature and humidity were constantly regulated *ad libitum* supply of food and water was given to the animals. Animal studies were approved by the district government of Lower Frankonia (Bezirksregierung Unterfranken) and carried out in accordance with local regulations.

3.1.7 Software

Imaris 7.7.2, 8.3.1, 9.1.1	Bitplane (Zurich, Switzerland)
Ilastik	179
Fiji	180
Matlab	MathWorks (Natick, USA)
SigmaPlot	Systat Software (Erkrath, Germany)
Microsoft Excel 2016	Microsoft Corporation (Redmond, USA)
Heyugens	Scientific Volume Imaging (Hilversum, The Netherlands)

3.2 Methods

3.2.1 Mouse genotyping by PCR

Isolation of mouse DNA was performed using ear punch samples. These were lysed in 500 µl DNA lysis buffer containing 2.5 µl Proteinase K. After incubating the samples overnight at 56°C under shaking conditions (900 rpm, Eppendorf Thermomixer) phenol/chloroform/isoamyl alcohol mixture (500 µl) was added to individual samples. Subsequently the samples were vigorously mixed by shaking and centrifuged at 10000 rpm for 10 min at room temperature. To the upper phase of a volume of approximately 440-500 µl isopropanol was added. Upon shaking, the mixture was centrifuged at 14000 rpm for 10 min at 4°C. The supernatant was discarded and the remaining DNA pellet was washed using 500 µl 70% ethanol. Subsequent to the washing step, the DNA was again centrifuged at 14000 rpm for 10 min at 4°C. The DNA pellet was dried at 37°C for 30 min and solubilized in 70 µl TE buffer for 30 min shaking at 500 rpm and at 37°C. For subsequent polymerase chain reaction (PCR) 1-2 µl of the DNA solution was used.

Primers:

Rag1_WT-F: 5' GAG GTT CCG CTA CGA CTC TG 3'

Rag1KO-F: 5' CCG GAC AAG TTT TTC ATC GT 3'

Rag1-R: 5' TGG ATG TGG AAT GTG TGC GAG 3'

Pipetting scheme:

DNA	1 μ l
Rag1_WT-F: 1:10	0.5 μ l
Rag1KO-F: 1:10	0.5 μ l
Rag1-R: 1:10	0.5 μ l
dNTP's (10 mM)	1 μ l
Taq-buffer (10x)	2.5 μ l
MgCl ₂	2.5 μ l
Taq-Polymerase	0.25 μ l
H ₂ O	16.25 μ l

PCR program:

96°C	3 min	
94°C	30 s	35 x
58°C	30 s	
72°C	45 s	
72°C	5 min	
HOLD 22°C		

Resulting band size:

WT: 474 bp

KO: 530 bp

For gel electrophoresis, 1.5 % agarose solved in 1x TAE buffer was boiled in a microwave and subsequently cooled down to approximately 60°C. Per 100 μ l solution 5 μ l Midori green were

added and the fluid was placed into a tray with a comb and allowed to solidify. The resulting gel was positioned in an electrophoresis chamber containing 1x TAE buffer. To 20 μ l DNA solution 4 μ l 6x loading dye solution were added and the samples were loaded into the gel slots. The gels were run for 30 min at 120-160 V. DNA ladder was used for size determination of the PCR products.

3.2.2 Transient middle cerebral artery occlusion (tMCAO)

Transient middle cerebral artery occlusion (tMCAO) model was used for investigation of reperfusion injury after ischemic stroke as described elsewhere¹⁸¹. 8-12-week-old mice were treated with an intraperitoneal injection of Buprenovet (10-20 μ g/g BW) 30 min prior the tMCAO surgery to enable sufficient analgesia. The animals were anesthetized with 2% Isoflurane in 70% N₂ 30% O₂ mixture and the body temperature was maintained at 37°C during the experiment. The surgical procedure was performed using a Leica stereo microscope and its duration was kept below 15 min. Middle cerebral artery (MCA) occlusion was achieved by advancing a silicon rubber-coated 6.0 nylon monofilament (Doccol, USA) into the right common carotid artery up to the circle of Willis and the MCA. 60 min after occlusion the filament was removed to allow reperfusion. Global neurological outcome and motor function of the mice were determined by using Bederson score and the grip test. The animals were either subjected to intravital imaging or *ex vivo* brain analysis after predefined time periods. The experiments were performed in accordance with the guidelines of the district government of Lower Frankonia.

For quantitative analysis of infarct volume, mice were sacrificed after a predefined time and brains were collected. The organs were cut in 2 mm slices and subsequently stained with 1% TTC solution for 15 min at 37°C. Stained brain samples were fixed with 4% PFA solution for 4-5 h. Planimetric analysis of TTC staining of brain sections was performed using Fiji software, as previously described elsewhere¹⁸¹. Brains with hemorrhages were excluded from the statistical analysis.

3.2.3 Mouse preparation for intravital imaging

For imaging of the murine bone marrow 6-8 weeks old wild type mice were anesthetized by intraperitoneal injection of triple anesthesia. Subsequently, megakaryocytes and blood vessels were intravitaly stained by intravenous injection of anti-GPIX Alexa546 (15 μ g/mouse) and

anti-CD105 Alexa488 (15 µg/mouse) antibodies, respectively. The hair covering the head of the animal was removed and the underlying skin was disinfected with 70% ethanol. An incision of 1.5 cm length was made along the midline of the skull. A custom designed metal plate was fixed to the skull with cyanoacrylate and mounted on a self-designed stereotactic frame to reduce head movement during the imaging session.

For imaging of the brain tissue a chronic open cranial window (OCW) was induced into the skull prior to intravital imaging. For this, 8-10-week-old mice were anesthetized by intraperitoneal injection of medetomidine (0.5 µg/g BW), midazolam (5 µg/g BW) and fentanyl (0.05 µg/g BW). To avoid brain swelling, the animals were subcutaneously injected with Dexametasone (0.2 mg/kg BW) before the surgical procedure. The hair at the site of the surgery was removed and the skin was disinfected with 70% ethanol. An incision of 1 cm length along the midline was made to expose the skull. A square-shaped area of ca. 0.5 cm side length was marked on the left or right side of the skull and the bone was thinned along square sides with a high-speed microdrill without damaging the midline of the skull. Subsequently, the square-shaped skull region was carefully removed with forceps without damaging the dura. A circular sterile coverslip was covered with a small drop of saline, placed on the craniotomed area and fixed with cyanoacrylate. Exposed skull was covered with dental cement. Subsequently the animal was injected with atipamezole (2.5 µg/g), flumazenil (0.05 µg/g) and naloxone (1.2 µg/g) to antagonize the triple anesthesia and allowed to recover for two weeks during which they were monitored daily. Directly before a multi-photon microscopy session the mice were anesthetized with triple narcotics and intravenously injected with anti-CD31 Alexa647 (15 µg/mouse), anti-GPIX Alexa546 (5 µg/mouse) and anti-Ly6G Alexa488 (10 µg/mouse) antibodies to fluorescently label the vasculature, platelets and the neutrophils, respectively. Subsequently, a custom designed metal plate was fixed to the open cranial window and mounted on a custom built stereotactic frame to reduce head movement during the imaging session.

3.2.4 Intravital imaging of mice by multi-photon microscopy

Multi-photon imaging of the murine bone marrow was performed with a standard configuration Leica TCS SP8 MP microscope (Leica Microsystems, Wetzlar, Germany) equipped with a 25x/1.00 IMM HC FLUOTAR motCORR VISIR objective. Ti-Sapphire Chameleon Vision II OPO MPX was used for excitation and the emission signal was detected by HyD-RDLs or PMT-NDDs. Z-stacks of 50 µm depth were imaged with a step size of 5 µm at a stack rate of 1 Hz.

Two-photon microscopy of the ischemic brain was performed using a TrimScope II multiphoton system (LaVision BioTec, Bielefeld, Germany) equipped with an Olympus 20x/0.95 water immersion objective. Excitation was achieved by a pulsed tunable broad-band Ti:Sa laser (Chameleon laser, Coherent, Germany). For emission detection HQ535/50 and ET605/70 filters were used. The hardware was controlled by ImSpector Pro-380 software. 15-30 min long time series were taken at a frame rate of 30 frames/s at different positions and for a total duration of 3-4 h for each mouse. The obtained images were maximum intensity projected over time using Fiji.

3.2.5 Light sheet fluorescence microscopy (LSFM) of cleared tissue

For the investigation of megakaryocytes in the murine bone marrow 8-12 weeks old mice were anesthetized with triple narcotics and intravenously injected with anti-GPIX Alexa750 (20 µg/mouse) and anti-CD105 Alexa647 (20 µg/mouse) antibodies stain for megakaryocytes and vasculature, respectively. 20 min after the intravital immunolabeling tissue fixation was performed by cardiac perfusion as previously described by others²⁵. Briefly, the mouse was fixed on a surgery table and the thorax was carefully opened without damaging the lungs or the heart. A 26G needle was inserted into the left ventricle of the heart and the right atrium was open by a small incision. 1x PBS was introduced into the circulation via the needle at a speed of 6 ml/min for 3-4 min till the blood was completely washed out of the animal. Subsequently, 4% PFA in 1x PBS was introduced into the circulation at the same speed for 8 min to fix the whole animal. After the successful perfusion fixation, sternum, femur and the bregma of the skull were harvested and postfixed with 4% PFA for 2 h. Bone sample preparation for LSFM was performed according to the method developed previously in the laboratory^{25,182}. Briefly, the bones were decalcified with 10% EDTA for 72 h, were then dehydrated in methanol solutions of increasing concentrations (50%, 70%, 95% and 100%) for a duration of 2 h each, and again stored in 100% methanol overnight. Decalcification and dehydration was performed at 4°C. Subsequently the samples were cleared in BABB solution for 4 h at room temperature and stored in fresh BABB solution at least for 12 h before imaging. For lungs and uncut brains every dehydration step was performed for 8-12 h and the samples were incubated with BABB for 12 h for the initial clearing.

LSFM imaging of ischemic brains at lower magnification was performed after perfusion fixation of the whole animal. High magnification LSFM of brain slices was performed after TTC staining.

In this case, the samples were fixed without cardiac perfusion in 4% PFA solution for 2 h and subsequently washed three times with 1x PBS at room temperature.

Optically cleared lung, bone or brain samples were imaged with custom-built light sheet fluorescence microscopes in the BioImaging Center of the Rudolf Virchow Center Würzburg. The low magnification LSF microscope was equipped with two EC Epiplan-Neofluar 2,5x/0,06 M27 excitation objectives (Zeiss, Germany) and a HCX PL FLUOTAR 5x/0.15 Dry detection objective (Leica, Germany). The laser illumination was achieved using diode lasers (Coherent OBIS LS: 488 nm 60 mW, 532 nm 50 mW, 561 nm 50 mW; Omicron LuXX: 642 nm 140 mW, 730 nm 40 mW) and controlled using acousto-optical tunable filter (AOTF). Light sheet was generated using a 6210H Galvanometer Scanner (Cambridge Technology). Emitted light was filtered (525/50 BrightLine HC, 582/64 BrightLine HC, 607/70 BrightLine HC, 697/58 BrightLine HC and 785/62 BrightLine HC) and detected by an Andor Neo 5.5 sCMOS camera. The high magnification LSF microscope was equipped with two EC Plan-Neofluar 5x/0,16 M27 (Zeiss, Germany) emission and one HCX APO L20x/0.95 IMM (Leica, Germany) objectives. AOTF controlled lasers (Cobolt Calypso Dual 491 nm and 532 nm, LuXX 642 nm and 730 nm) were combined with detection filters (525/50 BrightLine HC, 607/70 BrightLine HC, 697/58 BrightLine HC, 785/62 BrightLine HC). Both microscopes were controlled using Andor IQ 2.9 software.

Bone samples were imaged with a step size of 1 μm and brain samples with a step size of 0.5 μm when using the high magnification LSF microscope. For images at lower magnification step size in z direction was 2 μm . 500-1000 images per z-stack were acquired and stored as tiff files.

3.2.6 Image preprocessing, segmentation and quantitative analysis

3.2.6.1 Segmentation of megakaryocytes in lung and bone marrow

Image processing and data analysis of 3D LSF images of the bone marrow was performed as described in Stegner *et al*¹⁸². Namely, the images were first preprocessed in Fiji by using the median filter (diameter of 2 pixels) and removing the vessel signal from the MK channel. Small point like structures which frequently appear in the MK and vessel channels were removed by first creating binary imaging and subsequently detecting the objects with particle remover in Fiji which were then subtracted from the corresponding channels. Contrast enhancement was and background removal were performed in Imaris (normalization of the

layers, background subtraction) and in Fiji (3D Gauss filter and unsharp mask). To enable correct segmentation of MKs in Imaris software, artificial cell nuclei for MKs were created in Fiji. MKs were detected with Imaris software using the Cell module separately for small and big MKs.

Bone was segmented using the autofluorescence signal at 532 nm excitation wavelength by the machine learning based software Ilastik, which was trained for correct bone tissue detection for individual 3D LSFM stacks. Image preprocessing for background reduction and signal enhancement in Fiji was performed before the segmentation step. Segmented binary data were imported into Imaris for object generation. Bone-to-bone distance was assessed by using the Spots function in Imaris, generating spherical objects at local minima of the distance transformation map of the bone channel.

For detection of MKs in lung tissue, the 3D LSFM stacks were segmented for the cells using manual intensity threshold adjustment in Imaris software.

3.2.6.2 Segmentation of large thrombi in low magnification LSFM images of ischemic brains

Tiff images acquired by LSFM were deconvolved using Huygens software (signal-to-noise ratio: 40, background subtraction with nearest object) and exported as .h5 files. Deconvolved data was loaded into Ilastik and pixel classification for thrombi was performed using a pretrained algorithm. The results were exported as binary data and transferred to Imaris software together with the original and deconvolved thrombus channels as well as the vasculature channel. Thrombus detection in the pixel classified channel was performed using the Surface module of the software. The quantitative results were exported as Excel files and further analyzed with Matlab software. Final statistical analysis and graph generation was performed in SigmaPlot software.

3.2.6.3 Analysis of high magnification LSFM images of ischemic brains

Tiff images of platelet, vasculature and neutrophil channels acquired by LSFM were loaded into Imaris and maximum intensity projection (MIP) over Z-direction was performed. Resulting images were exported as three-channel tiff files. MIP images of the platelet channel were pixel classified using intensity thresholding (Yen method¹⁸³) in Fiji. In the resulting binary images, the total GPIX positive area or the total thrombus area were found using the particle analyzer

function in Fiji, where minimum thrombus area was set to 100 pixels and no limitations were assumed for GPIX-positive signal detection. For analysis of the anti-CD31 Alexa647 signal, the mean fluorescence intensity of MIP images was calculated. Neutrophil counting was performed manually. All values obtained from the MIP images were normalized by the number of planes of the corresponding 3D stack. Statistical analysis was performed using the SigmaPlot software.

3.2.7 Statistical analysis

Results are shown as mean \pm SD of each group if not stated otherwise. Differences between more than two groups were analyzed using OneWay ANOVA with Dunn's post-hoc test using the SigmaPlot software. P-values >0.05 were considered as statistically non-significant (ns); * $p<0.05$, ** $p<0.01$, *** $p<0.001$.

4 Results

4.1 Investigation of megakaryocyte presence, migration and spatial distribution

4.1.1 Long-term intravital imaging of megakaryocyte motility

Megakaryocyte motility in the bone marrow has been investigated by different groups^{24,25}. Nevertheless, the experiments were performed for only short time intervals of 30-60 min and did not differentiate between vessel-associated (VA) and non vessel-associated (NVA) megakaryocytes. To investigate MK motility at time scales of several hours, long term intravital imaging of mouse skull bone marrow was established and acquired MK trajectories were quantitatively analyzed.

4.1.1.1 Establishment of long-term intravital imaging of murine bone marrow

The method of intravital microscopy of the murine bone marrow, which was established by J. van Eeuwijk in our laboratory, made use of intravenous injection of tetramethylrhodamine (TMR) dextran for the visualization of the vasculature. Nevertheless, the TMR dextran signal decreases already after a short imaging period of 15 min and vessel signal cannot be distinguished from the background fluorescence after 45 min (

Figure 7A). Bleaching of TMR dextran, which results in a slightly decreased overall signal (

Figure 7A), could be overcome by repeated intravenous application of the marker via a jugular catheter. Nevertheless, TMR dextran leaks out of the discontinuous bone marrow vasculature as clearly shown by quantitative analysis of the fluorescence signal around the vessel in

Figure 7A: Over 45 min the TMR dextran signal increases in the bone marrow and builds a gradient from the vessel wall towards the inner area of the extravascular space (as indicated by an arrow in the intensity profile). Additional TMR dextran application could not overcome the loss of contrast caused by leakage, thus immunostaining of the vasculature was established. Two different endothelial cell markers – CD31 and CD105 – were immunolabeled by intravenous injection of fluorophore-conjugated corresponding antibodies, both leading to a stable signal for the endothelial cells for an imaging period of 3 h. As expected, anti-CD31 antibody bound endothelial cells as well as MKs and platelets (

Figure 7B), as the letter express CD31. To avoid the strong colocalization of MK and vasculature fluorescence channels resulting in inaccurate cell tracking, CD105 was further used for long-term intravital microscopy of the bone marrow.

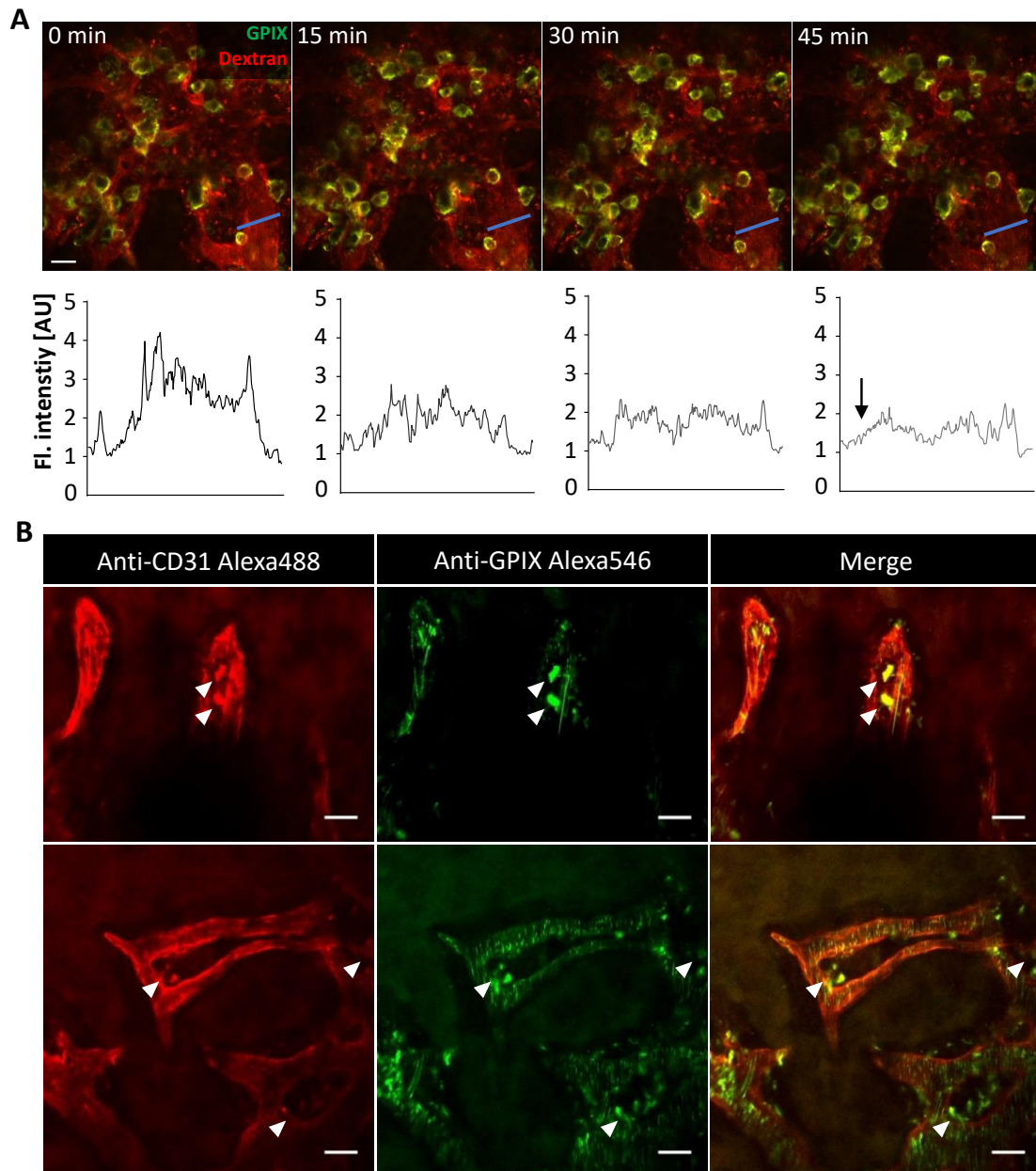


Figure 7. TMR dextran and anti-CD31 antibody are not suitable for long-term intravital fluorescence microscopy. **A** Intravital two-photon microscopy of mouse bone marrow (skull, bregma) was performed at a frame rate of 0.1 Hz. The MKs (and platelets) were immunolabeled with anti-GPIX Alexa488 and the vasculature was visualized by intravenous injection of TMR dextran. Upper panel: Four representative images at time points 0 min, 15 min, 30 min and 45 min are shown. Scale bar: 30 μ m. Lower panel: fluorescence intensity along the line (blue) indicated in the upper panel was quantified for the four time points. The arrow indicates the site of dextran leakage for the time point of 45 min. **B**

Intravital two-photon microscopy of mouse bone marrow (skull, bregma) was performed using anti-CD31 Alexa488 and anti-GPIX Alexa546 for immunostaining of the vasculature and MKs (and platelets), respectively. In the two representative examples (upper and lower panels), MKs clearly exhibiting double staining for CD31 and GPIX are indicated by arrows. Scale bar: 30 μm . Figure modified from Stegner *et al.*¹⁸²

4.1.1.2 Quantitative analysis of megakaryocyte motility in the bone marrow

MKs were imaged by intravital two-photon microscopy during 3 h at an inverse frame rate of 1 frames per second (fps) and subsequently the trajectories of the center of mass of individual cells were calculated. Tracking of individual MKs over time revealed no significant motility, but a wobbling-like movement (Figure 8A-B) at a velocity of $0.38 \pm 0.47 \mu\text{m}/\text{min}$ (at the time scale of $\tau = 1 \text{ min}$), which is in line with previous studies^{24,25}. To elucidate the impact of MK localization in respect to the bone marrow vasculature, cell movement was separately analyzed for vessel-associated (VA, 85% of all cells) and non vessel-associated (NVA, 15% of all cells) cells, showing no significant difference between the two groups (Figure 8B).

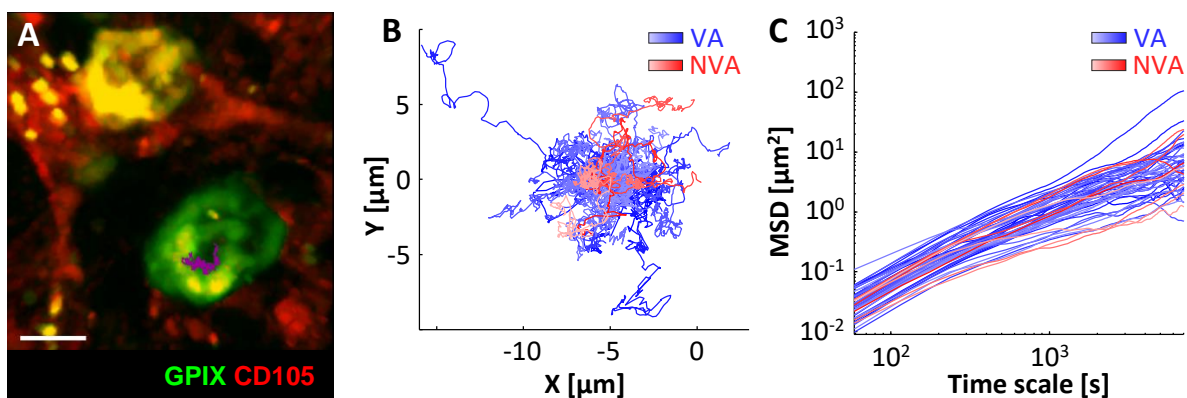


Figure 8. Intravital imaging of intact bone marrow reveals strongly diminished motility of megakaryocytes. Megakaryocytes (green) and bone marrow vasculature (red) were immunolabeled with an intravenous injection of anti-GPIX Alexa 488 and anti-CD105 Alexa 546 antibodies. Mice were subjected to intravital two-photon microscopy for a minimum duration of 3 h. **A** One representative trajectory (magenta) of the center of the mass of a MK is shown at 5x magnification. Scale bar: 15 μm . **B** Individual trajectories of all tracked megakaryocytes ($n = 54$ cells from 6 different animals) are shown in different blue (vessel-associated, $n = 46$) and red (non vessel-associated, $n = 8$) shadings. **C** Mean squared displacements for different time scales are shown in different blue (vessel-associated, $n = 46$) and red (non vessel-associated, $n = 8$) shadings. Figure modified from Stegner *et al.*¹⁸²

Next, mean squared displacement (MSD) analysis of individual MK trajectories was performed. Briefly, MSD can be connected to diffusive behavior by

$$MSD := \langle r^2(\tau) \rangle = 2nK_D\tau^\alpha$$

where n is the number of dimensions, K_D the time scale-dependent equivalent of the diffusion coefficient, τ the time scale and α the anomalous diffusion exponent. The anomalous diffusion exponent characterizes the motion type of the object, where values below 1 describe subdiffusive and values above 1 superdiffusive cases, while value 1 corresponds to Brownian motion. Both VA and NVA MKs displayed similarly low MSD values ($MSD_{NVA} = 0.0268 \pm 0.0086 \mu\text{m}^2$ and $MSD_{VA} = 0.0342 \pm 0.0183 \mu\text{m}^2$ for time scale of 1 min, $p = 0.301$, Mann-Whitney rank sum test) increasing very slowly over time (Figure 8C). The migration type was assessed by estimation of the anomalous diffusion exponent ($\alpha_{NVA} = 0.64 \pm 0.25$ and $\alpha_{VA} = 0.68 \pm 0.21$, $p = 0.661$, Student's t-test), which revealed a strongly subdiffusive motion for both vessel associated and non-vessel associated megakaryocytes.

In summary, megakaryocytes do not display any migration at time scales of 3 h, but rather a strongly subdiffusive wobbling-like movement. Furthermore, this slight movement is similar for VA and NVA MKs in respect of different motility parameters.

4.1.2 Investigation of megakaryocyte distribution in the bone marrow by computational modelling

In a previous work, van Eeuwijk succeeded in the reconstruction of the murine bone marrow (BM) vasculature and MKs in large bone marrow volumes using LSFM and found that the entire BM is densely vascularized and contains MKs²⁵. This finding indicates that there is no need for MK migration towards the vessels. To further support this hypothesis, MK localization relative to the vasculature needs to be performed.

4.1.2.1 Development and implementation of the algorithm for simulation of cell distribution

Directed MK migration towards the bone marrow vasculature would lead to a non-random special distribution of these cells. To elucidate whether cell distribution is random, the experimentally calculated data need to be compared to random data, which can only be produced by computer simulations. For this purpose, a Matlab-based algorithm was developed, allowing to predefine different cell shapes and a stable template into which cells are randomly placed. The main goal for algorithm development was a direct usage of 3D image

stacks (acquired by LSFM of the murine bone marrow) for the simulations to allow realistic *in silico* investigation by computational modelling. Consequently, the algorithm is voxel-based and all objects, such as vasculature or cells, are represented by 3D tensors. Furthermore, the algorithm performs sequential addition of MKs into the simulation space. The algorithm has no restrictions concerning the size and shape of the template or the cells. The quality of the simulation is limited only by the spatial resolution of the used image stacks, which can be improved either by increased imaging resolution or interpolation of voxel values.

Instead of using binary images of the vasculature, a distance transformation map (DTM) of the channel is used as a template, allowing direct calculation of cell-to-vessel distances. Each voxel value V represents the distance to the next vascular neighbor: $V < 0$ for vessel lumen, $V = 0$ for vessel wall, $V > 0$ for intravascular space. The vasculature DTM of size $d_1 \times d_2 \times d_3$ is converted into a tensor D of type (d_1, d_2, d_3) where D_{ijk} corresponds to the voxel values of the DTM. In addition, a second tensor B of type (d_1, d_2, d_3) is introduced, which represents a binary image of the vasculature:

$$B_{ijk} = \begin{cases} 1, & \text{if } D_{ijk} \leq 0 \\ 0, & \text{if } D_{ijk} > 0 \end{cases}$$

The algorithm is able to include different cells into the simulation, enabling to predefine the size and sphericity distribution of simulated MKs. All m binary MK image stacks are transformed into 3D tensors C_p of individual sizes $(p_1 + 1, p_2 + 1, p_3 + 1)$, where $C_{p,ijk} = 1$ represents voxels belonging to a cell and values outside of the cell are set to empty “not a number (NaN)”. Before the actual simulation, the number of simulated MKs n and the sequence of used MK tensors are predefined. In addition, a tensor M of size (d_1, d_2, d_3) is generated, where at the beginning of the simulation all values are set to 0 and are changed when a MK is added to the space (Figure 9).

For random addition of a new m^{th} cell into the bone marrow space, first, a point outside the vasculature with $B_{ijk} = 0$ is randomly chosen and the cell is placed. Consequently, the cell with the tensor C_p will occupy the space $([i, i + p_1], [j, j + p_2], [k, k + p_3])$. If $i + p_1 > d_1$, $j + p_2 > d_2$ or $k + p_3 > d_3$ the cell is partially located outside the template and a new position for the cell is chosen.

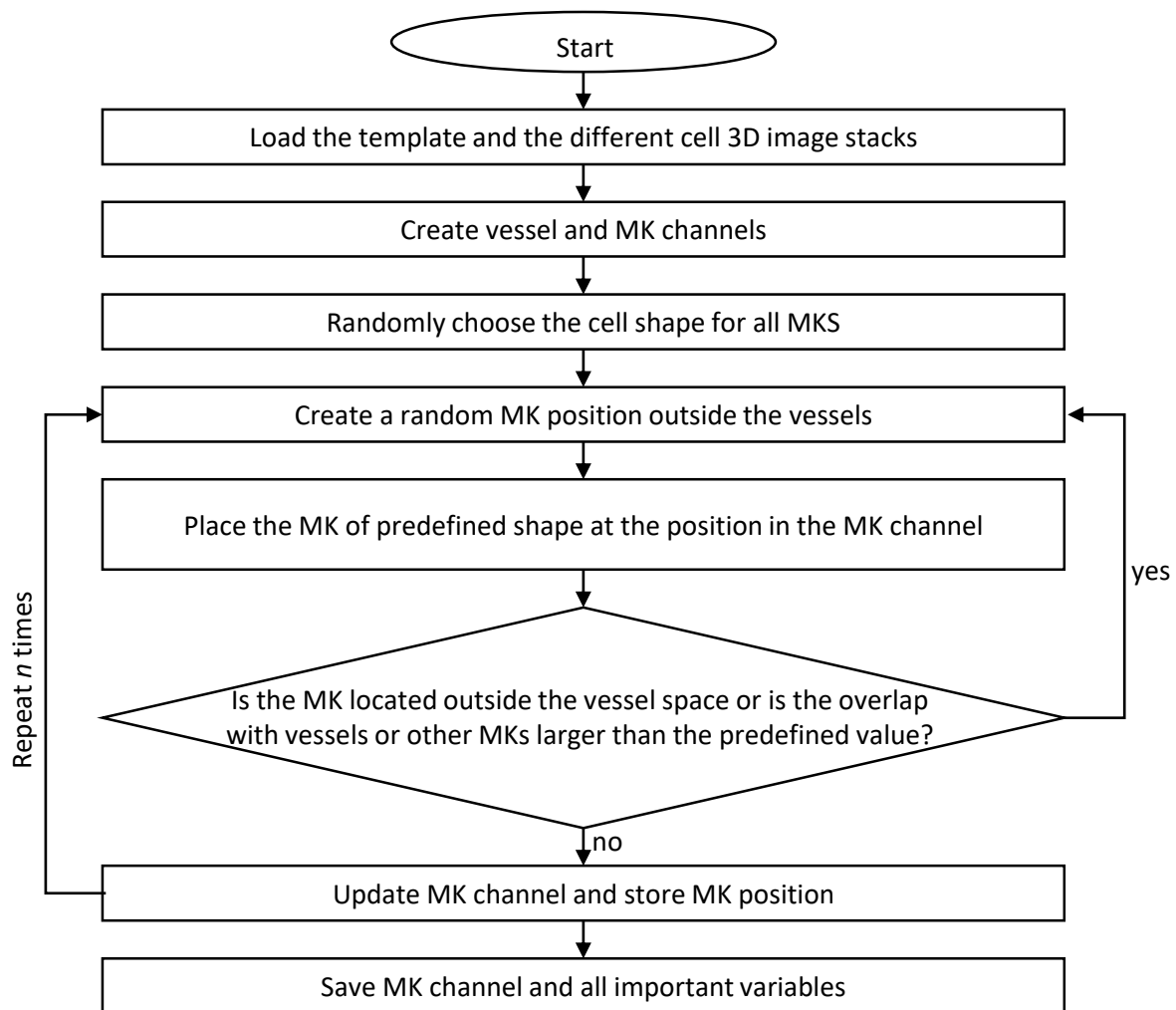


Figure 9. Simplified algorithm for simulation of megakaryocyte distribution in the bone marrow. 3D microscopy image stacks of the vasculature and single MKs are loaded and converted into 3D tensors and a virtual space for MKs is created. MKs are placed cell by cell into the MK space in a way that the colocalization with the vasculature or other MKs does not exceed a predefined value. Figure modified from Gorelashvili *et al.*¹⁸⁴

Next, the overlap of the m^{th} cell with the vasculature or other MKs is calculated:

$$O^{VC} = \sum_{i,j,k} O_{i+\tilde{p}_1, j+\tilde{p}_2, k+\tilde{p}_3}^{VC} = \sum_{i,j,k} B_{i+\tilde{p}_1, j+\tilde{p}_2, k+\tilde{p}_3} C_{\tilde{p}_1, \tilde{p}_2, \tilde{p}_3}$$

$$O^{MC} = \sum_{i,j,k} O_{i+\tilde{p}_1, j+\tilde{p}_2, k+\tilde{p}_3}^{MC} = \sum_{i,j,k} \sigma(M_{i+\tilde{p}_1, j+\tilde{p}_2, k+\tilde{p}_3} C_{\tilde{p}_1, \tilde{p}_2, \tilde{p}_3})$$

where

$$\sigma(x) = \begin{cases} 1, & \text{if } x > 0 \\ 0, & \text{if } x = NaN \end{cases}$$

and $\tilde{p}_1, \tilde{p}_2, \tilde{p}_3 \in \mathbb{N}, \tilde{p}_1 \in [1, p_1], \tilde{p}_2 \in [1, p_2], \tilde{p}_3 \in [1, p_3]$. If the overlaps O^{VC} and O^{MC} exceed predefined values, a new position for the cell is chosen. Otherwise MK tensor M is modified to M' as follows:

$$M'_{i+\tilde{p}_1, j+\tilde{p}_2, k+\tilde{p}_3} = m \cdot M_{i+\tilde{p}_1, j+\tilde{p}_2, k+\tilde{p}_3}$$

Such a modification of the MK tensor results in MKs distinguishable by unique voxel values and thus facilitates cell segmentation for visualization purpose. In addition, cell-to-vessel distance is calculated as the infimum value of $B_{i+\tilde{p}_1, j+\tilde{p}_2, k+\tilde{p}_3}$. The last step of the algorithm stores cell-to-vessel distances and the tensor M (Figure 9).

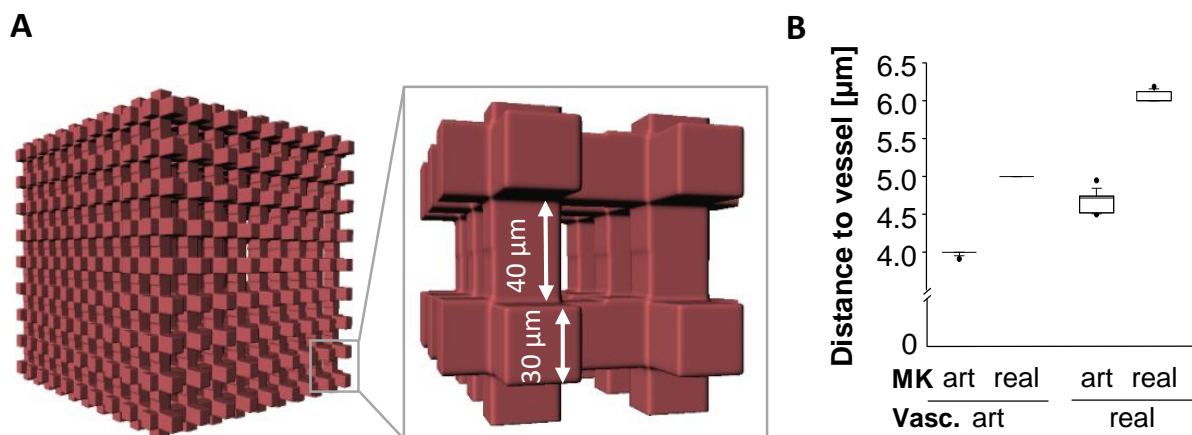


Figure 10. Artificial vascular network or megakaryocytes reduce cell-to-vessel distance in computational simulations compared to LSFM derived data. **A** An artificial vessel network was designed with a vessel size of 30 μm and intravascular distance of 40 μm mimicking the physiological structures. **B** Artificial (spherical) and real MKs were randomly distributed in the artificial or real vascular networks. MK distribution relative to the vasculature was characterized by cell distance to the nearest vessel. Median MK-to-vessel distances were calculated for artificial and real MKs simulated in artificial and real bone marrow vasculature ($n = 10$ simulation with 700 cells for each group). $p < 0.001$ (One-way ANOVA) and $p < 0.05$ for all pairs (Student-Newmann-Keuls-Test). Figure modified from Gorelashvili *et al.*¹⁸⁴

Often cell simulations are performed with artificially designed structures mimicking the physiological templates. Still, it is not clear, if this approach is suitable for systems of a highly

variable and irregular shape like bone marrow vasculature and MKs. To elucidate this aspect of computational modelling, artificial vasculature network with vessel size of 30 μm and vessel-to-vessel distance of 40 μm (in accordance with the data acquired by LSFM) (Figure 10A) and artificial spherical MKs of 20 μm diameter (corresponding to the mean MK diameter of LSFM data) were created in Fiji. Simulation of MK distribution was performed with artificial and the real vasculature and MKs. As the most important measure for cell distribution, median MK-to-vessel distance was calculated for each simulation, revealing significantly decreased values for the artificial vasculature network compared to the real vessels for both artificial ($3.99 \pm 0.03 \mu\text{m}$ vs. $5.00 \pm 0.00 \mu\text{m}$) and real MKs ($4.67 \pm 0.14 \mu\text{m}$ vs. $6.04 \pm 0.07 \mu\text{m}$). Furthermore, replacing real MKs by spherical objects results in a significantly decreased distance to the vessel. In summary, the results suggest that cell distribution simulations for highly irregular bone marrow vasculature and MKs should be performed based on real data acquired by microscopy experiments to achieve physiologically relevant results.

4.1.2.2 Semi-random distribution of megakaryocytes in the bone marrow

To investigate the process of potential megakaryocyte migration, computational modelling of MK distribution in the bone marrow was performed, where cell density and cell size and sphericity distributions were adjusted to the experimentally acquired data and vasculature template as well as cell images from LSFM data were used. First, the simulations were performed with a maximum of 5% overlap (of cell volume) of individual MKs with the vasculature. Compared to the real data, the simulation resulted in a markedly increased cell-to-vessel distance and a low proportion of vessel-associated (VA) MKs (

Table 1 and Figure 11A). To exclude simulation-related bias resulting from the rigid character of the used cell and vasculature templates, the value of allowed cell-vessel overlap was increased. Nevertheless, the MK-to-vessel distance and proportion of VA MKs could not be reproduced for any investigated overlap parameter (

Table 1). These data indicate that megakaryocytes are not fully randomly distributed in the bone marrow.

Table 1. Megakaryocyte-to-vessel distance and proportion of vessel-associated cells in a random simulation of cell distribution for different cell-vessel colocalization parameters. Data shown as mean \pm SD. MK: megakaryocyte; NVA: non-vessel associated; VA: vessel associated.

	Maximal MK-vessel overlap [% of MK volume]					
	5%	10%	25%	50%	100%	Real data
MK-to-vessel distance of all MKs [μm]	5.0 \pm 5.8	4.7 \pm 5.8	4.4 \pm 5.9	3.8 \pm 5.8	3.1 \pm 5.4	2.1 \pm 4.3
MK-to-vessel distance of NVA MKs [μm]	7.4 \pm 5.7	7.5 \pm 5.7	8.1 \pm 6.0	8.1 \pm 6.1	8.2 \pm 5.9	7.1 \pm 5.3
Proportion of VA MKs [%]	33	37	46	53	63	70

A non-random distribution can potentially result from two different processes: directed cell migration towards the vasculature or directed growth of VA MKs. The first will result in a non-random distribution of the entire MK population, while the latter will not affect NVA cells. Consequently, the distribution of non-vessel associated MKs was investigated. For this, the stable template was redefined to the joint volume of the vasculature and VA megakaryocytes and only NVA MKs were simulated. The MK-to-vessel distance of NVA cells was indistinguishable for the real data and simulation results (Figure 11B).

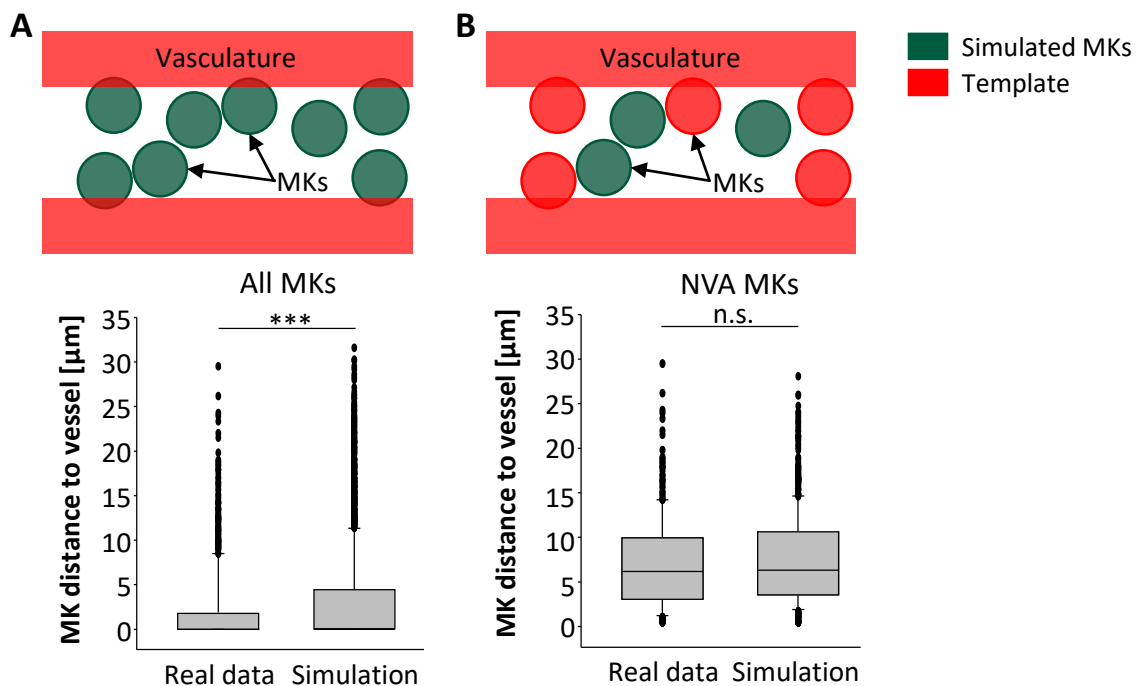


Figure 11. Megakaryocytes exhibit vessel biased random distribution in the bone marrow. A Megakaryocytes (green) were randomly placed into the unoccupied space (white) of the template (red), which in this case corresponds to the bone marrow vasculature. Cell number and cell size and sphericity distributions were adjusted to the physiological values. The maximal overlap between cell and vessel structures was set to 5% of cell volume. MK distance to the vasculature was compared between the real data and the simulation. *** $p < 0.001$ (Student's t-test). **B** Non vessel-associated (NVA) megakaryocytes (green) were randomly placed into the unoccupied space (white) of the template (red), which in this case corresponds to the bone marrow vasculature and vessel associated MKs. Cell number and cell size and sphericity distributions were adjusted to the physiological values. n.s. $p > 0.05$ (Student's t-test).

In summary, megakaryocytes are not randomly distributed in the bone marrow, but rather exhibit a vessel-biased distribution. Nevertheless, NVA MKs are randomly distributed, indicating that no directed migration towards the vasculature takes place. The underlying mechanisms for the localization bias of VA MKs remain unclear.

4.1.3 Quantitative analysis of megakaryocyte distribution throughout the bone in different bone types

So far, investigation of megakaryocyte migration towards the vasculature was investigated using intravital bone marrow imaging and computational modelling of the spatial distribution of these cells relative to the vessels. The results from both studies indicate that MKs do not migrate towards the vascular niche.

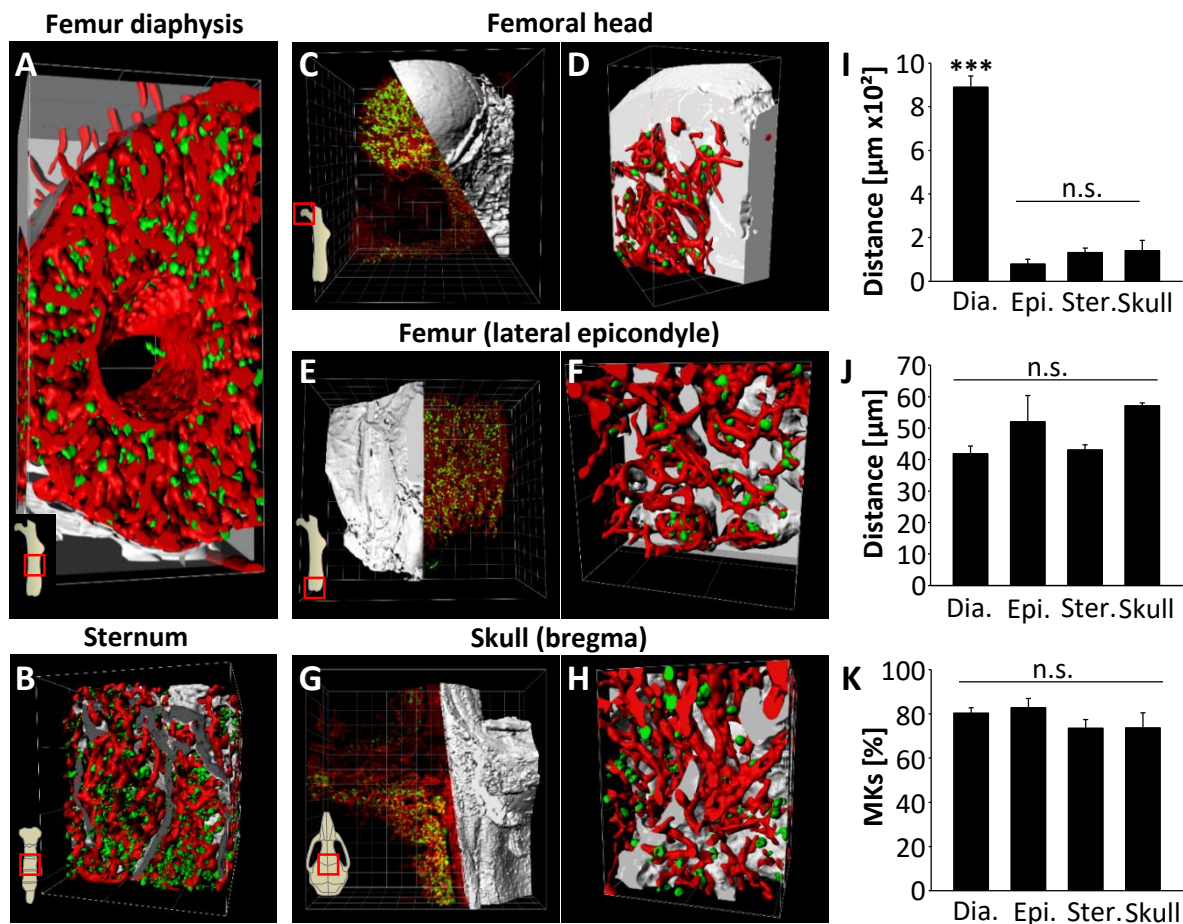


Figure 12. LSFM of bone marrow reveals full vascularization and megakaryocyte appearance in the entire organ in different bone types. A-H Vasculature (anti-CD105 Alexa 647, red), megakaryocytes (anti-GPIX Alexa750, green) and bone (autofluorescence at 532 nm, grey) were imaged by LSFM in optically cleared long bones (femur diaphysis (A)) and trabecular bones (sternum (B), femur head (C-D), femur epiphysis (E-F) and skull (G-H)). The overview images (C, E and G) of segmented bone structure, non-segmented vasculature and MKs as well as high magnification pictures (A-B and D, F and H) of segmented bones, vasculature and MKs reveal that both long bones and trabecular bones are highly vascularized and contain MKs. Grid size 200 μm . Bone-to-bone distance **I**, vessel-to-vessel distance **J** and percentage of vessel associated megakaryocytes (MKs) **K** were calculated for femur diaphysis (Dia), femur epiphysis (Epi), sternum (Ster) and skull. Except the significantly high bone-to-bone distance in femur diaphysis originating from the overall bone geometry, the different bone types display similar features. Bar graphs represent mean \pm SD. n.s. $p > 0.05$ One-way Anova, *** $p < 0.001$ (Mann–Whitney U test). Figure modified from Stegner *et al.*¹⁸²

Nevertheless, MK distribution analysis was previously performed only in femur diaphysis and sternum (Figure 12A-B), i.e. in relatively large bones, leaving the question open whether smaller trabecular bones exhibit a different vascularization pattern and megakaryocyte density due to their spongy structure, acting as reservoirs of MK progenitors. To investigate these aspects, cleared small trabecular bones such as femur head (Figure 12C-D), lateral epicondyle

(Figure 12E-F) and skull (Figure 12G-H) were imaged by LSM at lower and higher magnifications. Bone marrow vasculature and megakaryocytes, which were immunolabeled by using anti-CD105 Alexa 647 and anti-GPIX Alexa 750 antibodies, respectively, were found in the entire inter-bone space. Here, the inter-bone space was reconstructed by segmentation of the bone tissue based on autofluorescence signal at 532 nm excitation wavelength using machine learning segmentation software. These descriptive data already indicate that regions lacking mature MKs and potentially containing only MK progenitor cells (in accordance with conservative models of the endosteal niche) cannot be detected in long bones or trabecular bones (Figure 12A-H). Furthermore, vascularization and MK densities are comparably high in all samples. Quantitative analysis of the mean bone-to-bone distance reflected the differences between the long bones and the trabecular bone types, since femur diaphysis showed significantly higher values compared to femur epiphysis, sternum or skull ($890.5 \pm 50.8 \mu\text{m}$ vs. $78.9 \pm 20.5 \mu\text{m}$, $130.8 \pm 21.5 \mu\text{m}$ or $140.1 \pm 47.0 \mu\text{m}$, respectively). However, the results also show that the three investigated trabecular bones are indistinguishable in this aspect (Figure 12I). The bone marrow vascularization was analyzed by calculating the vessel-to-vessel distance, which, interestingly, is similar for all samples (Figure 12J) and thus corroborates the qualitative findings from Figure 12A-H. Furthermore, the vessel association of MKs was comparable with $80.3\% \pm 2.5\%$, $78.9\% \pm 4.3\%$, $73.5\% \pm 4.0\%$ and $73.7\% \pm 6.7\%$ for femur diaphysis, femur epiphysis, sternum and skull, respectively (Figure 12K), indicating that MK distribution relative to the vasculature is not affected by MK-to-bone distance.

As previously demonstrated, MK distribution is partially determined by the cell-to-vessel distance. Further analysis reveals, that median MK-to-bone and vessel-to-bone distances slightly differ in individual bone samples, but are strongly correlated (Pearson's coefficient of 0.836) (Figure 13A). This indicates that the cell distribution is primarily dependent on the localization of the vasculature and not on the distance to the bone. For more detailed analysis, MKs were categorized as bone-associated (BA) and non-bone associated (NBA) for cell-to-bone distances of below or above $100 \mu\text{m}$, respectively (Figure 13B). In femur diaphysis (Figure 13C) as well as in the trabecular sternum (Figure 13D) BA and NBA MKs were associated to the vasculature to the same extent (femur BA: $84.3\% \pm 3.1\%$, femur NBA: $78.8\% \pm 5.3\%$, sternum BA: $72.7\% \pm 3.9\%$, sternum NBA: $65.8\% \pm 9.5\%$) and also the cell-to-vessel distance of NVA MKs was similar for both groups (femur BA: $9.25 \pm 2.09 \mu\text{m}$, femur NBA: $9.49 \pm 1.42 \mu\text{m}$, sternum BA: $8.18 \pm 0.21 \mu\text{m}$, sternum NBA: $7.66 \pm 1.26 \mu\text{m}$). Furthermore, NBA and BA MKs display the same size distributions (femur BA: $30.9 \pm 2.2 \mu\text{m}$, femur NBA: $31.6 \pm 1.8 \mu\text{m}$, sternum BA: $34.4 \pm 1.9 \mu\text{m}$, sternum NBA: $29.9 \pm 1.5 \mu\text{m}$). In

summary, these results show that only localization relative to the vasculature, but not to the bone determines MK distribution in the bone marrow.

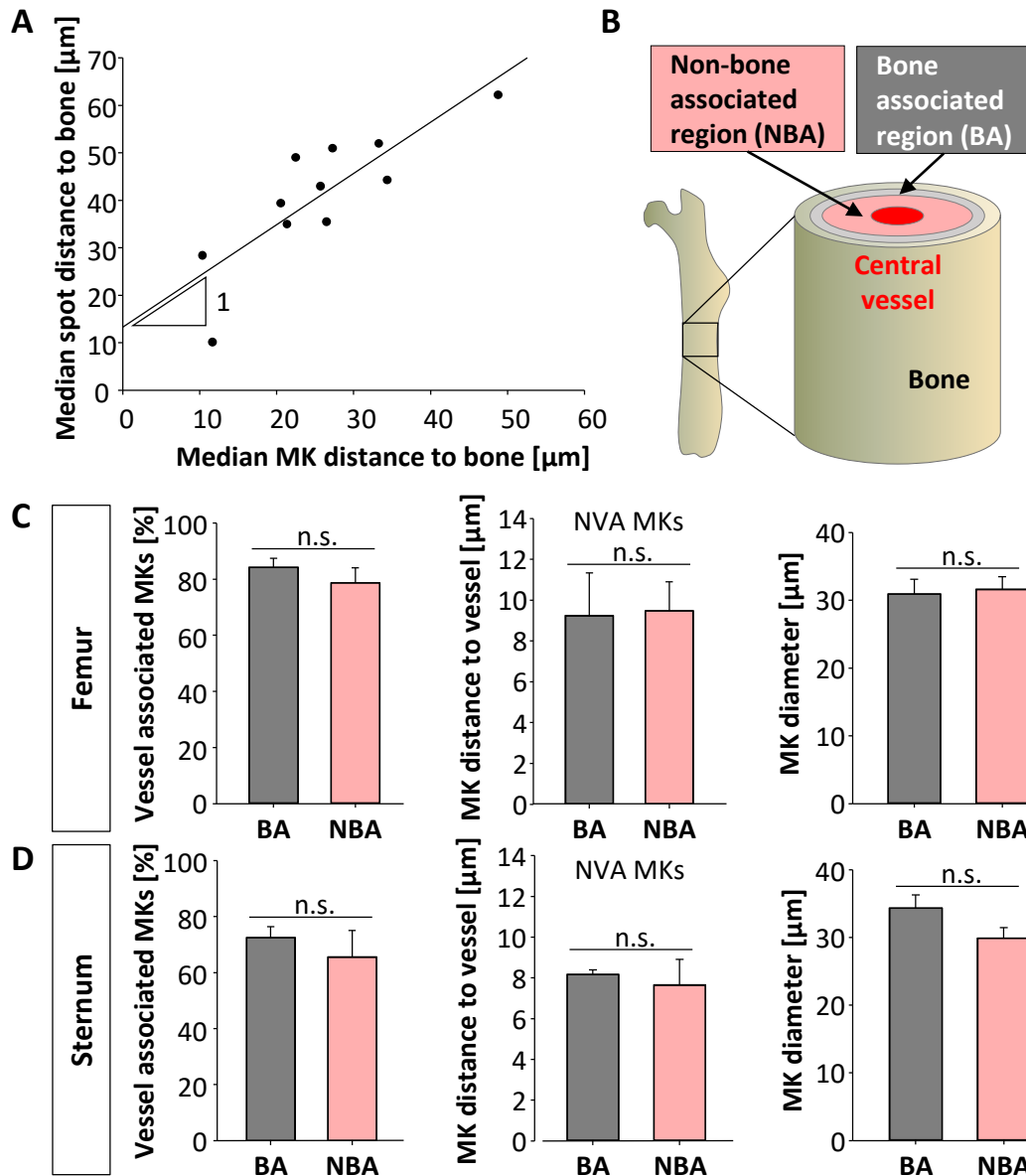


Figure 13. Megakaryocyte distribution is independent of cell-to-bone distance. **A** The correlation of the median MK-to-bone distance and the median vessel-to-bone distance for all 3D LSFM image stacks including long bones as well as trabecular bone types was found to be linear with a slope of 1 (Pearson's coefficient 0.836, $p < 0.01$). **B** MKs were categorized as non bone-associated (NBA, cell-to-bone distance below 100 μm) or bone-associated (BA, cell-to-bone distance above 100 μm). Percentage of vessel associated MKs, MK-to-vessel distance and MK diameter were calculated for NBA and BA MKs in long bones femur **C** and trabecular sternum **D**. NVA: non vessel-associated. Bar graphs represent mean \pm SD. $n = 4$. n.s. $p > 0.05$ (Student's t-test). Figure modified from Stegner *et al.*¹⁸²

4.1.4 Megakaryocytes in the murine lung

Megakaryocyte appearance and thrombopoiesis in the lung have been controversially discussed in a number of publications. Recently, Lefrançois *et al.* reported a remarkably high number of pulmonary MKs in mice suggesting the lung being a major site of thrombopoiesis³³. Nevertheless, the study was performed by intravital two-photon imaging limiting the volume of the analyzed tissue and thus exacerbating reliable measurement of MK numbers.

To review the finding by Lefrançois *et al.*, light sheet fluorescence microscopy of murine lungs was established by adjusting dehydration and optical clearing procedures for this tissue type. For a reliable estimation of MK density in murine lungs, different pulmonary areas from three different animals were imaged by LSFM, with a single stack volume size of 0.11-0.26 mm³. Figure 14A-B show a representative 3D image stacks of lung tissue and bone marrow of the sternum, revealing marked differences in MK density in these samples. Quantitative analysis of data revealed a MK density of 15.33 ± 7.055 1/mm³ in the lungs, which is 260-1100 times lower compared to the values in different types of bone marrow (femur diaphysis: 11145 ± 2655 1/mm³, femur epiphysis: 4036 ± 690.4 1/mm³, sternum 15802 ± 1078 1/mm³, skull 3987 ± 225.4 1/mm³) (Figure 14C).

Next, total MK numbers in femur, sternum and the lungs were estimated using the calculated cell density and total tissue volumes. Pulmonary MKs ($(10.7 \pm 8.6) \times 10^3$ MKs) constituted 1.3% of the joint MK population of lungs, femora ($(668.7 \pm 27.6) \times 10^3$ MKs) and sternum ($(158.0 \pm 21.6) \times 10^3$ MKs) (Figure 14D). On the other hand, investigation of the bone marrow by LSFM revealed that $1.99\% \pm 1.63\%$ of MKs are fully located intravascularly, while intravital imaging showed even lower values of 0.89%. A part of these MKs must be transported by the venous blood flow and thus, directly guided to the pulmonary tissue.

In summary, the lung is not a major site of platelet generation as the vast majority of MKs resides in the bone marrow.

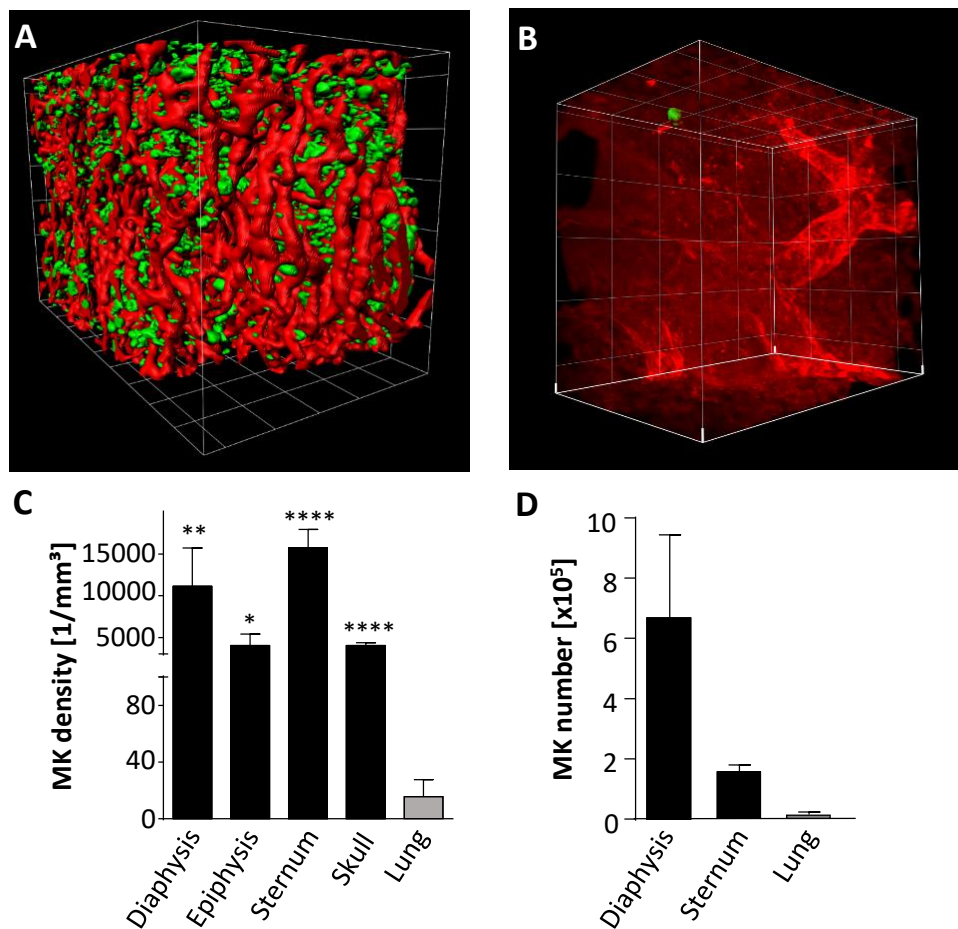


Figure 14. Lung is not a major site of thrombopoiesis in mice. **A-B** Light sheet fluorescence microscopy image of mouse sternum reveals a high density of megakaryocytes **A**, while almost no MKs can be found in the pulmonary tissue **B**. The vasculature (red) and the MKs (green) were intravenously immunolabeled with anti-CD31 Alexa647 and anti-GPIX Alexa750, respectively. **C** MK density in femur diaphysis and epiphysis, sternum and skull is higher compared to the density in the lungs (N=3-4 mice). Bar graphs represent mean \pm SD, * $p < 0.05$, ** $p < 0.01$, **** $p < 0.0001$ (Student's t-test). **D** Total MK numbers were calculated by multiplying the density of MKs in femur diaphysis, sternum and the lung by the estimated volumes of these organs.

4.1.5 Impact of MKs on cell migration in the bone marrow in simulation studies

According to the findings presented in the previous chapters, MKs are present in all regions of the bone marrow in high numbers and, due to their size, occupy large volumes. Thus, these cells can potentially hinder migration of other BM cells such as hematopoietic stem cells (HSCs) and neutrophils. To investigate this effect, an algorithm was developed, which uses LSFM-derived data, and allows computational simulation of cell migration in the bone marrow.

4.1.5.1 Development and implementation of the algorithm for simulation of cell migration

The cell migration algorithm is based on the computation modeling program described above and uses real microscopy-derived 3D images of bone marrow vasculature and MKs as templates and during migration single steps are simulated assuming a fixed step duration. Figure 15 provides a simplified structure of the major processes of the developed algorithm. First, the template is loaded and vessel and MK space tensors are generated to later enable cell-vasculature and cell-MK overlap calculations. Subsequently, the 3D image of the migrating cell is loaded and a corresponding 3D tensor is built. The starting position $\vec{P}(t = 0)$ of the migrating cell is randomly generated according to the algorithm for MK distribution simulation. Next, a random i^{th} step vector $\vec{S}(t = i)$ is generated depending on different parameters. The step is performed in 3D, where in each direction discrete values of a normal distribution function of predefined mean value and standard deviation are taken as basic instantaneous velocity. In addition to the basic velocity, chemotaxis effects can be added. The source of the attractive or repulsive chemotactic signal can be any predefined template, which in this special case was chosen to be the vasculature. The signal displays a linear gradient and thus correlates with the distance transformation map of the template. The signal is detected by cell membrane voxels and the net attraction is calculated for all three dimensions. The net attraction is then multiplied with a predefined chemotaxis parameter C to calculate additional step size. This approach reflects the physiological chemotactic sensing mechanisms of different types of cells. To simulate cell migration without chemotaxis, the parameter C was set to the value 0. At every step the cell is moved to the new position $\vec{P}(t = i) = \vec{P}(t = i - 1) + \vec{S}(t = i)$, which is calculated by the addition of the previous position and the step vector. If the migrating cell leaves the template or has an overlap with a MK, the cell is moved back to the previous position with $\vec{P}(t = i) = \vec{P}(t = i - 1)$. This step enables to mimic the phase of no movement, which is needed for cytoskeleton reorganization due to change of the direction of migration. If the cell does not collide with a MK or leave the template, its overlap with the vasculature is calculated. Here, the algorithm gives the possibility to simulate the process of a cell entering the blood flow by introducing a predefined probability. In case of intravasation, the simulation will be stopped and all following positions will be stored as $\vec{P}(t \geq i) = \vec{P}(t = i)$. Otherwise, $\vec{P}(t = i)$ is stored and a new step is simulated. After a predefined number n of positions, the simulation is stopped and all data are saved.

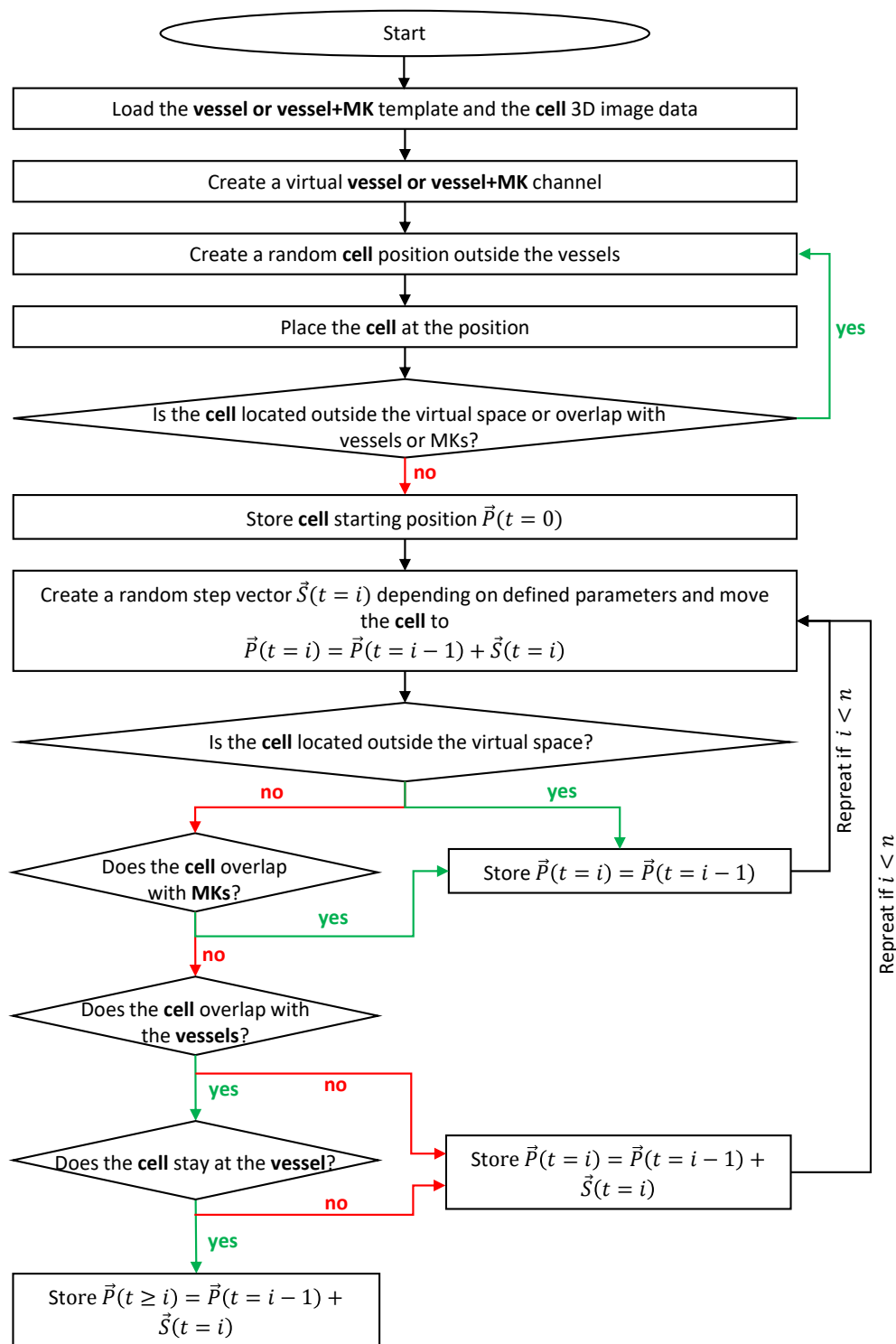


Figure 15. Simplified algorithm for simulation of cell migration in the bone marrow. 3D microscopy image stacks of the vasculature (and MKs) and images of migrating cells are loaded and converted into 3D. The migrating cell is placed into the template in a way that the colocalization with the vasculature or other MKs does not exceed a predefined value. Cell migration is performed with steps of random size in all directions or according to virtual chemotaxis and cell-vessel adhesion effects. Figure modified from Gorelashvili *et al.*¹⁸⁴

4.1.5.2 Megakaryocytes strongly hamper cell migration in the bone marrow

Physiologically, HSCs and neutrophils are recruited to the peripheral blood during stem cell mobilization or inflammatory processes, respectively. To analyze the influence of MK presence in the bone marrow on the time needed for HSCs or neutrophils to reach the vasculature, simulated cell migration was compared in templates with or without MKs. The diameter and the sphericity of the artificially designed HSC were adjusted to the physiological values. The cells were allowed to randomly migrate in the inter-vascular space at high or low velocities¹⁸⁵ and the number of steps until the first contact with a bone marrow vessel was assessed, assuming that the cell would subsequently migrate into the intraluminal space. In addition, mean squared displacement analysis of cell trajectories was performed for different time scales to characterize the migration. The results reveal that MKs markedly reduce cell motility. Namely, the number of steps needed to reach the vasculature is strongly increased in the presence of MKs (Figure 16A) for both cell types at high instantaneous velocities of $3 \pm 2 \mu\text{m}/\text{step}$. Furthermore, the corresponding HSC and neutrophil trajectories exhibited decreasing MSD values (Figure 16B-C) in presence of MKs. Lowering the instantaneous cell velocity to $2 \pm 1 \mu\text{m}/\text{step}$ further suppressed cell migration (Figure 16A). Interestingly, the hampering effect of MKs was more pronounced for cells migrating at lower velocities (Table 2).

Table 2. Number of steps until vessel entrance. HSC: hematopoietic stem cell; Prob-EV: probability for the cell to enter the vessel after a contact with the vasculature; V^{high} : high velocity of $v = 3 \pm 2 \mu\text{m}/\text{step}$; V^{low} : low velocity of $v = 2 \pm 1 \mu\text{m}/\text{step}$; C: parameter for chemotaxis, where for $C = 0$ the effect is absent. Data are presented as mean \pm SD

			Without MKs		With MKs	
			HSC	Neutrophil	HSC	Neutrophil
Prob-EV = 100%	V^{high}	C = 0	513 \pm 1107	628 \pm 1270	8057 \pm 10310	7869 \pm 10175
		C = 0.1	346 \pm 850	228 \pm 442	4988 \pm 7763	2553 \pm 4384
	V^{low}	C = 0	8100 \pm 13162	7406 \pm 12767	19694 \pm 13924	20541 \pm 13626
		C = 0.1	6807 \pm 12390	4915 \pm 10958	18404 \pm 14299	16160 \pm 14499
Prob-EV = 50%	V^{high}	C = 0	625 \pm 1315	654 \pm 1172	10753 \pm 11606	8783 \pm 10645
		C = 0.1	317 \pm 560	309 \pm 545	7291 \pm 9450	3944 \pm 5645
	V^{low}	C = 0	7862 \pm 13028	8015 \pm 13100	21675 \pm 13164	21872 \pm 13068
		C = 0.1	6900 \pm 12472	5225 \pm 11146	20121 \pm 13832	16107 \pm 14415

According to previous studies, cell migration in the bone marrow can be guided by chemotactic processes^{15,16,186}. To analyze the impact of these processes, chemotaxis was implemented into the cell migration algorithm, where the vessel walls were assumed to be the source of the chemoattractant. Furthermore, the algorithm was extended by an adjustable probability for entering the vessel lumen (Prob-EV) to reflect a more physiological cell migration process. Increasing the chemotactic parameter guiding the cells towards the vasculature, significantly decreased the number of steps needed for reaching and entering the vasculature and increased the corresponding MSD values for both investigated Prob-EV of 100% and 50% (Figure 16E-F and Table 2). Remarkably, while no significant difference could be found between HSCs and neutrophils in the absence of chemotaxis, in its presence neutrophils appeared to enter the vasculature faster than HSCs. As expected, reducing Prob-EV from 100% to 50% increased the time until entering the vasculature, but did not change the MSD values (compare Figure 16C and Figure 16G). Simulation results also show that for Prob-EV of 50% neutrophils reached the vasculature significantly faster than HSCs even in the absence of chemoattractants (Figure 16E-F and Table 2). In other words, cell size can have an effect on migration to the vasculature, and this effect can even be augmented by biophysical parameters such as chemotaxis and cell-to-vessel adhesion probability.

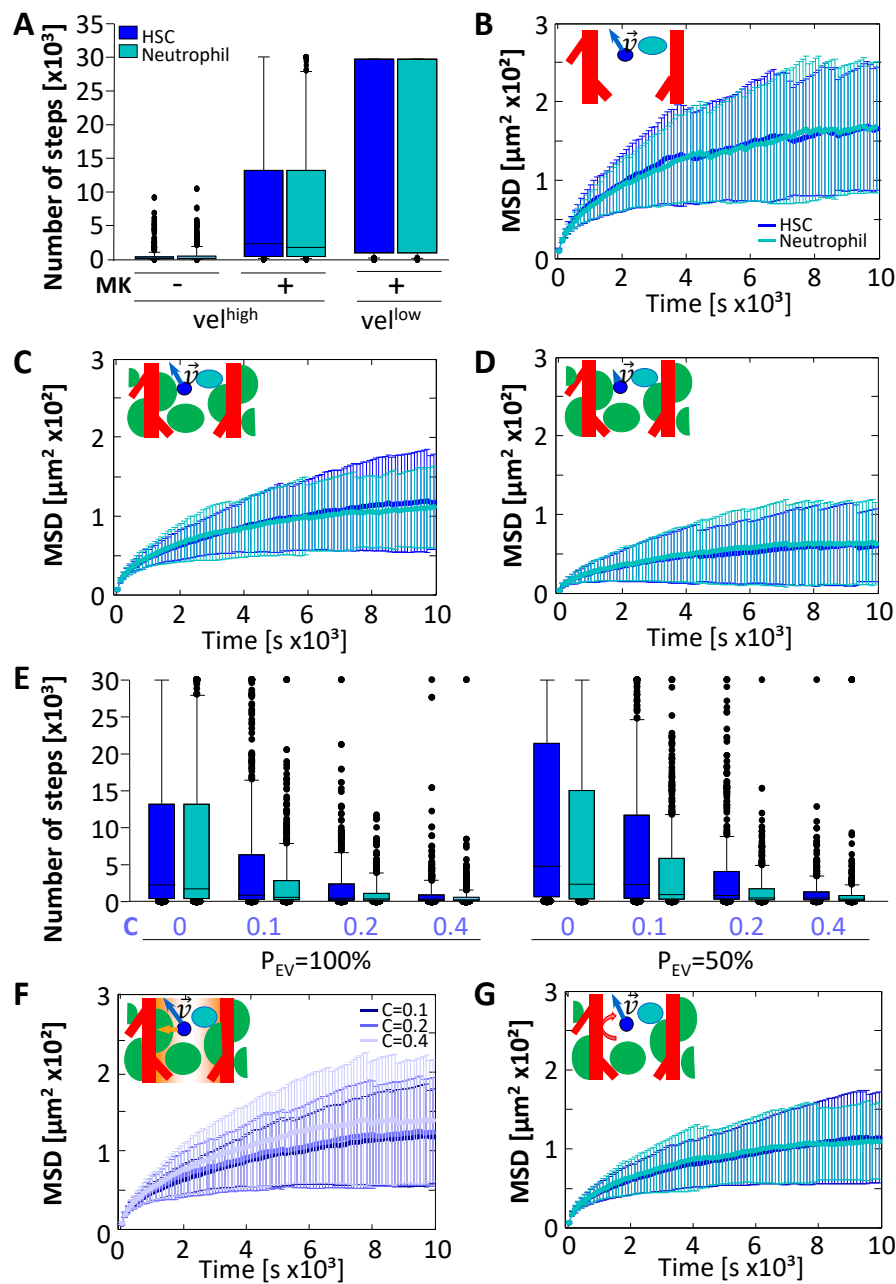


Figure 16. Strong inhibition of cell migration by megakaryocytes in the bone marrow can be compensated by chemotaxis. **A** Number of steps until entering the vessel lumen for artificial HSCs (blue) and neutrophils (cyan) migrating in the bone marrow with or without increased crowdedness resulting from the presence of MKs at high and low instantaneous velocities of $V^{\text{high}} = 3 \pm 2 \mu\text{m}/\text{step}$ and $V^{\text{low}} = 2 \pm 1 \mu\text{m}/\text{step}$, respectively. Probability for entering the vessel lumen after contact (Prob-EV) was set to $P_{\text{EV}} = 100\%$ and chemotaxis was absent ($C = 0$). Mean squared displacement (MSD) of HSC and neutrophil trajectories for **B** The MK-free template at high velocities and MK-containing template at high **C** and low **D** velocities. $P_{\text{EV}} = 100\%$ and $C = 0$. **E** Number of steps until entering the vessel lumen for $P_{\text{EV}} = 100\%$ and $P_{\text{EV}} = 50\%$ for increasing chemotaxis parameter $C = [0; 0.1; 0.2; 0.4]$ in presence of MKs. **F** MSD analysis of HSC migration data from **E** for $P_{\text{EV}} = 100\%$. **G** MSD analysis of HSC and neutrophil migration data from **E** for $P_{\text{EV}} = 50\%$ and $C = 0$. $N = 600$ for each simulation type. Figure modified from Gorelashvili *et al.*¹⁸⁴

4.2 Investigation of ischemic stroke and reperfusion injury

In the last decade many important factors for the development of ischemia reperfusion injury after stroke have been identified, such as platelets and immune cells. Nevertheless, the exact mechanisms of their contribution to tissue damage is still unclear. Light microscopy gives an opportunity to directly visualize the behavior of these cells in affected brains and to look for potential interactions.

4.2.1 Investigation of thrombus formation during I/R injury

4.2.1.1 Workflow for investigation of I/R injury after stroke by light sheet fluorescence microscopy

The reperfusion injury has been investigated by different imaging techniques, such as wide-field or confocal fluorescence microscopy of thin brain sections, intravital imaging by multiphoton microscopy and magnetic resonance imaging. Nevertheless, the first two techniques are associated with dramatic loss of information due to limited imaged volume and the latter lacks the resolution needed for studying cell-cell interactions. Thus, a light sheet fluorescence microscopy workflow was established for investigation of ischemic mouse brains.

Mice were subjected to tMCAO model with a duration of 60 min (Figure 17A). As previously discussed in the introduction, tMCAO is one of the most frequently used models in stroke research well reproducing the pathology of I/R injury in humans. The frequently used duration of 60 min mimics a typical situation when the affected patient can be treated within the therapeutically relevant time frame of 0-4.5 h after stroke by thrombolysis and/or thrombectomy. Shorter (30 min) or much longer (>3 h) tMCAO durations mostly lead to a very mild damage or to irreversible large-area tissue death, respectively, which do not reflect the reperfusion injury.

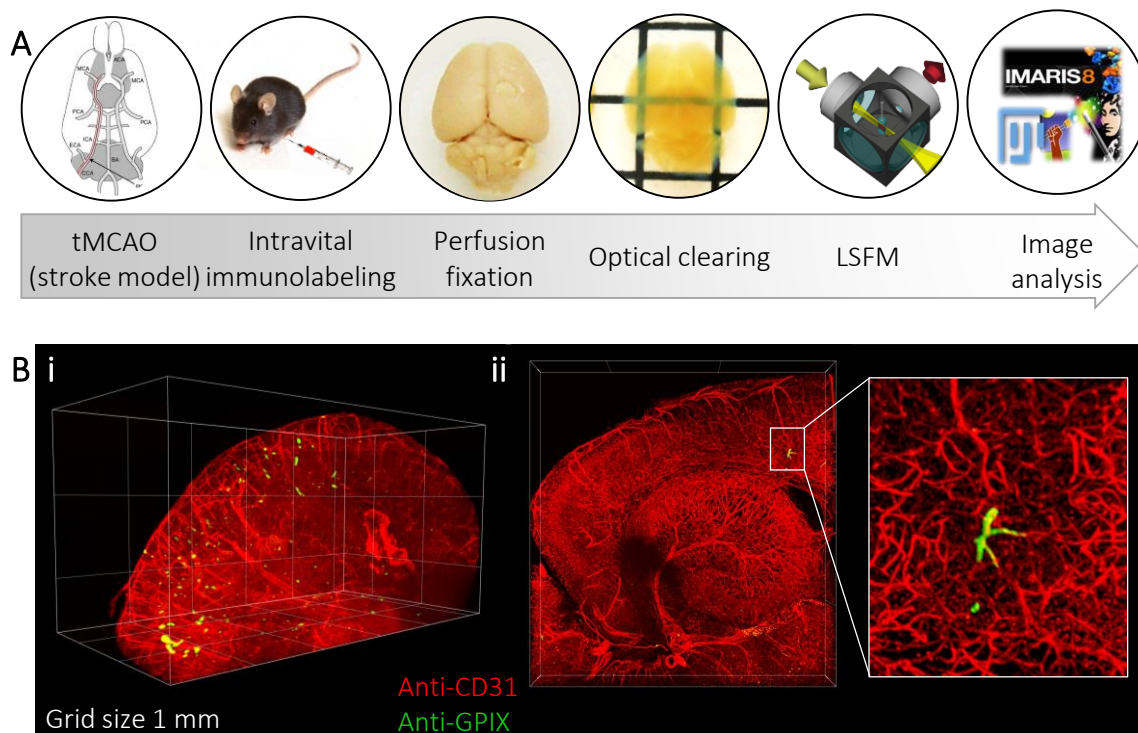


Figure 17. Light sheet fluorescence microscopy to study large ischemic mouse brain samples. **A** 8-12 weeks old mice were subjected to the transient middle cerebral artery occlusion (tMCAO) model of ischemic stroke. The animals were intravenously injected with fluorophore-bound antibodies for immunostaining of ECs (anti-CD31 Alexa647) and platelets (anti-GPIX Alexa750). Subsequently, the animals fixed by cardiac perfusion, the brains were harvested, optically cleared and imaged with a LSFM microscope. Acquired 3D image stacks were processed using deconvolution, segmentation and object recognition software. **B** (i) 3D reconstruction of an entire LSFM image stack prior to image processing containing the vasculature (red) and platelet channels (green), and (ii) a thin slice of the image stack demonstrates the ability of the technique to image small brain vessels and thrombi throughout the big-size sample. Grid size: 1 mm.

After reperfusion, the mice were subjected to immunolabeling using intravital injection of fluorophore-bound antibodies against the proteins of interest (Figure 17A). For immunostaining of platelets, a specific IgG derivative antibody against glycoprotein IX (GPIX) was used. It has been previously shown that this antibody is highly specific for platelets and does not affect their functionality. For immunostaining of the brain vasculature, antibodies against CD105 and CD31 were used while the latter enabled better signal to noise ratios in the LSFM images. Neutrophils were targeted using anti-Ly6G antibody. The dosage of used antibodies was fully sufficient for successful staining without interfering with the activity of the respective cell type. The alternative method, where the tissue is first permeabilized using detergents and subsequently stained with fluorophore-conjugated antibodies was tested for CD31 and GPIX staining (data not shown), but it was found to require exact optimization and long incubation

time to achieve homogenous labeling due to slow antibody penetration. In contrast, intravenously injected antibody is delivered to the whole organism via blood flow and, thus, enables a faster and a more homogenous staining of the tissue compared to immunolabeling after organ removal. One limitation for intravenous immunostaining is the permeability of blood vessels which is irrelevant when only the surface proteins of endothelial cells and blood cells such as platelets, neutrophils or T cells are targeted.

Prior to organ harvesting at a predefined time point after reperfusion, the mice were fixed using cardiac perfusion with paraformaldehyde (4% in PBS) (Figure 17A). In consequence, higher penetration depth during microscopy, due to reduced light absorbance by red blood cells, was achieved. In addition, a more homogenous and rapid tissue fixation can be performed by this method compared to fixation after organ removal where the slow diffusion speed of PFA is the limiting factor. The fixed brains were optically cleared using the solvent-based BABB clearing method. Here, the different durations (2 h, 4 h, 8 h, 12 h) of dehydration steps were tested and the optimal value of 8-12 h leading to improved clearing results was determined. The cleared brains were imaged using a low magnification (5x) light sheet fluorescence microscope to map thrombi in the entire organ. Imaged brain regions were reconstructed using the 3D rendering software Bitplane Imaris (Figure 17B). The resolution of the microscope was sufficient to detect small capillaries and platelet aggregates (Figure 17B).

Murine brain tissue samples show high autofluorescence signals. Thus, strong immunostaining for small objects of interest such as platelets is essential to obtain high signal to noise ratios in the microscopic images. This was addressed by using stable and bright fluorophores and by increasing the antibody concentration from 5 $\mu\text{g}/\text{animal}$ to 10 $\mu\text{g}/\text{animal}$. Further increase of antibody concentration did not affect the platelet signal intensity presumably due to saturation of the GPIX receptors on the platelet surface by antibodies. Figure 18A shows a representative slide from a 3D LSFM image stack at the emission wavelength of 750 nm where the anti-GPIX-Alexa750 signal as well as the autofluorescence of the brain can be clearly seen. While in regions *a* and *b* the signal of the platelet aggregates is higher compared to the low and homogenous autofluorescence of the neighboring tissue, in region *c* the autofluorescence of the brain is bright and appears in a structured-manner. The respective intensity profiles (Figure 18B) of lines shown in zoom-in images of Figure 18A indicate comparable intensities of platelet aggregates from regions *a* and *b* and the autofluorescence in region *c*. Consequently, thrombus segmentation based only on signal intensity fails in this case and a more complex method had to be established to obtain reliable results.

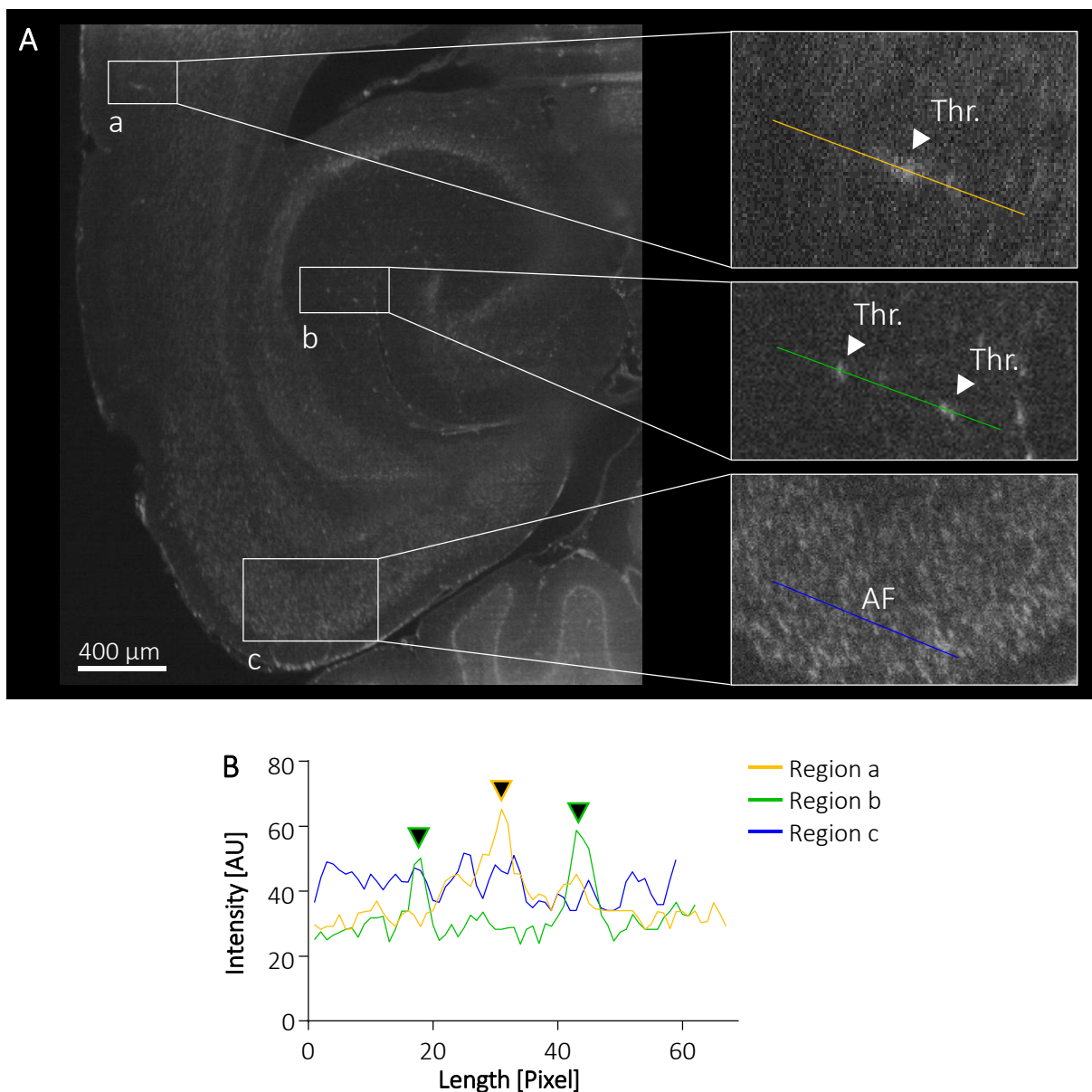


Figure 18. Brain area dependent inhomogeneity of thrombus intensity in LSFM images. **A** A representative single plane from 3D LSFM image of the signal at 750 nm shows inhomogeneous autofluorescence (AF) intensities for different brain regions. Zoom-in pictures show that the autofluorescence of neuron somata (region c) is comparable to the brightness of anti-GPIX Alexa750 labeled thrombus (Thr.) signal (arrows in the images of regions b and c) **B** Intensity profile along the lines in zoom-in images from A. Line colors are matched in A and B. AU: arbitrary units.

The image processing workflow established for platelet aggregate detection in ischemic brains consists of three main parts: deconvolution, machine learning based segmentation and object detection with subsequent quantitative analysis. Deconvolution was performed using theoretical point spread function for light sheet fluorescence microscopes and it increased the

resolution and the signal to noise ratio of the images. For the machine learning based pixel classification, the intensity and its gradients at different length scales were used to achieve good segmentation results. In the last step, the binary images of segmented thrombi were processed with the “Surface module” of Imaris software to detect platelet aggregates as objects and the corresponding characteristics, such as size and volume, of the objects were exported. Correct differentiation of platelet signal and autofluorescence was manually verified for every 3D stack.

4.2.1.2 Quantitative analysis of thrombus formation in murine brains after tMCAO

Most experimental studies investigate the outcome of the ischemia reperfusion injury 24 h after stroke by assessing the total infarcted brain volume and with the help of neurological scoring assays of the animals. Previous studies have shown that platelet GPIIb/IIIa and T cells play a major role in the reperfusion injury as mice treated with GPIIb/IIIa blocking Fab-fragment p0p/B or Rag1-deficient mice (lacking B and T cells) are largely protected in the tMCAO model^{93,129,131,132}. Despite the strong impact of platelets on the outcome of stroke, and experimental data, which argues against a contribution of platelet aggregation on infarct progression⁹³, thrombotic activity is still widely seen as one cause for the breakdown of the microcirculation^{113,187}. Therefore, we assessed a potential correlation between thrombus formation and infarct progression by thrombus mapping in ischemic brains of wild type, *Rag1*^{-/-} and p0p/B Fab treated mice 24 h after stroke using LSM. Thrombus formation was significantly reduced in murine brains after GPIIb/IIIa blockade compared to the vehicle-treated wild type mice, while *Rag1*-deficient animals showed a strong tendency to reduced thrombus number and total thrombus volume (Figure 19B-F). These results indicate that there is a positive correlation between thrombus formation and infarct area. Nevertheless, these data do not provide information on the causality of these processes, i.e. it is unclear whether platelet aggregation leads to tissue death and poor neurological outcome. It has been previously shown that intravenous injection of Fab-fragments of the anti-CLEC-2 antibody INU1 induces rapid platelet activation and thrombus formation in different organs including the brain and is mostly lethal ca. 20 min after intravenous injection⁵⁷. LSM images of INU1-Fab treated mice showed markedly increased number and size of thrombi compared to wild type mice after tMCAO (Figure 19A-B). These results indicate that the amount and total volume of thrombi in the wild type mice 24 h after stroke is comparably small and it is unlikely that these platelet aggregates are causative for severe tissue damage or poor neurological outcome.

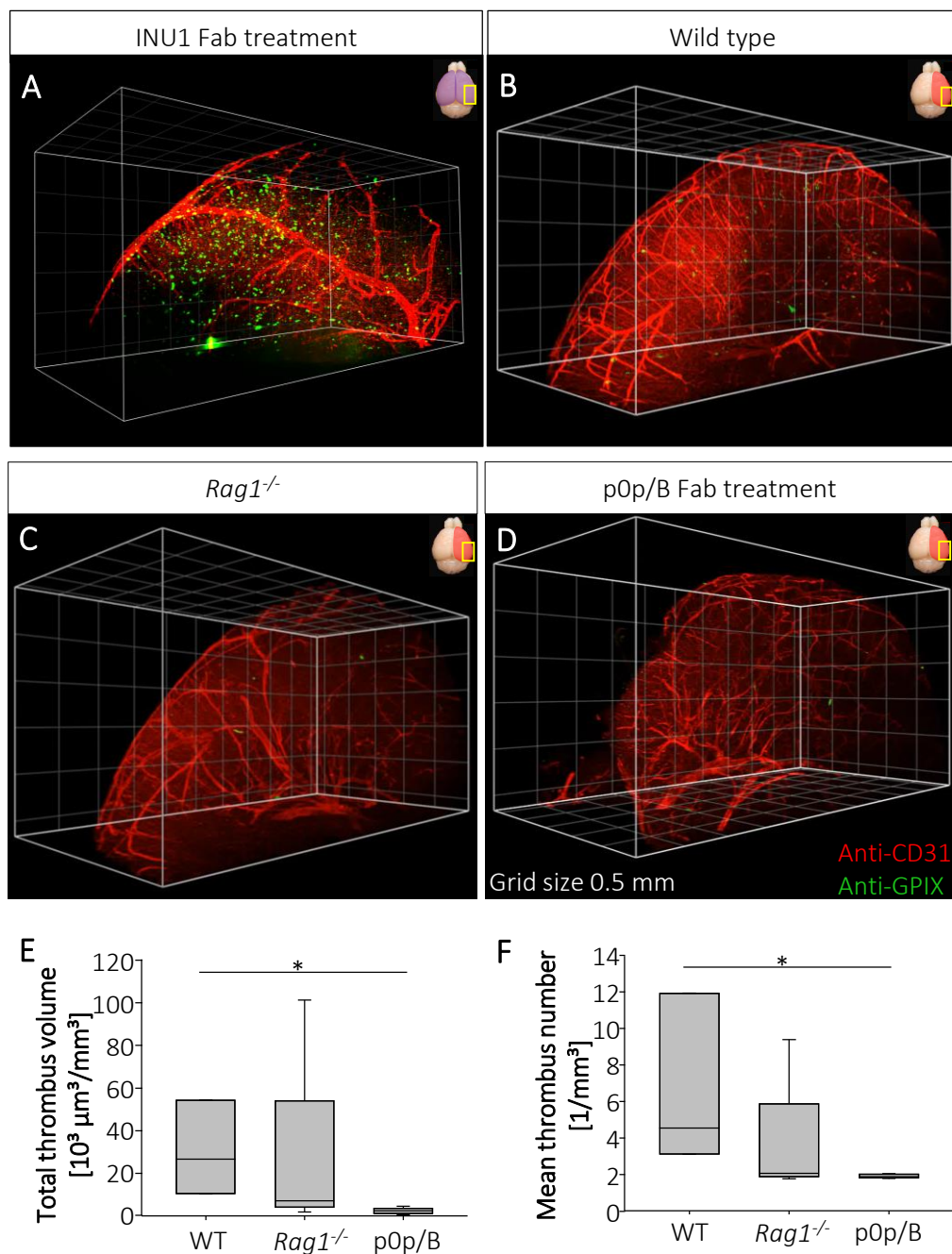


Figure 19. Thrombus formation in wild type, *Rag1*-deficient and p0p/B Fab treated animals 24 h after stroke reflects the severity of the I/R injury. A Representative 3D LSFM image of platelets (anti-GPIX Alexa750, green) and brain vasculature (anti-CD31 Alexa647) in an INU1 fab treated animal shows formation of large thrombi. B-D Wild type animal (B) shows less thrombus formation 24 h after tMCAO in the affected hemisphere compared to the positive control, while genetic *Rag1*-deficiency (C) and usage of GPIIb-blocking antibody (D) are associated with almost no thrombus formation. E-F Quantitative analysis of total thrombus volume (E) and mean thrombus number (F) for wild type (n=3), *Rag1*-deficient (n=5) and GPIIb blocked (n=5) animals shows a clear tendency for correlation of neurological protection and reduced thrombus formation 24 h after tMCAO. The values are normalized by imaged brain volume. Kruskal-Wallis One Way ANOVA on Ranks, $p < 0.05$; Multiple comparison procedures (Dunn's Method) $p < 0.05$ for wild type and GPIIb blocked groups.

After detecting a correlative relationship between thrombus formation and tissue damage in ischemic brains, platelet aggregation was investigated at different time points of the acute I/R injury. Schuhmann and coworkers were able to show that the volume of infarcted tissue increases over time and peaks 8 h after reperfusion (Department of Neurology, University Hospital Würzburg, personal communication). To identify a potential effect of thrombus formation on tissue damage, mouse brains in the early (2-4 h), intermediate (8 h) and late phases (24 h) of acute I/R injury were analyzed using LSFM. Representative 3D reconstruction of the caudal parts of the ipsilateral hemispheres (Figure 20A-D) and quantitative analysis of numbers and the total volumes of thrombi in both caudal and rostral parts showed that the thrombus formation mainly takes place in the late phase of I/R injury (Figure 20E-F). The values of the number and the total volume of thrombi for the early and intermediate phases were comparable to control animals (pooled untreated and sham operated mice). These results indicate that significant thrombus formation takes place hours after the time point where irreversible tissue damage has reached the maximal volume. In consequence, thrombus formation is not the cause for cerebral damage following tMCAO.

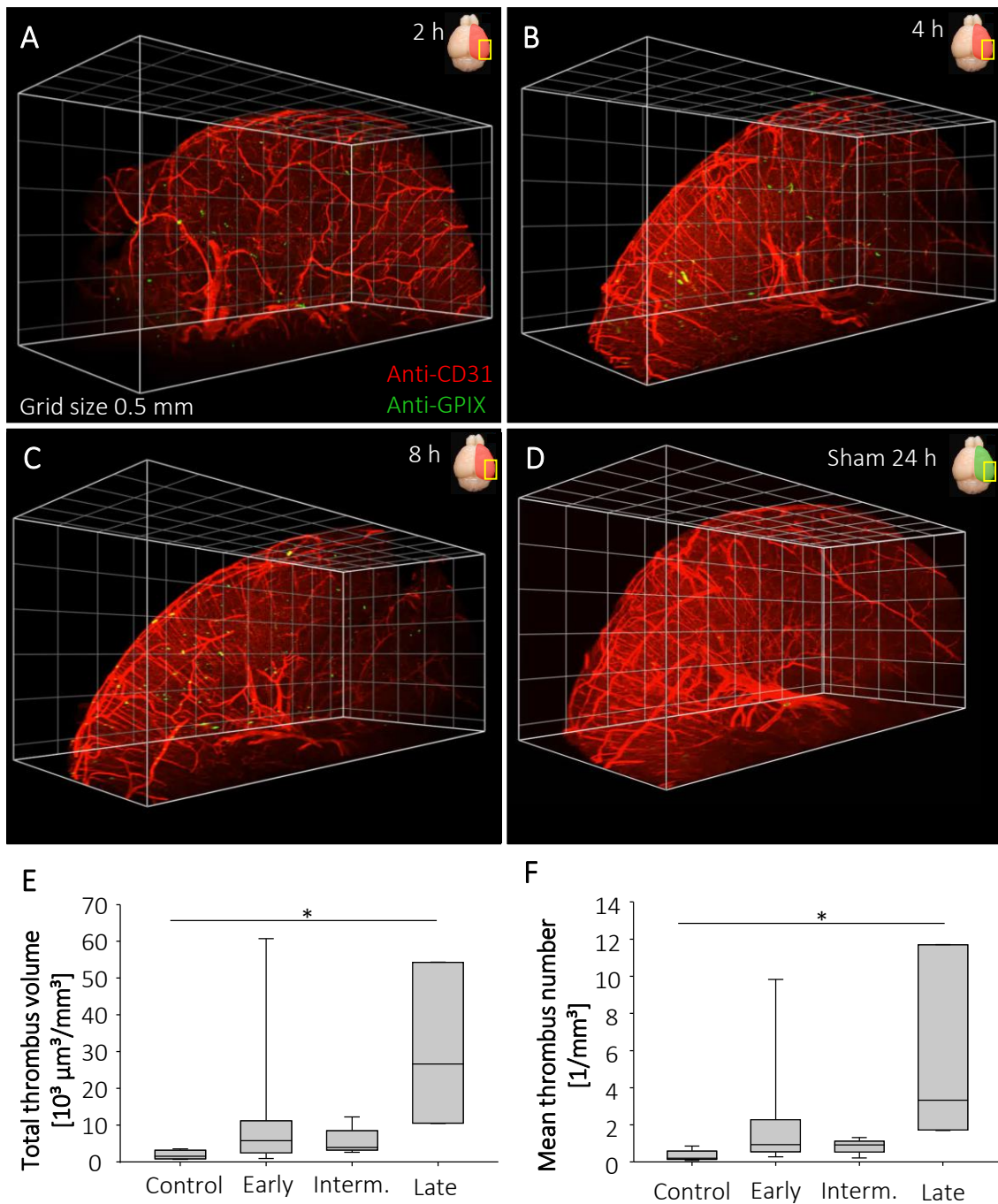


Figure 20. Thrombus formation starts only in the late phase of I/R injury in wild type animals. **A-D** Representative 3D LSFM image of platelets (anti-GPIX Alexa750, green) and brain vasculature (anti-CD31 Alexa647) in wild type mice 2 h (A), 4 h (B) and 8 h (C) after tMCAO show strongly reduced thrombus formation compared to 24 h (Fig 3B), while the number of platelets aggregates is still higher than in control animals (D). **E-F** Total thrombus volume (E) and mean thrombus number (F) for control wild type animals (untreated and sham operated, $n=5$), animals at the early (2-4 h after stroke, $n=7$) and intermediate (8 h after stroke, $n=5$) phases of I/R injury are lower compared to the late (24 h after stroke, $n=3$) stage. The values are normalized by imaged brain volume. Kruskal-Wallis One Way ANOVA on Ranks, $p<0.05$; Multiple comparison procedures (Dunn's Method) $p<0.05$ for control and late groups.

In addition, thrombus formation was quantified in the contralateral hemispheres (CLHs), which do not exhibit tissue death after stroke. Representative 3D reconstruction of ischemic brains 4 h or 24 h after tMCAO clearly showed that small thrombi are formed also in the CLH (Figure 21A-B). Next, the thrombus numbers and total thrombus volumes were compared for ILHs and CLHs by building the CL/IL ratios for both parameters. Thrombus numbers and total volume in CLHs were approximately at 50% of levels in ILHs (Figure 21C-D). These data indicate, that during I/R injury, thrombus formation occurs in both hemispheres to a low extent without leading to tissue damage.

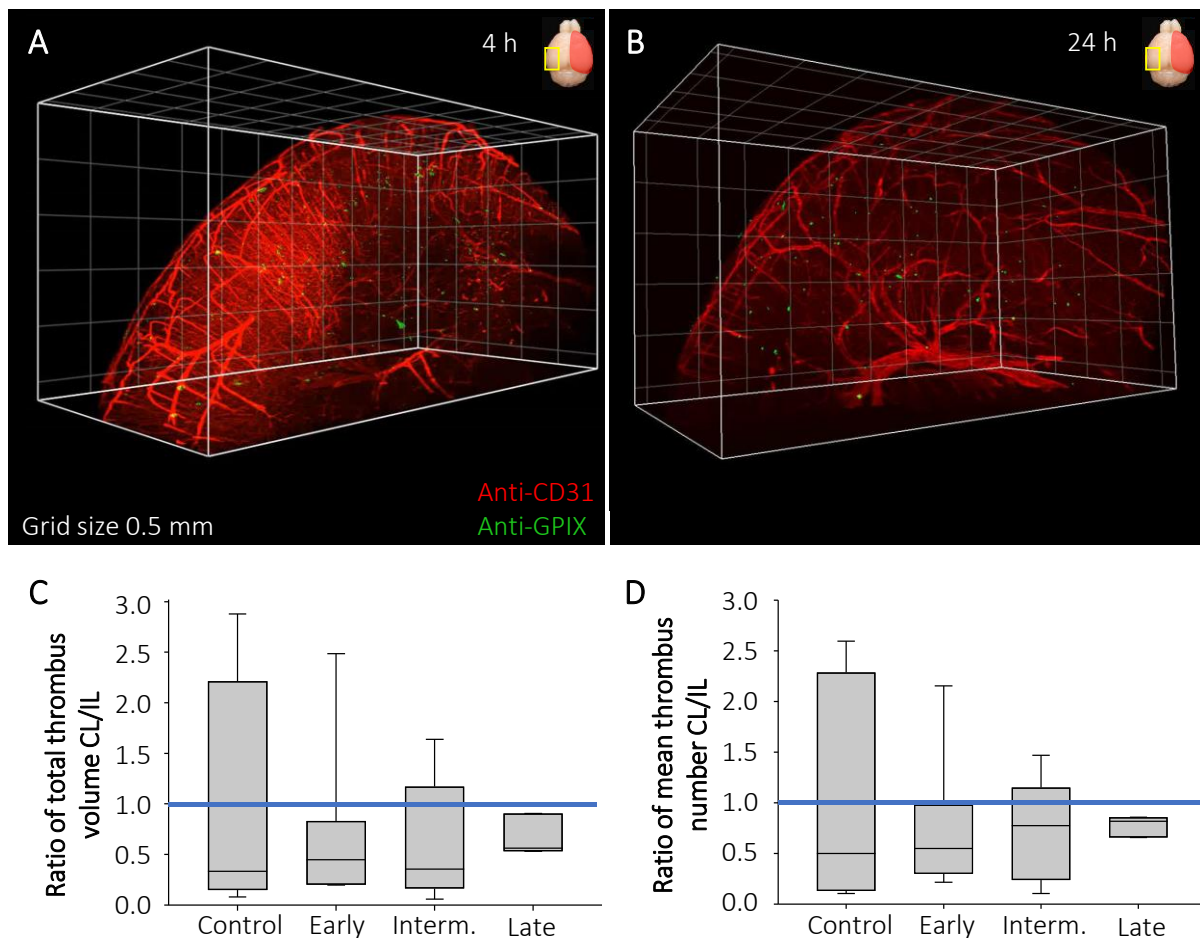


Figure 21. Contralateral hemisphere shows thrombus formation after ischemic stroke in wild type animals. A-B Representative 3D LSFM image of platelet aggregates (anti-GPIX Alexa750, green) and brain vasculature (anti-CD31 Alexa647) in the CLH of mouse brains 4 h (A) and 24 h (B) after tMCAO show thrombus formation to a less extent compared to the ILH (Fig. 3B and 4A-C). C-D Quantitative analysis of the ratios total thrombus volume (E) and mean thrombus number (F) of contralateral (CL) and ipsilateral (IL) hemispheres for control wild type animals (untreated and sham operated, n=5), animals at the early (2-4 h after stroke, n=7), intermediate (8 h after stroke, n=5) and late (24 h after stroke, n=3) stages of I/R injury reveals reduced thrombus formation in the CL side of the ischemic brain. Blue line corresponds to the value of 1. The values are normalized by imaged brain volume.

4.2.2 Investigation of the early phase of I/R injury after ischemic stroke

Brain tissue damage caused by I/R injury reaches its maximum extent already 8 h after recanalization, as demonstrated by Schuhmann *et al.* (personal communication). Tissue damage mainly results from neuronal death which takes approximately 4 h after the point of inception. Thus, the processes causing brain infarction are likely to take place in the first 4 h after successful recanalization. Thus, in further experiments, platelets, the vasculature and neutrophils were investigated during the early phase (1-4 h) of acute I/R injury by LSM and intravital 2PM.

4.2.2.1 Establishment of intravital brain imaging by two-photon microscopy

2PM of the murine brain is limited by the poor accessibility of the organ for light as it is covered by a strongly absorbing skull. To overcome this limitation, in general, two different approaches are used: i) skull thinning and ii) replacement of the skull by a glass coverslip. The latter is also known as open cranial window (OCW) technique and is supposed to allow for deep light penetration depths as well as to give the possibility of long time imaging¹⁴². Skull thinning also enables intravital brain imaging, but is limited in light penetration depth. Further, mice must be imaged latest one day after the surgical procedure due to the rapid regrowth of the skull. As skull thinning almost always induces minor damage of the brain cortex, the processes resulting from the surgery and the ischemic stroke can overlap. Thus, the OCW technique was established and used for intravital imaging of murine brains after ischemic stroke.

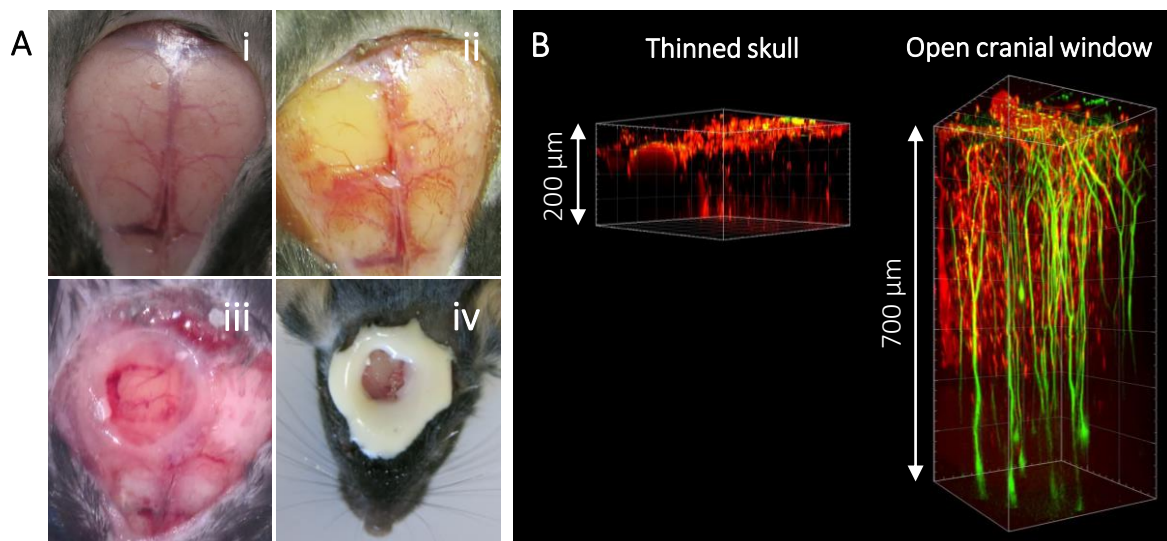


Figure 22. Open cranial window technique enables higher penetration depth compared to thinned skull method for 2PM. **A** The established open cranial window (OCW) method for 2PM consists of four steps: i) removal of the skin around the skull, ii) thinning of square shaped skull area combined with subsequent skull removal, iii) covering of the skull-free area with a small coverslip using cyanoacrylate and iv) sealing the skin-free area with dental cement. **B** Thy1-eGFP mice were subjected to the thinned skull or OCW procedures and subsequently intravital two-photon microscopy of the immunolabeled (vasculature: anti-CD31 Alexa 546, platelets: anti-GPIX Alexa 488) brains was performed. Representative images show a much higher light penetration depth after OCW compared to thinned skull method.

The OCW technique has been described by different groups and the methodology differs slightly. The technique was, for the first time, established in our laboratory in the course of this thesis, while the protocol details were adjusted to the needs of imaging mice after ischemic stroke. The workflow can be subdivided in four main steps. First, the skin was removed around the skull (Figure 22A-i). Subsequently, a small square-shaped part of the skull in the area of the biggest expected infarction was thinned and removed (Figure 22A-ii). Here, the damage of the dura and resulting loss of CFS was prevented. During the establishment of the technique, application of low melting agarose or sodium chloride as immersion medium (of higher refractive index compared to the air) between the coverslip and the dura were tested. While application of low melting agarose frequently resulted in high opaqueness, saline led to sufficiently good results. The dura was covered with a small amount of saline and a glass coverslip, which was sealed using cyanoacrylate (Figure 22A-iii). As a last step of the procedure, the full skin free area on the skull and the margins of the edges of the coverslip were covered with dental cement stabilizing the cranial window and preventing non-sterile inflammation (Figure 22A-iv). Mice were allowed to recover and were closely monitored for two

weeks to guarantee the full remission of surgery induced injury. Comparison of 3D reconstruction of 2PM images of mouse brains showed that the OCW method enables deeper tissue imaging down to 700 μm deep in the cortex while only 200 μm deep structures can be visualized in case of the thinned skull. Further, the image resolution is higher for OCW compared to the thinned skull method allowing for identification of single neurons and platelets. In contrast, the thinned skull method results in poor image resolution (Figure 22B).

4.2.2.2 Intravital imaging of platelet-vessel interaction during the early phase of the I/R injury

The results of thrombus mapping in ischemic brains during the first 24 h after stroke by volumetric imaging using LSFM suggest a minor role of thrombus formation (chapter 4.2.1). Given that platelets strongly influence the outcome of the I/R injury^{93,94,96}, initial investigation of platelet-vessel interaction was performed using intravital 2PM. Therefore, mice with OCW were subjected to tMCAO and directly after reperfusion were intravenously immunolabeled with anti-GPIX and anti-CD105 antibodies. In this initial study, immunolabeling of the vasculature using anti-CD31 antibodies was not performed as platelets also express PECAM1. Multiple vessels were imaged in the brain cortex for a duration of 30 min. To assess platelet-vessel interaction, the 2D time lapse images were maximum intensity projected (MIP). At certain regions of the imaged vessels increased intensity of the labeled anti-GPIX antibody was detected in the MIP images (Figure 23). Signal accumulation appeared mostly at sites of vessel bifurcation and was found to originate from decrease of flow velocity and not from permanent adhesion or aggregate formation of platelets at these regions. Interestingly, the anti-CD105 antibody signal was also enhanced at these sites. These observations indicate that interaction of platelets with the vessel wall correlates with CD105 expression in the ischemic brains. Nevertheless, it is still unclear whether platelets induce endothelial cell responses, which that result in increased CD105 expression, or whether already activated ECs attract platelets.

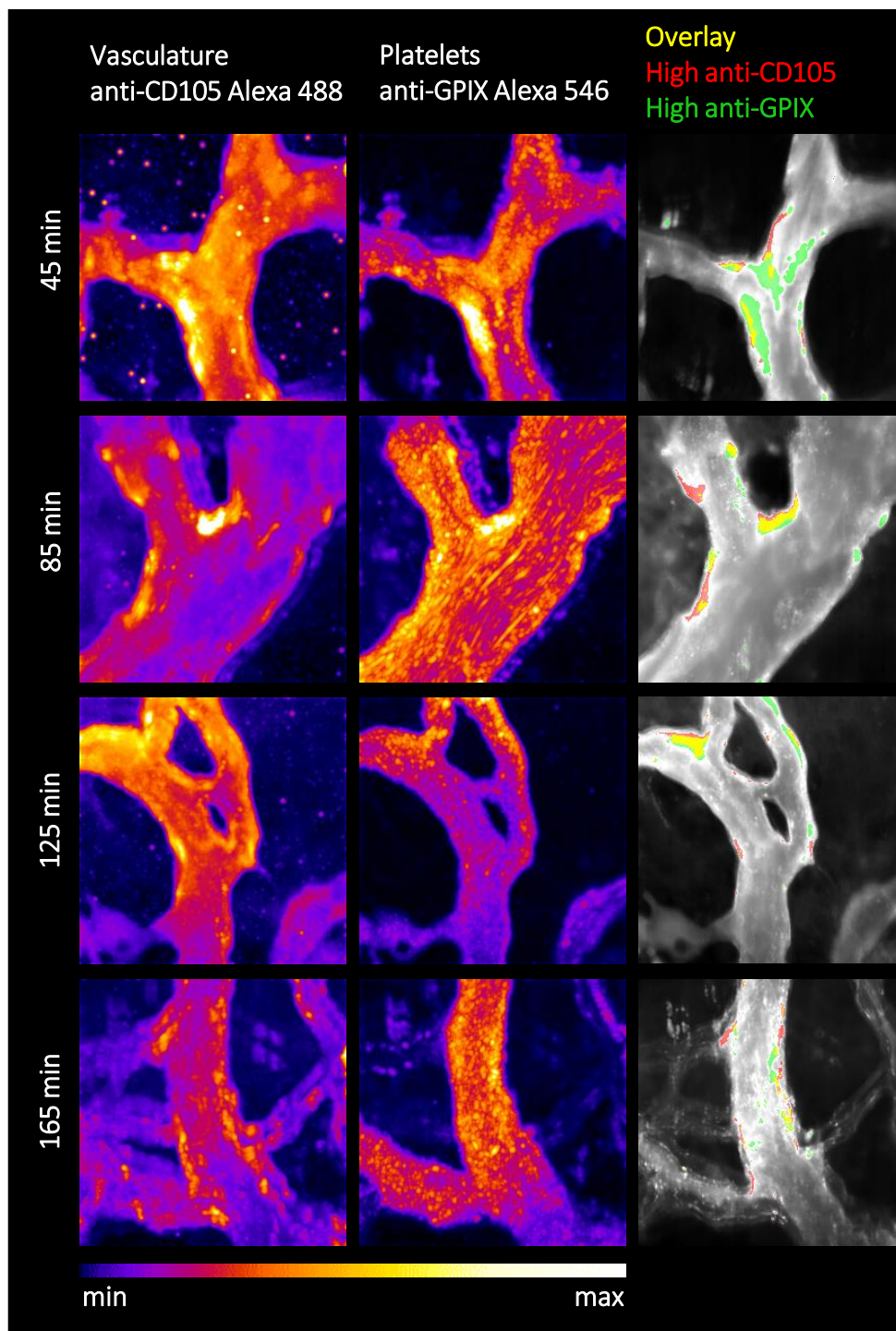


Figure 23. Frequent platelet-vessel interaction correlates with enhanced CD105 expression in wild type murine brains after stroke. Different areas of ischemic murine brain (n=4 mice) were intravitaly imaged using two-photon microscopy during the early phase (0-4 h after tMCAO) of I/R injury. Each area was imaged at a frequency of 30 frames/s and the images were maximum projected over time. Representative single channel and overlay images are shown. Higher intensity in the single channel images (yellow-white) represents the areas of GPIX (platelet) or CD105 accumulation over time. Overlay images show high colocalization (yellow) of anti-CD105 Alexa488 (red) and anti-GPIX Alexa546 (green) accumulation sites signals especially at vessel bifurcations.

4.2.2.3 Investigation of platelet distribution, vascular response and neutrophil infiltration during the early phase of the I/R injury by LSFM

Previous studies have shown that I/R injury after stroke is a thrombo-inflammatory process, where platelets, endothelial and immune cells play a major role. So far, mapping of these major players in large areas of the ischemic brain has not been performed for the early phase of the acute stroke.

Here, 2 mm thick ischemic brain slices harvested 4 h after reperfusion were imaged using high magnification (20x) LSFM. Platelets, the vasculature and neutrophils were stained using anti-GPIX, anti-CD31 and anti-Ly6G antibodies, respectively, and were detected and quantitatively analyzed in IL and CL hemispheres. The 3D data sets were acquired in 3 different regions of each hemisphere. Figure 24 shows a representative 3D LSFM image of the ILH slice of an ischemic brain. The zoom-in image clearly shows single platelets and neutrophils as well as the capillaries. Due to the small thickness of the imaged sample, perfusion fixation was not performed.

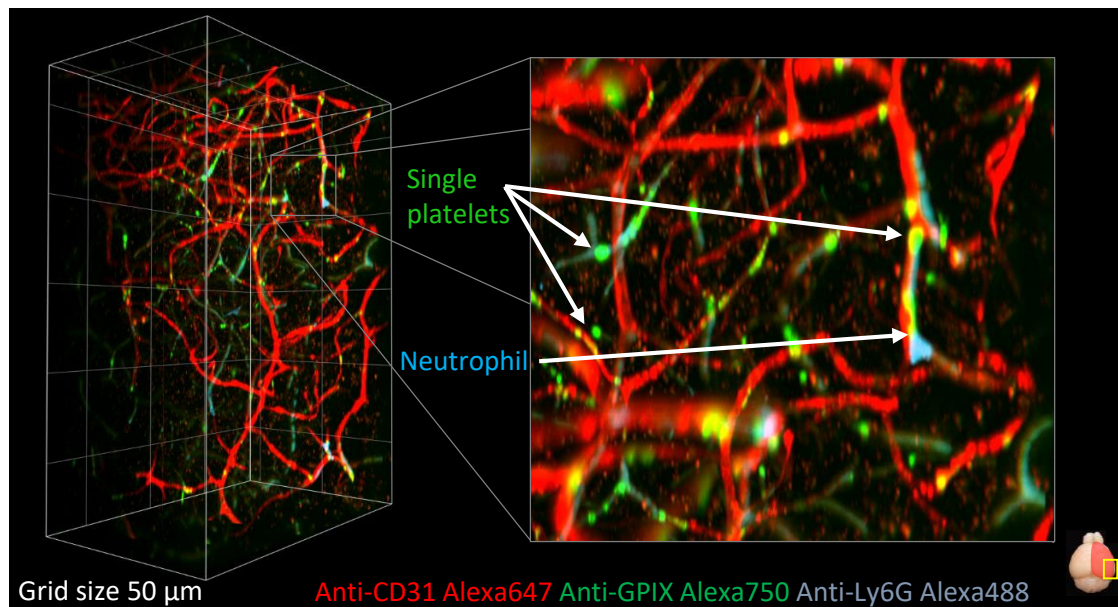


Figure 24. High magnification LSFM enables imaging of platelets, the vasculature and infiltrating neutrophils at subcellular resolution in murine brains 4 h after stroke. Mice were subjected to tMCAO and, subsequent to the reperfusion, intravenously injected with anti-GPIX Alexa750 (green), anti-CD31 Alexa647 (red) and anti-Ly6G Alexa488 (blue) antibodies. The brains were collected without perfusion 4 h after stroke. LSFM of small areas ($512 \times 512 \mu\text{m}^2$) in the CL and IL hemispheres (3 areas each) was performed with a high magnification 20x objective. Representative image of a cropped data set shows the 3D reconstruction of the z-stack. The zoom-in images demonstrate the high resolution image enabling to identify single platelets and neutrophils. Grid size 50 μm .

Platelet tethering and activation has been found to play an important role in the progression of I/R injury. Here, platelet appearance in the ischemic brain was quantitatively assessed in wild type animals and in mice, which were treated with the GPIIb/IIIa blocking Fab-fragment p0p/B. p0p/B-treated mice are strongly protected in tMCAO model exhibiting markedly reduced infarct sizes and good neurological outcome⁹³. To quantitatively analyze the 3D images, MIP of z-stack data sets were generated (Figure 25A) and the total GPIIb/IIIa-positive areas (Figure 25B) as well as platelet aggregate (Figure 25C) areas were calculated.

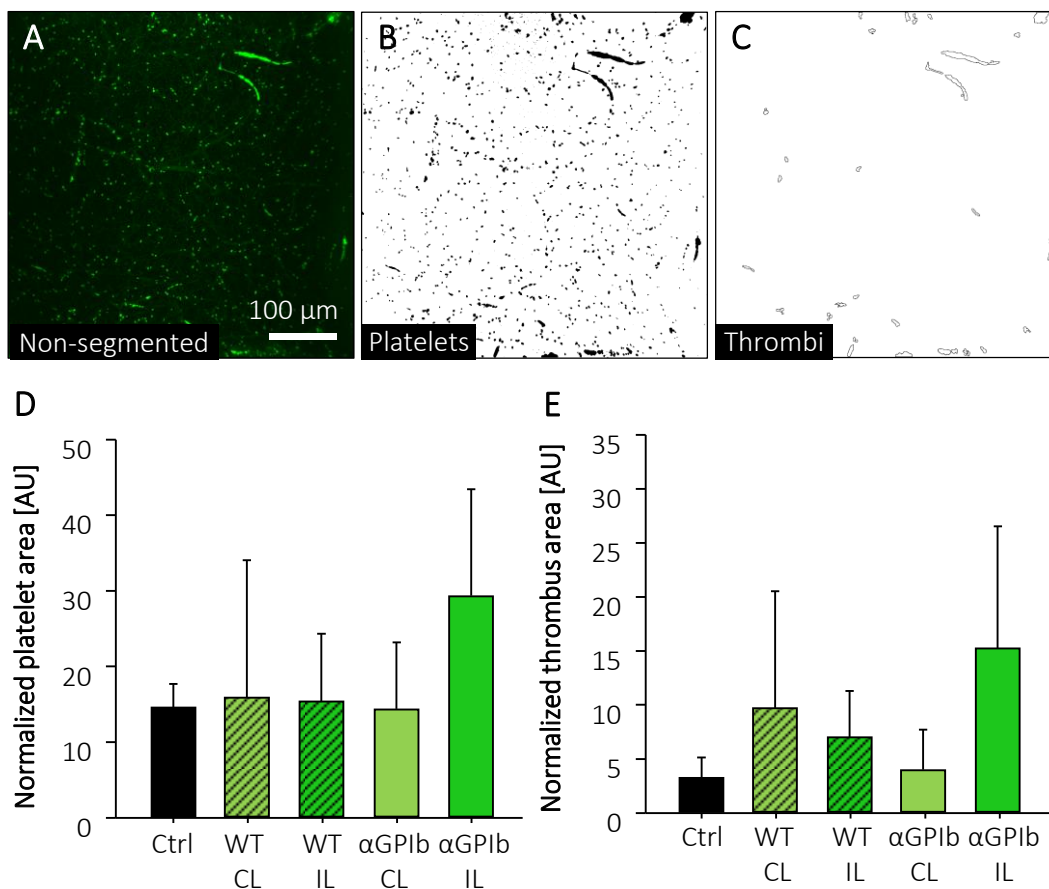


Figure 25. Platelet distribution and aggregate formation in both hemispheres of p0p/B Fab injected and untreated brains 4 h after tMCAO is comparable to control animals. A-C Mice were intravenously injected with anti-GPIIb/IIIa Alexa750, anti-CD31 Alexa647 and anti-Ly6G Alexa488 antibodies 15 min after tMCAO and the brains were collected without perfusion 4 h after stroke. LSFM of small areas in the contralateral (CL) and ipsilateral (IL) hemispheres (3 areas each) was performed with a high magnification 20x objective. 750 nm channel of the resulting 3D stack was maximum projected over Z direction (A) and subsequently the total platelet (B) and total thrombus (C) areas were segmented. D-E The total platelet (C) and total thrombus (D) areas were normalized by the stack size for CL and IL hemispheres of untreated (Ctrl, n=3), wild type (WT, n=4) and wild type GPIIb blocked (αGPIIb, n=4) animals. OneWay ANOVA: $p > 0.05$ for D and E.

Quantitative analysis of the wild type and p0p/B treated animals showed that total amount of platelets is comparable between both groups. Further, no elevated platelet appearance occurs in the ILH compared to the CLH (Figure 25D). Similar results were obtained for platelet aggregate formation (Figure 25E). These results confirm the indirect results from the thrombus mapping experiments and indicate that neither platelet accumulation nor aggregate formation are involved in the progression of I/R injury after stroke.

Endothelial cells are involved in different steps of developing I/R injury. Due to hypoxia they become activated, followed by the rapid impairment of the tight junctions and breakdown of the blood brain barrier (BBB) resulting in increased leakiness of the brain endothelium^{125,188}. CD31 is one of the most frequently used surface markers of ECs and is also involved in inflammatory processes. Here, quantitative analysis of CD31 expression on the ECs of the brain vasculature was performed in the MIP images of the 3D LSFM data sets. Interestingly, a reduction of the anti-CD31 signal was detected in ILH compared to CLH (Figure 26A-B). Quantitative analysis shows that the anti-CD31 signal is reduced in ILH of both wild type and GPIIb/IIIa blocked samples and thus seems to be independent of platelet tethering.

Neutrophil infiltration during I/R injury is controversially discussed in the literature. In addition, these cells have been found to interact with platelets and ECs during inflammatory processes. Thus, the number of neutrophils was determined. Single neutrophils (Figure 26D) were detected and counted in the ILHs and CLHs of wild type and p0p/B Fab treated mice. These results indicate an increase in neutrophil infiltration in the ILHs of both groups compared to the CLHs.

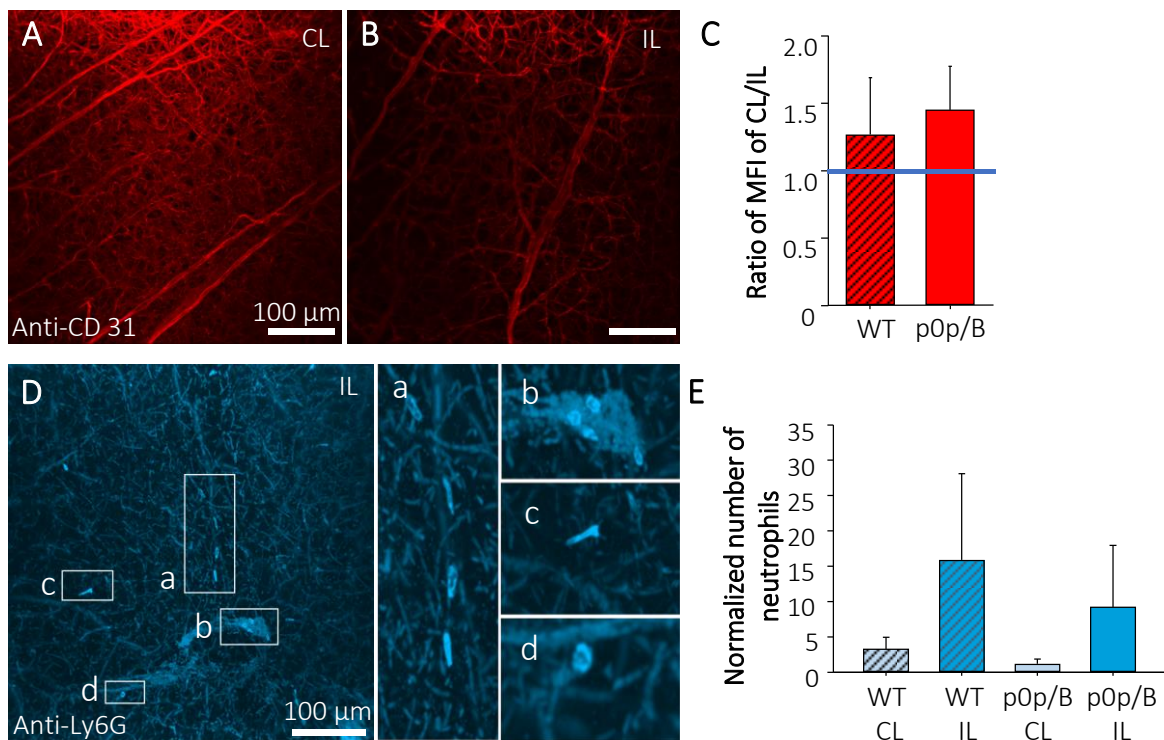


Figure 26. Lowered CD31 expression and enhanced neutrophil infiltration are found in the ILH compared to the CLH 4 h after tMCAO. **A-B** Mice were intravenously injected with anti-GPIX Alexa750, anti-CD31 Alexa647 and anti-Ly6G Alexa488 antibodies 15 min after tMCAO and the brains were collected without perfusion 4 h after stroke. LSM of small areas in the contralateral (CL) (A) and ipsilateral (IL) (B) hemispheres (3 areas each) was performed with a high magnification 20x objective. 647 nm channel of the resulting 3D stack was maximum projected over Z direction and subsequently the mean fluorescence intensity (MFI) was calculated. **C** The MFIs of anti-CD31 Alexa647 and anti-Ly6G Alexa488 signals were normalized by the stack size for CL and IL hemispheres of untreated (Ctrl, n=3), wild type (WT, n=4) and p0p/B-F(ab) treated wild type animals (p0p/B, n=4) and the ratio of the values for CL and IL was calculated. Blue line indicates the value 1. **D** 488 nm channel of the resulting 3D stack was maximum projected over Z direction and subsequently the neutrophils (representative magnified images a-d) were counted. **E** The neutrophil numbers were normalized by the stack size for CL and IL hemispheres of wild type (WT, n=4) and p0p/B-F(ab) treated wild type animals (p0p/B, n=4). OneWay ANOVA: $p > 0.05$.

5 Discussion and outlook

5.1 Megakaryocyte distribution in the bone marrow

Investigation of megakaryocyte (MK) migration in the bone marrow during the maturation should be ideally performed by *in vivo* imaging of the cells in different types of bones for their entire lifespan. However, this ideal approach cannot be realized due to limitations in the imaging techniques. Thus, different methods must be combined to gain new insights in these processes. Here, *in vivo* imaging of MKs in murine skull, *ex vivo* light sheet microscopy (LSFM) of intact cleared bones of different types and *in silico* analysis of MK distribution based on microscopy data were combined for this purpose.

In vivo imaging of MKs by multi-photon microscopy in the bone marrow has been performed by several groups in the past^{24,25,41}. Interestingly, the results indicated a strong spatial vessel association of the cells and a lack of motility. Nevertheless, the short imaging time or pretreatment of the animals with TPO did not allow for a reliable conclusion on the migratory activities of MKs at longer time scales. Here, a long-time (4 h) multi-photon imaging protocol of skull bone marrow was established by finding a stable immunolabeling and using volumetric multi-photon imaging, resulting in increased numbers of investigated MKs. Mean squared displacement analysis of the tracked MKs confirmed the previous results by van Eeuwijk and Junt *et al*^{24,25}. Furthermore, due to a high number of analyzed cells, vessel-associated (VA) and non-VA (NVA) cells could be compared. Here, no differences were found in respect to migratory activities of the two groups at time scales of several hours. Nevertheless, spontaneous MK migration towards the vasculature, especially in bone types other than skull, cannot be fully excluded by these data.

Bigger bones such as femur or sternum are hardly accessible by two-photon microscopy due to poor light penetration. To circumvent these limitations, *in vivo* imaging was combined with LSFM of intact bones of different types. Due to recent developments in tissue clearing methods and volumetric microscopy as well as improved image processing tools for large 3D data stacks, several groups were able to perform microscopic analysis of bone marrow cells. In her dissertation van Eeuwijk was able to establish a bone clearing protocol and for a first time analyze MK distribution in the bone marrow. Nevertheless, several aspects remained still unclear, namely: 1) Dependence of the vessel association of MKs from the high density of bone marrow vasculature 2) Presence of directed migratory behavior of MKs towards the vasculature and 3) differences between the abundance of MKs in the endosteal (bone-

associated, BA) and vascular (non bone-associated, NBA) niches while, here, the niches are defined in the more conservative way. To address the first two questions, an *in silico* study of MK distribution in the bone marrow was established and performed. First, a new algorithm simulating the cell distribution in the bone marrow vasculature was developed and showed that using real 3D image data acquired by LSM is significantly more beneficial for *in silico* studies than artificial data. Similar studies have been performed for 2D image data by other groups e.g. for the investigation of HSC localization in the bone¹³. Microscopy data were used to a lesser extent in previous studies since smaller cells of high sphericity can be more easily replaced by an artificial structure. However, MKs display high inhomogeneity in size and shape and thus require usage of real image data templates for *in silico* studies. After successfully establishing the algorithm, simulated and measured MK distributions in the bone marrow were compared, leading to the conclusion that vessel-association of the MKs is not fully random, which is in line with previous findings in 2D TEM images of the femur¹⁷, although the reason remains unclear. A vessel-biased MK distribution in the bone marrow can ensure sufficient platelet supply of the organism in cases of extensive blood loss. Possible explanation for the bias could be primarily perisinusoidal localization of HSCs and/or directed growth/polarization of MKs towards the vasculature triggered by signaling proteins such as soluble SDF1 or the endothelial cell protein VCAM-1. Very recently, Dütting *et al.* from our department came up with another explanation: we suggested that GTPases downstream of GPIIb α might by a regulatory circuit guiding MK polarization⁴². Decreased MK polarization was associated with lower numbers of vessel-associated MKs, while hyperpolarization led to intravasation. In consequence, polarization or “directed growth” mediated by intracellular signaling (downstream of) GPIIb α could be the mechanism responsible for high levels of vessel-association of MKs. Furthermore, in the recent publication by Stegner *et al.* we propose a model of two MK pools coexisting in the bone marrow where one group is responsible for platelet production and the other is more quiescent although they contain a similar fraction of mature MKs¹⁸². Considering that MKs and MK-biased HSCs do regulate HSC activity, MKs could display a “self-regulatory” behavior by affecting MK-biased HSCs. This model is supported by the finding that NVA MKs seem not to be part of platelet producing population since they do not display migration towards the vasculature. This finding is based on the comparison of simulated and real NVA MK distributions in the bone marrow where both groups were indistinguishable. In conclusion, NVA MKs are randomly distributed since in the case of directed migration towards the vessel the NVA population of the MKs should show a biased distribution.

The main feature of the classical model of megakaryocyte maturation is the migration from the endosteal niche towards the vascular niche^{21,22}. Nevertheless, as previously shown by different studies, the niche model of the bone marrow must have a more functional than structural character, especially when addressing the activity of HSCs^{13,47,182}. The 3D imaging by LSFM of cleared uncut bones of different types confirmed this model, since the entire bone marrow of long bones as well as trabecular bones was vascularized to the same extent. Moreover, no differences in cell size or MK-to-vessel distance could be found for BA and NBA MKs. Combining these results with the findings by van Eeuwijk, we can conclude that MK size and distribution are dictated by the bone marrow vasculature. This finding is in accordance with the current understanding of functional vascular and endosteal niches, which cannot be fully separated.

5.2 Thrombopoiesis in healthy pulmonary tissue

3D light sheet fluorescence microscopy for murine pulmonary tissue was established to enable megakaryocyte imaging in intact lungs at subcellular resolution. MK numbers were compared between the lung and different bone marrow regions obtained by the same microscopy technique. Quantitative analysis of the 3D LSFM image stacks of pulmonary tissue in healthy mice revealed a markedly (260-1100-fold) lower MK density in the lungs compared to bone marrow samples. Further, extrapolating these data allowed to estimate that about 1% of the total MK population resides in the lungs. These findings lead to the conclusion, that lungs cannot be a major site of thrombopoiesis. Considering that 1% or 2% (2PM or LSFM derived data, respectively) of BM MKs are located intrasinusoidally and can be transported to the lungs by the venous blood flow, the data support the hypothesis that pulmonary MKs originate from the bone marrow, confirming the results from previous studies^{27,32}. Due to limitations in experimental approaches for investigation of thrombopoiesis in the bone marrow, for a long time it was not clear whether the bone marrow or the lung is the major site of platelet production⁴⁴. Although thrombopoiesis does take place in the pulmonary capillaries as demonstrated previously⁴³, the markedly higher number of BM MKs compared to pulmonary MKs shows, that lungs' contribution to thrombopoiesis is limited. This finding strongly contradicts different publications providing relatively high (estimated) fractions of pulmonary thrombopoiesis, especially the recent work by Lefrançois *et al*³³. Nevertheless, the limitations of the experiments regarding the low imaging volumes or resolution and misleading

extrapolations leading to overestimated values has to be taken into consideration. Here, LSFM clearly provides an advantage of imaging large volumes at high resolution.

Despite the low number of investigated animals, the quantitative analysis of LSFM data showed highly significant differences between MK densities in the BM as compared to the lungs. Nevertheless, the effect of cardiac perfusion procedure prior investigation of the tissue should be considered, as theoretically intravascular pulmonary MKs can be removed by this technique. However, qualitative examination of LSFM images of non-perfused lungs from the same experiments did not reveal any differences between the two groups (data not shown). Further, the percentage of intrasinusoidal MKs obtained by intravital microscopy was determined to be even lower compared to LSFM data, indicating that perfusion fixation has no or a marginal effect on MK density in LSFM data.

The number of MKs in lungs is known to positively correlate with certain pulmonary, cardiovascular or other diseases^{26,27}. Nevertheless, it is unclear whether MK transmigration process is enhanced under pathological situations or general increase in MK numbers leads to more intravascular, and in a consequence, pulmonary MKs. Investigation of these processes could be performed with large volume LSFM, enabling precise comparison of MK numbers in different organs of the same animal.

5.3 Microscopy and image processing techniques for investigation of ischemic stroke

Studies on the pathomechanisms underlying ischemic stroke have been performed by using various techniques in the last decades. This includes flow cytometric analysis of cell content of ischemic brains as well as protein concentration analysis using quantitative Western blotting or enzyme-linked immunosorbent assays^{135,189,190}. Nevertheless, they do not provide information about the spatial distribution of the cells or proteins in the brains. Cell-cell interactions or protein expression levels on specific cell types are also difficult to assess by non-imaging methods. To overcome these limitations, microscopy techniques are often combined with biochemical methods^{138,139,189}. Here, mainly fluorescence microscopy of thin brain sections is performed. Due to straightforward immunostaining protocols for thin tissue sections compared to intravital or large volume staining and easy accessibility of different regions of the organ, this technique can be used for initial screening of cells and proteins of interest. However, the limitation in imaged volume and influence of cutting artifacts during

sectioning can lead to altered results. Intravital imaging using two-photon microscopy avoids cutting artifacts and provides valuable information about the dynamics of ongoing processes in the living animals. Furthermore, it allows to visualize transient interactions in small image volumes, which are not detectable with *ex vivo* techniques^{191–193}. Nevertheless, only cortical brain regions can be imaged by this technique due to limitations in the penetration depth.

Light sheet fluorescence microscopy (LSFM) is the only imaging technique enabling whole organ microscopy at subcellular resolutions without inducing cutting artifacts or leading to severe photobleaching. LSFM is therefore a unique tool to screen for rare events in the entire organ, which is technically almost impossible with other microscopy methods. Thus, this technique should be used complementary to other microscopy methods in stroke research. However, sample staining, clearing and imaging is non-trivial for LSFM. In consequence, investigation of ischemic brains by LSFM has been so far described only once, where the vascular degradation was studied during the chronic phase of I/R injury after tMCAO¹⁹⁴. Nevertheless, the signal-to-noise ratio and segmentation quality of acquired 3D stacks were not fully optimized in that study. In the present work, a more advanced LSFM imaging method for low- and high-resolution simultaneous mapping of different cell types, such as platelets, the vasculature and neutrophils, by optimizing immunolabelling and clearing parameters for sample preparation was developed. This technique, for the first time, enables to visualize and correlate different structures in various brain regions. Further, a complex image processing workflow was established for thrombus detection in large data sets overcoming the complications resulting from highly inhomogeneous and strong autofluorescence of the brain tissue. For thrombus segmentation, advanced machine learning tools in combination with object detection were used to enable unbiased automated quantitative analysis. The general approach of thrombus detection can be adapted to other cases of big data set segmentation for organs characterized by high autofluorescence.

So far, ischemic stroke is mostly investigated by endpoint analysis using different biochemical and microscopic methods. For investigation of dynamic processes in the ischemic brain over several hours, two-photon intravital microscopy via open cranial window was implemented and adapted from previous publications¹⁴². The established technique enabled dynamic simultaneous imaging of platelets and the vasculature at high spatial and temporal resolutions. Furthermore, in future experiments, multiple imaging sessions with the same animal can be performed to investigate long-term effects of stroke. In an initial experiment (data not shown), brains collected after intravital imaging were subjected to clearing and subsequent LSFM

providing the possibility to combine these two techniques in terms of correlative microscopy in future.

5.4 Thrombus formation during the acute phase of I/R injury after ischemic stroke

The important role of platelets during the acute phase of reperfusion injury after stroke has been demonstrated in numerous studies. Briefly, platelet signaling pathways responsible for tethering and activation, but not aggregation are involved in thrombo-inflammatory processes during ischemic stroke^{113,195}. Nevertheless, it is still broadly believed that thrombus and small platelet aggregate formation lead to the poor outcome of I/R injury¹¹³. In previous studies, it could be clearly demonstrated that the absence or blockade of the platelet integrin GPIIb/IIIa, which mediates aggregate formation by platelet bridging, is not beneficial during stroke neither in experimental nor in clinical settings. Instead, the animals or patients developed severe intracranial hemorrhages with a worsened or even lethal outcome^{93,110}. To clearly identify a potential role of thrombus formation during reperfusion injury, quantitative analysis of thrombus number and volume in ischemic brains must be assessed¹⁹⁵.

So far, investigation of ischemic tissue after during I/R injury is mostly performed at 24 h after the initial tMCAO. Nevertheless, Schuhmann and colleagues (Department of Neurology, University hospital Würzburg, personal communication) investigated the infarct sizes and neurological outcome of tMCAO after the time points of 2 h, 4 h, 8 h, and 24 h, and found that the infarct size is already maximal 8 h after recanalization. These results raise the question, whether thrombus formation correlates with or even causes tissue damage and poor neurologic outcome. So far, quantitative analysis of thrombus formation has been investigated by Western blotting of brain lysates, or fluorescence microscopy of thin tissue sections. Nevertheless, these techniques do not provide spatially resolved information for large brain areas. In this work, thrombus mapping in ischemic brains was performed using LSM in both brain hemispheres for the early (2-4 h), intermediate (8 h) and late phases (24 h) of acute stroke. The results from wild type mice subjected to tMCAO show a lower number and total volume of formed thrombi after 24 h of reperfusion injury compared to thrombi observed in animals treated with Fab fragments of the anti-CLEC-2 antibody INU1. INU1-Fab treatment induces massive, life threatening platelet aggregation in different organs including the brain⁵⁷. These data indicate that the thrombus formation which is detectable during the initial 24 h

following tMCAO cannot be causative for the cerebral damage. Further, the thrombus numbers and total volumes are statistically indistinguishable for the control experiments and the early and the intermediate phases of I/R injury. However, both parameters increase during the late phase to still moderate values (compared to INU1-Fab treated animals). Taking into account that tissue damage peaks already 8 h after reperfusion (Schuhmann, personal communication), i.e. at a time point, when thrombus numbers or total volume are at the level of control animals, it cannot be triggered by thrombus formation in the affected regions. In addition, thrombus formation is also detected in the contralateral hemispheres (approximately 50% of the thrombus number and total volume values detected in the ILH) of ischemic brains, which do not exhibit tissue damage after tMCAO, further supporting the concept that thrombus formation is only an epiphenomenon of ischemic stroke but not a cause of tissue damage and infarction in I/R injury. Quantitative comparison of the appearance of platelets or their small aggregates in ischemic brain slices 4 h after reperfusion reflects the results obtained for thrombus formation. Importantly, blocking the platelet GPIIb/IIIa leads to platelet aggregate deposition comparable to that observed in untreated mice. GPIIb/IIIa blockade with Fab-fragments of p0p/B is strongly protective in terms of tissue damage and neurologic outcome in experimental stroke⁹³. Consequently, these data indicate that the neuroprotection (due to GPIIb/IIIa-inhibition) can occur despite the observation of few platelet aggregates. Taken together, these results demonstrate that the few thrombi observed after tMCAO are not the cause of infarct progression during the reperfusion injury. Hereby, the outcome of the experiments is in line with previous experimental and clinical studies, which showed that inhibition of platelet aggregation is not beneficial in I/R injury, but rather increase lethality due to induction of bleeding complications^{93,111}. Apparently, not thrombus formation but platelet tethering and activation dominate the initiation of I/R injury progression. Consequently, the corresponding proteins, such as GPIIb/IIIa or GPVI (and ITAM signaling proteins downstream of GPVI) should be pharmaceutically addressed in future to provide efficient treatment for I/R injury without leading to intracerebral hemorrhage development. Likewise, future imaging studies aiming to elucidate the role of platelets in the infarct progression following tMCAO should study differences between control and GPVI-deficient or GPIIb/IIIa-blocked animals. These experiments would allow to identify the alterations between treated and untreated mice, which can be directly attributed to platelets.

Interestingly, thrombus numbers and volume during the late phase of acute I/R injury correlates with the neurological outcome. Wild type animals show higher number of thrombi compared to Rag1-deficient mice or mice treated with p0p/B Fab. Mice lacking T cells (*Rag1*^{-/-}) as well as

mice with inhibited GPIIb/IIIa-vWF interactions (p0p/B-treatment, $vWF^{-/-}$) are strongly protected in tMCAO model in terms of tissue infarction and neurological outcome^{93,131}. Nevertheless, the underlying mechanisms of the negative correlation between thrombus formation and tissue protection in tMCAO model at the late phase of I/R injury are unclear. However, it appears plausible that dying tissue releases factors which promote thrombotic activity.

The experiments of this part of the thesis have been performed with low mouse numbers, still providing statistically significant results. However, to validate the quantitative analysis and, especially, to corroborate the unchanged thrombus and platelet aggregate formation during the early and intermediate phases, further experiments must be performed.

5.5 Neutrophils and the endothelium in the acute phase of I/R injury

I/R injury resulting from the ischemic stroke is often described as a thrombo-inflammatory process since platelets and immune cells are involved in its progression¹⁹⁵. Besides platelets, endothelial and immune cells play a major role during infarct progression^{90,117,195}. The combination of different microscopic and -non-imaging techniques has provided the information, which cell types act as key players during the progression of I/R injury. Nevertheless, visualization of large brain samples for detection of involved cells and investigation of their localization has not been performed in the acute phase of ischemic stroke.

In this work, high-resolution LSM of ischemic brains was performed to visualize platelets, the expression of PECAM1 on the endothelium and neutrophil infiltration during the early phase of I/R injury in large brain samples. The fluorescence signal intensity of PECAM1, which is expressed on ECs and on activated platelets, is decreased in the ipsilateral hemisphere compared to the contralateral hemisphere. The decrease is also observed to a comparable extent in mice treated with Fab-fragments of the GPIIb/IIIa blocking antibody p0p/B. CD31 has multiple roles during inflammation, where it, on the one side, promotes leukocyte adhesion and transmigration and, on the other side, becomes cleaved by metalloproteinases during EC apoptosis¹²¹. The cleaved soluble PECAM1 acts as an anti-inflammatory protein and blocks leukocyte extravasation and its levels are elevated after ischemic stroke¹²¹. Although, the reason for the decrease in CD31 fluorescence signal detected by LSM is not clear, one could speculate that it results from the removal of endothelial PECAM1 molecules from the EC surface upon the damage of the vasculature. Increased sPECAM1 levels detected in stroke patients in clinical studies support this hypothesis¹²³. Here, further experiments should be

performed to analyze a potential correlation of CD31 reduction on ECs and the tissue damage, localization of platelets or immune cells using correlative microscopy techniques including intravital 2PM and LSM.

A further EC marker, CD105 (endoglin), was investigated during the early phase of acute stroke by dynamic intravital imaging using two-photon microscopy in an initial study. The fluorescence signal of anti-CD105 positively correlated with the abundance of platelet-vessel interactions. There is little known about the role of endoglin during ischemic stroke, except that the deficiency of CD105 worsens the outcome after permanent MCAO¹²⁴. However, CD105 is thought to act anti-inflammatory and enhanced CD105 expression has been observed during inflammation¹⁹⁶. In consequence, one could speculate that elevated CD105 results from the inflammatory processes taking place during the reperfusion injury, potentially, in platelet mediated manner. Nevertheless, control experiments with sham operated mice were missing during this initial study and thus, the results must be treated with caution.

Neutrophil infiltration into the ischemic brain upon reperfusion has been demonstrated by different studies^{133,138,139}. However, the exact role of these cells in I/R injury is less understood. In the present work, neutrophil infiltration into the ipsilateral hemisphere could be confirmed although the number of detected neutrophils (less than 100 cells per 0.5 mm³ sample volume) is comparably low¹³⁸. Obtained data also show neutrophil appearance in the CLH, but to a less extent than in the ILH. Inhibition of initial platelet tethering did not significantly affect the neutrophil infiltration, however, for a clear result, higher number of mice must be studied.

In summary, CD31 abundance on ECs and neutrophil infiltration change during the early phase of acute ischemic stroke. However, the changes also occur in p0p/B Fab treated animals. The low number of investigated animals does not allow to clearly determine whether blocked platelet tethering affects the infiltration of neutrophils or the decrease in CD31 abundance on ECs, or vice versa, warranting further studies.

5.6 Future perspectives

The present work addresses two major topics of platelet biology – megakaryocyte migration and ischemia reperfusion injury after cerebral stroke – by developing and applying advanced microscopy and image processing tools.

Megakaryocyte migration was investigated by combining intravital 2PM and mean squared displacement (MSD) analysis of cell trajectories, *ex vivo* LSFM of cleared murine bones and *in silico* investigation of MK distribution in the bone marrow leading to the conclusion that MKs do not exhibit directed movement towards the BM vasculature. Although no MK migration was detected by intravital microscopy of murine bone marrow, spontaneous migration of these cells cannot be excluded. Furthermore, only mature MKs were investigated in these experiments, as no specific surface markers are available for earlier developmental stages. To address this, repeated intravital 2PM with a duration of several hours could be combined with a “pulse and chase” approach, where individual HSCs (e.g. using *Cttna1*-GFP reporter mice⁷ or photoactivatable GFP¹⁹⁷ in combination with bone marrow transplantation) are followed until the differentiation into a MK and even platelet release. Quantitative analysis of potential migration of HSCs or MK progenitor cells can be performed using time-resolved mean squared displacement analysis. This technique gives the possibility to identify different migration types, such as directed, diffusive-like and wobbling-like movements, on variable time scales, which typically occur alternately^{198,199}. Furthermore, these experiments could also be used to provide experimental evidence for the results of the *in silico* studies of HSC and neutrophil migration in the bone marrow, where MKs were found to act as steric obstacles. These computational simulations were performed with newly developed algorithms, which use real 3D LSFM data as templates for MKs or the BM vasculature and allow to model random and non-random cell distribution and different types of cell migration including chemotaxis. Due to its flexibility, the algorithms can be used for investigation of cell distribution and migration in any type of tissue, e.g. immune cells in lymph nodes or HSC homing in the BM after irradiation and transplantation, if respective 3D templates are present.

Investigation of acute phase of cerebral ischemic stroke requires the full information on the distribution of cell types of interest, such as platelets or immune cells. Knowledge of cell localization enables to elucidate cell infiltration and cell-cell interactions. Therefore, a LSFM workflow for imaging of whole murine brains was established. Quantitative mapping of formed thrombi or platelet aggregates was required advanced, machine-learning-based image processing techniques, due to the high and inhomogeneous autofluorescence signal of brain

tissue. The image processing workflow can be easily transferred to other cases of object segmentation in big volumetric data. In future, also deep machine learning visual segmentation tools, e.g. software provided by Definiens (Germany) or Zeiss (Germany), could be implemented into the workflow to even increase the segmentation quality and shorten the calculation times.

In the present work, immunolabeling of cells of interest was performed by intravenous injection of fluorescently labelled antibodies. However, the established LSFM workflow can be also combined with *ex vivo* immunostaining methods. This combination allows for imaging of structures/cells which are not accessible by intravenous antibody injection (due to the blood-brain-barrier) but play important roles during the development of I/R injury, such as neurons, microglia or astrocytes. Further, replacing the BBB clearing by methods, e.g. 3DISCO or CUBIC, preserving the functionality of fluorescent proteins can extend the applicability of the workflow to mouse lines expressing fluorophore conjugated proteins.

In initial experiments, high-resolution intravital imaging of platelets and the vasculature in ischemic brains was performed. Despite their small size, single platelets in the brain vasculature were resolved in the time lapse images. The results indicated that CD105 expression on ECs is enhanced at sites of frequent platelet-vessel contact. Since 2PM is strongly limited in the size of imaged volume, a correlative approach combining LSFM and 2PM could be beneficial to explore the dynamics of cell-cell interactions and subsequently map for characteristic interactions *ex vivo*. However, image registration tools have to be adapted for the specific workflow to accurately identify the exact small regions of intravital microscopy in the whole-brain data set acquired by LSFM.

The established workflows and their proposed development provide the possibility of visualization of the ischemic brain on cellular to subcellular levels. Especially the combination of 2PM and LSFM should be used in future to further explore the affected brain regions in respect of cell distribution and localization. T cells, which are strongly involved in pathology of I/R injury^{129,131,132}, are the particularly suitable candidates for such investigations. Confocal microscopy of thin tissue sections or 2PM intravital imaging cannot sufficiently detect the rare events of T cell infiltration, which could be overcome by large volume imaging using LSFM and help to identify potential interaction partners such as platelets or immune cells. Here, differences between Rag1-deficient and wildtype mice should be addressed in terms of platelet and immune cell distribution and the survival of neurons in ischemic brains. Neutrophil infiltration was confirmed in the present LSFM data. However, further investigation of platelet-

neutrophil interactions *in vivo* and colocalization *ex vivo* should be performed using 2PM and LSFM in a correlative approach. So far, the role of neutrophil infiltration in I/R injury is not fully understood and the whole-brain imaging could provide valuable insights by increasing the number of investigated cells and brain regions.

Involvement of ECs in I/R injury was also demonstrated using LSFM, since the ischemic brain areas exhibited a decrease in CD31 signal in the endothelium. However, also the expression of other EC markers, such as VECAM1 or CEACAM 1, is known to be affected during I/R injury. Here, the established LSFM workflow can be used for whole-brain screening of these markers on the endothelium in ipsilateral and contralateral hemispheres. Furthermore, the EC surface proteins mediating tight junctions and thus the integrity of BBB can be addressed with this method.

In conclusion, this thesis has demonstrated that advanced microscopy is a powerful tool to tackle biomedical questions within the platelet field. However, it became clear that sample preparation and microscopy workflows, image processing as well as registration tools need to be optimized/developed in order to fully capitalize on the benefits of advanced imaging.

6 References

1. Crane GM, Jeffery E, Morrison SJ: Adult haematopoietic stem cell niches. *Nature reviews. Immunology* 2017, 17:573–590.
2. Antoniani C, Romano O, Miccio A: Concise Review. Epigenetic Regulation of Hematopoiesis: Biological Insights and Therapeutic Applications. *STEM CELLS Translational Medicine* 2017, 6:2106–2114.
3. Schofield R: The relationship between the spleen colony-forming cell and the haemopoietic stem cell. *Blood cells* 1978, 4:7–25.
4. Kiel MJ, Yilmaz OH, Iwashita T, Yilmaz OH, Terhorst C, Morrison SJ: SLAM family receptors distinguish hematopoietic stem and progenitor cells and reveal endothelial niches for stem cells. *Cell* 2005, 121:1109–1121.
5. Ding L, Saunders TL, Enikolopov G, Morrison SJ: Endothelial and perivascular cells maintain haematopoietic stem cells. *Nature* 2012, 481:457–462.
6. Chen JY, Miyanishi M, Wang SK, Yamazaki S, Sinha R, Kao KS, Seita J, Sahoo D, Nakauchi H, Weissman IL: Hoxb5 marks long-term haematopoietic stem cells and reveals a homogenous perivascular niche. *Nature* 2016, 530:223–227.
7. Acar M, Kocherlakota KS, Murphy MM, Peyer JG, Oguro H, Inra CN, Jaiyeola C, Zhao Z, Luby-Phelps K, Morrison SJ: Deep imaging of bone marrow shows non-dividing stem cells are mainly perisinusoidal. *Nature* 2015, 526:126–130.
8. Lord BI, Testa NG, Hendry JH: The relative spatial distributions of CFUs and CFUc in the normal mouse femur. *Blood* 1975, 46:65–72.
9. Asada N, Takeishi S, Frenette PS: Complexity of bone marrow hematopoietic stem cell niche. *International journal of hematology* 2017, 106:45–54.
10. Morrison SJ, Scadden DT: The bone marrow niche for haematopoietic stem cells. *Nature* 2014, 505:327–334.
11. Boulais PE, Frenette PS: Making sense of hematopoietic stem cell niches. *Blood* 2015, 125:2621–2629.
12. Kunisaki Y, Bruns I, Scheiermann C, Ahmed J, Pinho S, Zhang D, Mizoguchi T, Wei Q, Lucas D, Ito K, Mar JC, Bergman A, Frenette PS: Arteriolar niches maintain haematopoietic stem cell quiescence. *Nature* 2013, 502:637–643.
13. Bruns I, Lucas D, Pinho S, Ahmed J, Lambert MP, Kunisaki Y, Scheiermann C, Schiff L, Poncz M, Bergman A, Frenette PS: Megakaryocytes regulate hematopoietic stem cell quiescence through CXCL4 secretion. *Nature medicine* 2014, 20:1315–1320.
14. Boxio R, Bossenmeyer-Pourié C, Steinckwich N, Dournon C, Nüsse O: Mouse bone marrow contains large numbers of functionally competent neutrophils. *Journal of leukocyte biology* 2004, 75:604–611.

15. Furze RC, Rankin SM: Neutrophil mobilization and clearance in the bone marrow. *Immunology* 2008, 125:281–288.
16. Petit I, Szyper-Kravitz M, Nagler A, Lahav M, Peled A, Habler L, Ponomaryov T, Taichman RS, Arenzana-Seisdedos F, Fujii N, Sandbank J, Zipori D, Lapidot T: G-CSF induces stem cell mobilization by decreasing bone marrow SDF-1 and up-regulating CXCR4. *Nature immunology* 2002, 3:687–694.
17. Lichtman MA, Chamberlain JK, Simon W, Santillo PA: Parasinusoidal location of megakaryocytes in marrow. A determinant of platelet release. *American journal of hematology* 1978, 4:303–312.
18. Pang L, Weiss MJ, Poncz M: Megakaryocyte biology and related disorders. *The Journal of clinical investigation* 2005, 115:3332–3338.
19. Patel SR, Hartwig JH, Italiano JE: The biogenesis of platelets from megakaryocyte proplatelets. *The Journal of clinical investigation* 2005, 115:3348–3354.
20. Yu M, Cantor AB: Megakaryopoiesis and thrombopoiesis. An update on cytokines and lineage surface markers. *Methods in molecular biology (Clifton, N.J.)* 2012, 788:291–303.
21. Avezilla ST, Hattori K, Heissig B, Tejada R, Liao F, Shido K, Jin DK, Dias S, Zhang F, Hartman TE, Hackett NR, Crystal RG, Witte L, Hicklin DJ, Bohlen P, Eaton D, Lyden D, Sauvage F de, Rafii S: Chemokine-mediated interaction of hematopoietic progenitors with the bone marrow vascular niche is required for thrombopoiesis. *Nature medicine* 2004, 10:64–71.
22. Bluteau D, Lordier L, Di Stefano A, Chang Y, Raslova H, Debili N, Vainchenker W: Regulation of megakaryocyte maturation and platelet formation. *Journal of thrombosis and haemostasis : JTH* 2009, 7 Suppl 1:227–234.
23. Niswander LM, Fegan KH, Kingsley PD, McGrath KE, Palis J: SDF-1 dynamically mediates megakaryocyte niche occupancy and thrombopoiesis at steady state and following radiation injury. *Blood* 2014, 124:277–286.
24. Junt T, Schulze H, Chen Z, Massberg S, George T, Krueger A, Wagner DD, Graf T, Italiano JE, Shivdasani Ramesh A., Andrian UH von: Dynamic Visualization of Thrombopoiesis Within Bone Marrow. *Science (New York, N.Y.)* 2007, 317:1764–1767.
25. van Eeuwijk JMM: Studies on thrombopoiesis and spleen tyrosine kinase-mediated signaling in platelets. doctoral thesis. Würzburg, 2016.
26. Brill R, Halpern MM: The frequency of megakaryocytes in autopsy sections. *Blood* 1948:286–291.
27. Sharma GK, Talbot IC: Pulmonary megakaryocytes: "missing link" between cardiovascular and respiratory disease? *Journal of Clinical Pathology* 1986:969–976.
28. Zucker-Franklin D, Philipp CS: Platelet Production in the Pulmonary Capillary Bed. *The American Journal of Pathology* 2000, 157:69–74.
29. Weyrich AS, Zimmerman GA: Platelets in lung biology. *Annual review of physiology* 2013, 75:569–591.

30. Borges I, Sena I, Azevedo P, Andreotti J, Almeida V, Paiva A, Santos G, Guerra D, Prazeres P, Mesquita LL, Silva LSdB, Leonel C, Mintz A, Birbrair A: Lung as a Niche for Hematopoietic Progenitors. *Stem cell reviews* 2017.
31. Aschoff L: Ueber capilläre Embolie von riesenkernhaltigen Zellen. *Archiv f. pathol. Anat.* 1893, 134:11–25.
32. Kaufman R, Airo R, Pollack S, Crosby W, Doberneck R: Origin of Pulmonary Megakaryocytes. *Blood* 1965, 1965:767–775.
33. Lefrançais E, Ortiz-Muñoz G, Caudrillier A, Mallavia B, Liu F, Sayah DM, Thornton EE, Headley MB, David T, Coughlin SR, Krummel MF, Leavitt AD, Passegué E, Looney MR: The lung is a site of platelet biogenesis and a reservoir for haematopoietic progenitors. *Nature* 2017, 544:105–109.
34. Wright JH: The Origin and Nature of the Blood Plates. *The Boston Medical and Surgical Journal*, 1906:643–645.
35. Machlus KR, Italiano JE: The incredible journey: From megakaryocyte development to platelet formation. *The Journal of cell biology* 2013, 201:785–796.
36. Becker RP, De Bruyen, Peter P. H.: The transmural passage of blood cells into myeloid sinusoids and the entry of platelets into the sinusoidal circulation; a scanning electron microscopic investigation. *American Journal of Anatomy* 1975:183–206.
37. Radley JM, Scurfield G: The mechanism of platelet release. *Blood* 1980, 56:996–999.
38. Hartwig JH, Italiano JE: The birth of the platelet. *Journal of Thrombosis and Haemostasis* 2003:1580–1586.
39. Italiano JE, Shivdasani Ramesh A.: Megakaryocytes and beyond: the birth of platelets. *Journal of Thrombosis and Haemostasis* 2003:1174–1182.
40. Nishimura S, Nagasaki M, Kunishima S, Sawaguchi A, Sakata A, Sakaguchi H, Ohmori T, Manabe I, Italiano JE, Ryu T, Takayama N, Komuro I, Kadowaki T, Eto K, Nagai R: IL-1 α induces thrombopoiesis through megakaryocyte rupture in response to acute platelet needs. *The Journal of cell biology* 2015, 209:453–466.
41. Zhang L, Orban M, Lorenz M, Barocke V, Braun D, Urtz N, Schulz C, Brühl M-L von, Tirniceriu A, Gaertner F, Proia RL, Graf T, Bolz S-S, Montanez E, Prinz M, Müller A, Baumgarten L von, Billich A, Sixt M, Fässler R, Andrian UH von, Junt T, Massberg S: A novel role of sphingosine 1-phosphate receptor S1pr1 in mouse thrombopoiesis. *The Journal of experimental medicine* 2012, 209:2165–2181.
42. Dütting S, Gaits-Iacovoni F, Stegner D, Popp M, Antkowiak A, van Eeuwijk JMM, Nurden P, Stritt S, Heib T, Aurbach K, Angay O, Cherpokova D, Heinz N, Baig AA, Gorelashvili MG, Gerner F, Heinze KG, Ware J, Krohne G, Ruggeri ZM, Nurden AT, Schulze H, Modlich U, Pleines I, Brakebusch C, Nieswandt B: A Cdc42/RhoA regulatory circuit downstream of glycoprotein Ib guides transendothelial platelet biogenesis. *Nature communications* 2017, 8:1.

43. Howell WH, Donahue D. D.: The production of blood platelets in the lungs. *Journal of Experimental Medicine* 1936:177-203.
44. Kaufman RM, Airo R, Pollack S, Crosby WH: Circulating Megakaryocytes and Platelet Release in the Lung. *Blood* 1965:720–731.
45. Fuentes R, Wang Y, Hirsch J, Wang C, Rauova L, Worthen GS, Kowalska MA, Poncz M: Infusion of mature megakaryocytes into mice yields functional platelets. *The Journal of clinical investigation* 2010, 120:3917–3922.
46. Johnston I, Hayes V, Poncz M: Threading an elephant through the eye of a needle. Where are platelets made? *Cell research* 2017, 27:1079–1080.
47. Zhao M, Perry JM, Marshall H, Venkatraman A, Qian P, He XC, Ahamed J, Li L: Megakaryocytes maintain homeostatic quiescence and promote post-injury regeneration of hematopoietic stem cells. *Nature medicine* 2014, 20:1321–1326.
48. Stegner D, Nieswandt B: Platelet receptor signaling in thrombus formation. *Journal of molecular medicine (Berlin, Germany)* 2011, 89:109–121.
49. Varga-Szabo D, Pleines I, Nieswandt B: Cell adhesion mechanisms in platelets. *Arteriosclerosis, Thrombosis, and Vascular Biology* 2008, 28:403–412.
50. Hagedorn I, Vögtle T, Nieswandt B: Arterial thrombus formation. *Hamostaseologie* 2017, 30:127–135.
51. Ruggeri ZM, Orje JN, Habermann R, Federici AB, Reininger AJ: Activation-independent platelet adhesion and aggregation under elevated shear stress. *Blood* 2006, 108:1903–1910.
52. Maxwell MJ, Westein E, Nesbitt WS, Giuliano S, Dopheide SM, Jackson SP: Identification of a 2-stage platelet aggregation process mediating shear-dependent thrombus formation. *Blood* 2007, 109:566–576.
53. Nesbitt WS, Westein E, Tovar-Lopez FJ, Tolouei E, Mitchell A, Fu J, Carberry J, Fouras A, Jackson SP: A shear gradient-dependent platelet aggregation mechanism drives thrombus formation. *Nature medicine* 2009, 15:665–673.
54. Savage B, Almus-Jacobs F, Ruggeri ZM: Specific synergy of multiple substrate-receptor interactions in platelet thrombus formation under flow. *Cell* 1998, 94:657–666.
55. Nieswandt B, Brakebusch C, Bergmeier W, Schulte V, Bouvard D, Mokhtari-Nejad R, Lindhout T, Heemskerk JW, Zirngibl H, Fässler R: Glycoprotein VI but not alpha2beta1 integrin is essential for platelet interaction with collagen. *The EMBO journal* 2001, 20:2120–2130.
56. Nieswandt B, Watson SP: Platelet-collagen interaction. Is GPVI the central receptor? *Blood* 2003, 102:449–461.
57. Lorenz V: Cellular regulation of the hemITAM-coupled platelet receptor C-type lectin-like receptor 2 (CLEC-2): In vitro and in vivo studies in mice. Doctoral thesis. Würzburg, 2015.

58. Offermanns S: Activation of platelet function through G protein-coupled receptors. *Circulation research* 2006, 99:1293–1304.
59. Clemetson KJ: Platelet activation. Signal transduction via membrane receptors. *Thrombosis and haemostasis* 1995, 74:111–116.
60. Jung SM, Moroi M: Platelets interact with soluble and insoluble collagens through characteristically different reactions. *The Journal of biological chemistry* 1998, 273:14827–14837.
61. Ruggeri ZM: Platelets in atherothrombosis. *Nature medicine* 2002, 8:1227–1234.
62. Sachs UJH, Nieswandt B: In vivo thrombus formation in murine models. *Circulation research* 2007, 100:979–991.
63. Nieswandt B, Schulte V, Bergmeier W, Mokhtari-Nejad R, Rackebrandt K, Cazenave J-P, Ohlmann P, Gachet C, Zirngibl H: Long-Term Antithrombotic Protection by in Vivo Depletion of Platelet Glycoprotein VI in Mice. *J Exp Med* 2001, 193:459–470.
64. Bender M, May F, Lorenz V, Thielmann I, Hagedorn I, Finney BA, Vögtle T, Remer K, Braun A, Bösl M, Watson SP, Nieswandt B: Combined in vivo depletion of glycoprotein VI and C-type lectin-like receptor 2 severely compromises hemostasis and abrogates arterial thrombosis in mice. *Arteriosclerosis, Thrombosis, and Vascular Biology* 2013, 33:926–934.
65. Lowe KL, Finney BA, Deppermann C, Hägerling R, Gazit SL, Frampton J, Buckley C, Camerer E, Nieswandt B, Kiefer F, Watson SP: Podoplanin and CLEC-2 drive cerebrovascular patterning and integrity during development. *Blood* 2015, 125:3769–3777.
66. Finney BA, Schweighoffer E, Navarro-Núñez L, Bénézech C, Barone F, Hughes CE, Langan SA, Lowe KL, Pollitt AY, Mourao-Sa D, Sheardown S, Nash GB, Smithers N, Reis e Sousa C, Tybulewicz VLJ, Watson SP: CLEC-2 and Syk in the megakaryocytic/platelet lineage are essential for development. *Blood* 2012, 119:1747–1756.
67. Stegner D, Dütting S, Nieswandt B: Mechanistic explanation for platelet contribution to cancer metastasis. *Thrombosis Research* 2014, 133:S149-S157.
68. Manne BK, Xiang SC, Rondina MT: Platelet secretion in inflammatory and infectious diseases. *Platelets* 2017, 28:155–164.
69. Deppermann C: Platelets and vascular integrity. *Platelets* 2018:1–7.
70. Ho-Tin-Noé B, Boulaftali Y, Camerer E: Platelets and vascular integrity: how platelets prevent bleeding in inflammation // Platelets and vascular integrity. How platelets prevent bleeding in inflammation. *Blood* 2018, 131:277–288.
71. Middleton E, Rondina MT: Platelets in infectious disease. *Hematology. American Society of Hematology. Education Program* 2016:256–261.
72. Pitchford S, Pan D, Welch HCE: Platelets in neutrophil recruitment to sites of inflammation. *Current opinion in hematology* 2017, 24:23–31.

73. Sreeramkumar V, Adrover JM, Ballesteros I, Cuartero MI, Rossaint J, Bilbao I, Nácher M, Pitaval C, Radovanovic I, Fukui Y, McEver RP, Filippi M-D, Lizasoain I, Ruiz-Cabello J, Zarbock A, Moro MA, Hidalgo A: Neutrophils scan for activated platelets to initiate inflammation. *Science (New York, N.Y.)* 2014, 346:1234–1238.
74. Zuchtriegel G, Uhl B, Pühr-Westerheide D, Pörnbacher M, Lauber K, Krombach F, Reichel CA: Platelets Guide Leukocytes to Their Sites of Extravasation. *PLoS biology* 2016, 14:e1002459.
75. Giles JA, Greenhalgh AD, Denes A, Nieswandt B, Coutts G, McColl BW, Allan SM: Neutrophil infiltration to the brain is platelet-dependent, and is reversed by blockade of platelet GPIIb/IIIa. *Immunology* 2018.
76. Corken A, Russell S, Dent J, Post SR, Ware J: Platelet glycoprotein Ib-IX as a regulator of systemic inflammation. *Arteriosclerosis, Thrombosis, and Vascular Biology* 2014, 34:996–1001.
77. Rondina MT, Garraud O: Emerging evidence for platelets as immune and inflammatory effector cells. *Frontiers in immunology* 2014, 5:653.
78. Nowinski WL: Introduction to Brain Anatomy. Edited by Miller K. New York, NY, Springer New York, 2011, pp. 5–40.
79. Blinder P, Tsai PS, Kaufhold JP, Knutsen PM, Suhl H, Kleinfeld D: The cortical angiome. An interconnected vascular network with noncolumnar patterns of blood flow. *Nature neuroscience* 2013, 16:889–897.
80. Obermeier B, Daneman R, Ransohoff RM: Development, maintenance and disruption of the blood-brain barrier. *Nature medicine* 2013, 19:1584–1596.
81. Famakin BM: The Immune Response to Acute Focal Cerebral Ischemia and Associated Post-stroke Immunodepression. A Focused Review. *Aging and disease* 2014, 5:307–326.
82. Catanese L, Tarsia J, Fisher M: Acute Ischemic Stroke Therapy Overview. *Circulation research* 2017, 120:541–558.
83. Jackman K, Iadecola C: Neurovascular regulation in the ischemic brain. *Antioxidants & redox signaling* 2015:149–160.
84. Bai J, Lyden PD: Revisiting cerebral postischemic reperfusion injury. New insights in understanding reperfusion failure, hemorrhage, and edema. *International journal of stroke : official journal of the International Stroke Society* 2015, 10:143–152.
85. Berkhemer OA, Fransen PSS, Beumer D, van den Berg LA, Lingsma HF, Yoo AJ, Schonewille WJ, Vos JA, Nederkoorn PJ, Wermer MJH, van Walderveen MAA, Staals J, Hofmeijer J, van Oostayen JA, Lycklama à Nijeholt GJ, Boiten J, Brouwer PA, Emmer BJ, Bruijn SF de, van Dijk LC, Kappelle LJ, Lo RH, van Dijk EJ, Vries J de, Kort PLM de, van Rooij WJJ, van den Berg JSP, van Hasselt BAAM, Aerden LAM, Dallinga RJ, Visser MC, Bot JCJ, Vroomen PC, Eshghi O, Schreuder THCM, Heijboer RJJ, Keizer K, Tielbeek AV, den Hertog HM, Gerrits DG, van den Berg-Vos RM, Karas GB, Steyerberg EW, Flach HZ, Marquering HA, Sprengers MES, Jenniskens SFM, Beenen LFM, van den Berg R, Koudstaal PJ, van Zwam WH, Roos YBWEM, van der Lugt A, van Oostenbrugge RJ,

- Majoie CBLM, Dippel DWJ: A randomized trial of intraarterial treatment for acute ischemic stroke. *The New England journal of medicine* 2015, 372:11–20.
86. Hallenbeck JM, Dutka AJ: Background review and current concepts of reperfusion injury. *Archives of neurology* 1990, 47:1245–1254.
 87. del Zoppo GJ, Mabuchi T: Cerebral microvessel responses to focal ischemia. *Journal of cerebral blood flow and metabolism : official journal of the International Society of Cerebral Blood Flow and Metabolism* 2003, 23:879–894.
 88. Badimon L, Vilahur G: Platelets, arterial thrombosis and cerebral ischemia. *Cerebrovascular diseases (Basel, Switzerland)* 2007, 24 Suppl 1:30–39.
 89. Durukan A, Tatlisumak T: Acute ischemic stroke. Overview of major experimental rodent models, pathophysiology, and therapy of focal cerebral ischemia. *Pharmacology, biochemistry, and behavior* 2007, 87:179–197.
 90. Jin R, Yang G, Li G: Inflammatory mechanisms in ischemic stroke. Role of inflammatory cells. *Journal of leukocyte biology* 2010, 87:779–789.
 91. Fluri F, Schuhmann MK, Kleinschnitz C: Animal models of ischemic stroke and their application in clinical research. *Drug design, development and therapy* 2015, 9:3445–3454.
 92. Bhatt DL, Fox KAA, Hacke W, Berger PB, Black HR, Boden WE, Cacoub P, Cohen EA, Creager MA, Easton JD, Flather MD, Haffner SM, Hamm CW, Hankey GJ, Johnston SC, Mak K-H, Mas J-L, Montalescot G, Pearson TA, Steg PG, Steinhubl SR, Weber MA, Brennan DM, Fabry-Ribaud L, Booth J, Topol EJ: Clopidogrel and aspirin versus aspirin alone for the prevention of atherothrombotic events. *The New England journal of medicine* 2006, 354:1706–1717.
 93. Kleinschnitz C, Pozgajova M, Pham M, Bendszus M, Nieswandt B, Stoll G: Targeting platelets in acute experimental stroke. Impact of glycoprotein Ib, VI, and IIb/IIIa blockade on infarct size, functional outcome, and intracranial bleeding. *Circulation* 2007, 115:2323–2330.
 94. Morowski M, Vögtle T, Kraft P, Kleinschnitz C, Stoll G, Nieswandt B: Only severe thrombocytopenia results in bleeding and defective thrombus formation in mice. *Blood* 2013, 121:4938–4947.
 95. Schuhmann MK, Guthmann J, Stoll G, Nieswandt B, Kraft P, Kleinschnitz C: Blocking of platelet glycoprotein receptor Ib reduces "thrombo-inflammation" in mice with acute ischemic stroke. *Journal of neuroinflammation* 2017, 14:18.
 96. Meyer SF de, Stoll G, Wagner DD, Kleinschnitz C: von Willebrand factor. An emerging target in stroke therapy. *Stroke* 2012, 43:599–606.
 97. Verhenne S, Denorme F, Libbrecht S, Vandenbulcke A, Pareyn I, Deckmyn H, Lambrecht A, Nieswandt B, Kleinschnitz C, Vanhoorelbeke K, Meyer SF de: Platelet-derived VWF is not essential for normal thrombosis and hemostasis but fosters ischemic stroke injury in mice. *Blood* 2015, 126:1715–1722.

98. Meyer SF de, Schwarz T, Deckmyn H, Denis CV, Nieswandt B, Stoll G, Vanhoorelbeke K, Kleinschnitz C: Binding of von Willebrand factor to collagen and glycoprotein Ibalpha, but not to glycoprotein IIb/IIIa, contributes to ischemic stroke in mice--brief report. *Arteriosclerosis, Thrombosis, and Vascular Biology* 2010, 30:1949–1951.
99. Denorme F, Meyer SF de: The VWF-GPIb axis in ischaemic stroke. Lessons from animal models. *Thrombosis and haemostasis* 2016, 116:597–604.
100. Stegner D, Haining EJ, Nieswandt B: Targeting glycoprotein VI and the immunoreceptor tyrosine-based activation motif signaling pathway. *Arteriosclerosis, Thrombosis, and Vascular Biology* 2014, 34:1615–1620.
101. van Eeuwijk JMM, Stegner D, Lamb DJ, Kraft P, Beck S, Thielmann I, Kiefer F, Walzog B, Stoll G, Nieswandt B: The Novel Oral Syk Inhibitor, BI1002494, Protects Mice From Arterial Thrombosis and Thromboinflammatory Brain Infarction. *Arteriosclerosis, Thrombosis, and Vascular Biology* 2016, 36:1247–1253.
102. Cherpokova D, Bender M, Morowski M, Kraft P, Schuhmann MK, Akbar SM, Sultan CS, Hughes CE, Kleinschnitz C, Stoll G, Dragone LL, Watson SP, Tomlinson MG, Nieswandt B: SLAP/SLAP2 prevent excessive platelet (hem)ITAM signaling in thrombosis and ischemic stroke in mice. *Blood* 2015, 125:185–194.
103. Deppermann C, Cherpokova D, Nurden P, Schulz J-N, Thielmann I, Kraft P, Vögtle T, Kleinschnitz C, Dütting S, Krohne G, Eming SA, Nurden AT, Eckes B, Stoll G, Stegner D, Nieswandt B: Gray platelet syndrome and defective thrombo-inflammation in Nbeal2-deficient mice. *The Journal of clinical investigation* 2013.
104. Stegner D, Deppermann C, Kraft P, Morowski M, Kleinschnitz C, Stoll G, Nieswandt B: Munc13-4-mediated secretion is essential for infarct progression but not intracranial hemostasis in acute stroke. *Journal of thrombosis and haemostasis : JTH* 2013, 11:1430–1433.
105. Thornton P, McColl BW, Greenhalgh A, Denes A, Allan SM, Rothwell NJ: Platelet interleukin-1alpha drives cerebrovascular inflammation. *Blood* 2010, 115:3632–3639.
106. Choudhri TF, Hoh BL, Zerwes HG, Prestigiacomo CJ, Kim SC, Connolly ES, Kottirsch G, Pinsky DJ: Reduced microvascular thrombosis and improved outcome in acute murine stroke by inhibiting GP IIb/IIIa receptor-mediated platelet aggregation. *J. Clin. Invest.* 1998, 102:1301–1310.
107. Abumiya T, Fitridge R, Mazur C, Copeland BR, Koziol JA, Tschopp JF, Pierschbacher MD, del Zoppo GJ: Integrin alpha(IIb)beta(3) inhibitor preserves microvascular patency in experimental acute focal cerebral ischemia. *Stroke* 2000, 31:1402-09; discussion 1409-10.
108. Bergmeier W, Schulte V, Brockhoff G, Bier U, Zirngibl H, Nieswandt B: Flow cytometric detection of activated mouse integrin alphaIIb beta3 with a novel monoclonal antibody. *Cytometry* 2002, 48:80–86.
109. Massberg S, Schürzinger K, Lorenz M, Konrad I, Schulz C, Plesnila N, Kennerknecht E, Rudelius M, Sauer S, Braun S, Kremmer E, Emambokus NR, Frampton J, Gawaz M:

- Platelet adhesion via glycoprotein IIb integrin is critical for atheroprogession and focal cerebral ischemia. An in vivo study in mice lacking glycoprotein IIb. *Circulation* 2005, 112:1180–1188.
110. Adams HP, Effron MB, Torner J, Dávalos A, Frayne J, Teal P, Leclerc J, Oemar B, Padgett L, Barnathan ES, Hacke W: Emergency administration of abciximab for treatment of patients with acute ischemic stroke. Results of an international phase III trial: Abciximab in Emergency Treatment of Stroke Trial (AbESTT-II). *Stroke* 2008, 39:87–99.
 111. Kellert L, Hametner C, Rohde S, Bendszus M, Hacke W, Ringleb P, Stampfl S: Endovascular stroke therapy. Tirofiban is associated with risk of fatal intracerebral hemorrhage and poor outcome. *Stroke* 2013, 44:1453–1455.
 112. Hagedorn I, Schmidbauer S, Pleines I, Kleinschnitz C, Kronthaler U, Stoll G, Dickneite G, Nieswandt B: Factor XIIa inhibitor recombinant human albumin Infestin-4 abolishes occlusive arterial thrombus formation without affecting bleeding. *Circulation* 2010, 121:1510–1517.
 113. Meyer SF de, Denorme F, Langhauser F, Geuss E, Fluri F, Kleinschnitz C: Thromboinflammation in Stroke Brain Damage. *Stroke* 2016, 47:1165–1172.
 114. Albert-Weißenberger C, Sirén A-L, Kleinschnitz C: Ischemic stroke and traumatic brain injury. The role of the kallikrein-kinin system. *Progress in neurobiology* 2013, 101-102:65–82.
 115. Vidale S, Consoli A, Arnaboldi M, Consoli D: Postischemic Inflammation in Acute Stroke. *Journal of clinical neurology (Seoul, Korea)* 2017, 13:1–9.
 116. Benakis C, Garcia-Bonilla L, Iadecola C, Anrather J: The role of microglia and myeloid immune cells in acute cerebral ischemia. *Frontiers in cellular neuroscience* 2014, 8:461.
 117. An C, Shi Y, Li P, Hu X, Gan Y, Stetler RA, Leak RK, Gao Y, Sun B-L, Zheng P, Chen J: Molecular dialogs between the ischemic brain and the peripheral immune system. Dualistic roles in injury and repair. *Progress in neurobiology* 2014, 115:6–24.
 118. Szalay G, Martinecz B, Lénárt N, Környei Z, Orsolits B, Judák L, Császár E, Fekete R, West BL, Katona G, Rózsa B, Dénes Á: Microglia protect against brain injury and their selective elimination dysregulates neuronal network activity after stroke. *Nature communications* 2016, 7:11499.
 119. Ludewig P, Sedlacik J, Gelderblom M, Bernreuther C, Korkusuz Y, Wagener C, Gerloff C, Fiehler J, Magnus T, Horst AK: Carcinoembryonic antigen-related cell adhesion molecule 1 inhibits MMP-9-mediated blood-brain-barrier breakdown in a mouse model for ischemic stroke. *Circulation research* 2013, 113:1013–1022.
 120. Boeckh-Behrens T, Kleine J, Kaesmacher J, Zimmer C, Schirmer L, Simon S, Poppert H: The CD31 molecule. A possible neuroprotective agent in acute ischemic stroke? *Thrombosis journal* 2017, 15:11.
 121. Kalinowska A, Losy J: PECAM-1, a key player in neuroinflammation. *European journal of neurology* 2006, 13:1284–1290.

122. Woodfin A, Voisin M-B, Nourshargh S: PECAM-1. A multi-functional molecule in inflammation and vascular biology. *Arteriosclerosis, Thrombosis, and Vascular Biology* 2007, 27:2514–2523.
123. Zaremba J, Losy J: sPECAM-1 in serum and CSF of acute ischaemic stroke patients. *Acta neurologica Scandinavica* 2002, 106:292–298.
124. Shen F, Degos V, Chu P-L, Han Z, Westbroek EM, Choi E-J, Marchuk D, Kim H, Lawton MT, Maze M, Young WL, Su H: Endoglin deficiency impairs stroke recovery. *Stroke* 2014, 45:2101–2106.
125. Knowland D, Arac A, Sekiguchi KJ, Hsu M, Lutz SE, Perrino J, Steinberg GK, Barres BA, Nimmerjahn A, Agalliu D: Stepwise recruitment of transcellular and paracellular pathways underlies blood-brain barrier breakdown in stroke. *Neuron* 2014, 82:603–617.
126. Gelderblom M, Leyboldt F, Steinbach K, Behrens D, Choe C-U, Siler DA, Arumugam TV, Orthey E, Gerloff C, Tolosa E, Magnus T: Temporal and spatial dynamics of cerebral immune cell accumulation in stroke. *Stroke* 2009, 40:1849–1857.
127. Kraft P, Scholtyschik K, Schuhmann MK, Kleinschnitz C: Depletion of CD11c+ Cells Does Not Influence Outcomes in Mice Subjected to Transient Middle Cerebral Artery Occlusion. *Neuroimmunomodulation* 2017, 24:123–131.
128. Mombaerts P, Iacomini J, Johnson RS, Herrup K, Tonegawa S, Papaioannou VE: RAG-1-deficient mice have no mature B and T lymphocytes. *Cell* 1992, 68:869–877.
129. Yilmaz G, Arumugam TV, Stokes KY, Granger DN: Role of T lymphocytes and interferon-gamma in ischemic stroke. *Circulation* 2006, 113:2105–2112.
130. Schuhmann MK, Langhauser F, Kraft P, Kleinschnitz C: B cells do not have a major pathophysiologic role in acute ischemic stroke in mice. *Journal of neuroinflammation* 2017, 14:112.
131. Kleinschnitz C, Kraft P, Dreykluft A, Hagedorn I, Göbel K, Schuhmann MK, Langhauser F, Helluy X, Schwarz T, Bittner S, Mayer CT, Brede M, Varallyay C, Pham M, Bendszus M, Jakob P, Magnus T, Meuth SG, Iwakura Y, Zerneck A, Sparwasser T, Nieswandt B, Stoll G, Wiendl H: Regulatory T cells are strong promoters of acute ischemic stroke in mice by inducing dysfunction of the cerebral microvasculature. *Blood* 2013, 121:679–691.
132. Kleinschnitz C, Schwab N, Kraft P, Hagedorn I, Dreykluft A, Schwarz T, Austinat M, Nieswandt B, Wiendl H, Stoll G: Early detrimental T-cell effects in experimental cerebral ischemia are neither related to adaptive immunity nor thrombus formation. *Blood* 2010, 115:3835–3842.
133. Strecker J-K, Schmidt A, Schäbitz W-R, Minnerup J: Neutrophil granulocytes in cerebral ischemia - Evolution from killers to key players. *Neurochemistry international* 2017, 107:117–126.
134. Bonaventura A, Liberale L, Vecchié A, Casula M, Carbone F, Dallegri F, Montecucco F: Update on Inflammatory Biomarkers and Treatments in Ischemic Stroke. *International journal of molecular sciences* 2016, 17.

135. Na S-Y, Mracsko E, Liesz A, Hünig T, Veltkamp R: Amplification of regulatory T cells using a CD28 superagonist reduces brain damage after ischemic stroke in mice. *Stroke* 2015, 46:212–220.
136. Anrather J, Iadecola C: Inflammation and Stroke. An Overview. *Neurotherapeutics : the journal of the American Society for Experimental NeuroTherapeutics* 2016, 13:661–670.
137. Neumann J, Riek-Burchardt M, Herz J, Doeppner TR, König R, Hütten H, Etemire E, Männ L, Klingberg A, Fischer T, Görtler MW, Heinze H-J, Reichardt P, Schraven B, Hermann DM, Reymann KG, Gunzer M: Very-late-antigen-4 (VLA-4)-mediated brain invasion by neutrophils leads to interactions with microglia, increased ischemic injury and impaired behavior in experimental stroke. *Acta neuropathologica* 2015, 129:259–277.
138. Perez-de-Puig I, Miró-Mur F, Ferrer-Ferrer M, Gelpi E, Pedragosa J, Justicia C, Urra X, Chamorro A, Planas AM: Neutrophil recruitment to the brain in mouse and human ischemic stroke. *Acta neuropathologica* 2015, 129:239–257.
139. Enzmann G, Mysiorek C, Gorina R, Cheng Y-J, Ghavampour S, Hannocks M-J, Prinz V, Dirnagl U, Endres M, Prinz M, Beschorner R, Harter PN, Mittelbronn M, Engelhardt B, Sorokin L: The neurovascular unit as a selective barrier to polymorphonuclear granulocyte (PMN) infiltration into the brain after ischemic injury. *Acta neuropathologica* 2013, 125:395–412.
140. Denk W, Strickler James H., Webb Watt W.: Two-Photon Laser Scanning Fluorescence Microscopy. *Science* 1990:73–76.
141. Göppert-Mayer M: Elementary processes with two quantum transitions. *Ann. Phys.* 2009, 18:466–479.
142. Helmchen F, Denk W: Deep tissue two-photon microscopy. *Nature methods* 2005, 2:932–940.
143. Andresen V, Alexander S, Heupel W-M, Hirschberg M, Hoffman RM, Friedl P: Infrared multiphoton microscopy: subcellular-resolved deep tissue imaging. *Current Opinion in Biotechnology* 2009:54–62.
144. Kobat D, Durst ME, Nishimura N, Wong AW, Schaffer CB, Xu C: Deep tissue multiphoton microscopy using longer wavelength excitation. *Opt. Express* 2009, 17:13354.
145. Yoder EJ, Kleinfeld D: Cortical imaging through the intact mouse skull using two-photon excitation laser scanning microscopy. *Microscopy research and technique* 2002, 56:304–305.
146. Trachtenberg JT, Chen BE, Knott GW, Feng G, Sanes JR, Welker E, Svoboda K: Long-term in vivo imaging of experience-dependent synaptic plasticity in adult cortex. *Nature* 2002, 420:788–794.
147. Richardson DS, Lichtman JW: Clarifying Tissue Clearing. *Cell* 2015, 162:246–257.
148. Orlich M, Kiefer F: A qualitative comparison of ten tissue clearing techniques. *Histology and histopathology* 2017:11903.

149. Becker K, Jährling N, Saghafi S, Dodt H-U: Immunostaining, dehydration, and clearing of mouse embryos for ultramicroscopy. *Cold Spring Harbor protocols* 2013, 2013:743–744.
150. Ertürk A, Becker K, Jährling N, Mauch CP, Hojer CD, Egen JG, Hellal F, Bradke F, Sheng M, Dodt H-U: Three-dimensional imaging of solvent-cleared organs using 3DISCO. *Nature protocols* 2012, 7:1983–1995.
151. Becker K, Jährling N, Saghafi S, Weiler R, Dodt H-U: Chemical clearing and dehydration of GFP expressing mouse brains. *PloS one* 2012, 7:e33916.
152. Ke M-T, Fujimoto S, Imai T: SeeDB. A simple and morphology-preserving optical clearing agent for neuronal circuit reconstruction. *Nature neuroscience* 2013, 16:1154–1161.
153. Meng-Tsen Ke, Satoshi Fujimoto, Takeshi Imai: SeeDB: a simple and morphology-preserving optical clearing agent for neuronal circuit reconstruction.
154. Etsuo A. Susaki, Kazuki Tainaka, Dimitri Perrin, Fumiaki Kishino, Takehiro Tawara, Tomonobu M. Watanabe, Chihiro Yokoyama, Hirotaka Onoe, Megumi Eguchi, Shun Yamaguchi, Takaya Abe, Hiroshi Kiyonari, Yoshihiro Shimizu, Atsushi Miyawaki, Hideo Yokota, Hiroki R. Ueda: Whole-Brain Imaging with Single-Cell Resolution Using Chemical Cocktails and Computational Analysis.
155. Gómez-Gaviro MV, Balaban E, Bocancea D, Lorrio MT, Pompeiano M, Desco M, Ripoll J, Vaquero JJ: Optimized CUBIC protocol for three-dimensional imaging of chicken embryos at single-cell resolution. *Development (Cambridge, England)* 2017, 144:2092–2097.
156. Susaki EA, Tainaka K, Perrin D, Kishino F, Tawara T, Watanabe TM, Yokoyama C, Onoe H, Eguchi M, Yamaguchi S, Abe T, Kiyonari H, Shimizu Y, Miyawaki A, Yokota H, Ueda HR: Whole-brain imaging with single-cell resolution using chemical cocktails and computational analysis. *Cell* 2014, 157:726–739.
157. Chung K, Deisseroth K: CLARITY for mapping the nervous system. *Nature methods* 2013, 10:508–513.
158. Chung K, Wallace J, Kim S-Y, Kalyanasundaram S, Andalman AS, Davidson TJ, Mirzabekov JJ, Zalocusky KA, Mattis J, Denisin AK, Pak S, Bernstein H, Ramakrishnan C, Grosenick L, Gradinaru V, Deisseroth K: Structural and molecular interrogation of intact biological systems. *Nature* 2013, 497:332–337.
159. Huisken J, Stainier DYR: Selective plane illumination microscopy techniques in developmental biology. *Development (Cambridge, England)* 2009, 136:1963–1975.
160. Santi PA: Light sheet fluorescence microscopy. A review. *The journal of histochemistry and cytochemistry : official journal of the Histochemistry Society* 2011, 59:129–138.
161. Voie AH, Burns DH, Spelman FA: Orthogonal-plane fluorescence optical sectioning. Three-dimensional imaging of macroscopic biological specimens. *Journal of microscopy* 1993, 170:229–236.

162. Huisken J, Swoger J, Del Bene F, Wittbrodt J, Stelzer EHK: Optical sectioning deep inside live embryos by selective plane illumination microscopy. *Science (New York, N.Y.)* 2004, 305:1007–1009.
163. Dodt H-U, Leischner U, Schierloh A, Jährling N, Mauch CP, Deininger K, Deussing JM, Eder M, Zieglgänsberger W, Becker K: Ultramicroscopy. Three-dimensional visualization of neuronal networks in the whole mouse brain. *Nature methods* 2007, 4:331–336.
164. Ernst H K Stelzer: Light-sheet fluorescence microscopy for quantitative biology.
165. Becker K, Jährling N, Saghafi S, Dodt H-U: Ultramicroscopy. Light-sheet-based microscopy for imaging centimeter-sized objects with micrometer resolution. *Cold Spring Harbor protocols* 2013, 2013:704–713.
166. Gao L, Shao L, Chen B-C, Betzig E: 3D live fluorescence imaging of cellular dynamics using Bessel beam plane illumination microscopy. *Nature protocols* 2014, 9:1083–1101.
167. Vettenburg T, Dalgarno HIC, Nylk J, Coll-Lladó C, Ferrier DEK, Čižmár T, Gunn-Moore FJ, Dholakia K: Light-sheet microscopy using an Airy beam. *Nature methods* 2014, 11:541–544.
168. Chen B-C, Legant WR, Wang K, Shao L, Milkie DE, Davidson MW, Janetopoulos C, Wu XS, Hammer JA, Liu Z, English BP, Mimori-Kiyosue Y, Romero DP, Ritter AT, Lippincott-Schwartz J, Fritz-Laylin L, Mullins RD, Mitchell DM, Bembenek JN, Reymann A-C, Böhme R, Grill SW, Wang JT, Seydoux G, Tulu US, Kiehart DP, Betzig E: Lattice light-sheet microscopy. Imaging molecules to embryos at high spatiotemporal resolution. *Science (New York, N.Y.)* 2014, 346:1257998.
169. Pierre Mahou, Julien Vermot, Emmanuel Beaurepaire, Willy Supatto: Multicolor two-photon light-sheet microscopy.
170. Bouchard MB, Voleti V, Mendes CS, Lacefield C, Grueber WB, Mann RS, Bruno RM, Hillman EMC: Swept confocally-aligned planar excitation (SCAPE) microscopy for high speed volumetric imaging of behaving organisms. *Nature photonics* 2015, 9:113–119.
171. Hu YS, Zimmerley M, Li Y, Watters R, Cang H: Single-molecule super-resolution light-sheet microscopy. *Chemphyschem : a European journal of chemical physics and physical chemistry* 2014, 15:577–586.
172. Mike Friedrich, Qiang Gan, Vladimir Ermolayev, Gregory S. Harms: STED-SPIM: Stimulated Emission Depletion Improves Sheet Illumination Microscopy Resolution.
173. Wang K, Milkie DE, Saxena A, Engerer P, Misgeld T, Bronner ME, Mumm J, Betzig E: Rapid adaptive optical recovery of optimal resolution over large volumes. *Nature methods* 2014, 11:625–628.
174. Nieswandt B, Bergmeier W, Rackebrandt K, Gessner JE, Zirngibl H: Identification of critical antigen-specific mechanisms in the development of immune thrombocytopenic purpura in mice. *Blood* 2000, 96:2520–2527.

175. Gougos A, Letarte M: Identification of a human endothelial cell antigen with monoclonal antibody 44G4 produced against a pre-B leukemic cell line. *Journal of immunology* (Baltimore, Md. : 1950) 1988, 141:1925–1933.
176. Bergmeier W, Rackebrandt K, Schröder W, Zirngibl H, Nieswandt B: Structural and functional characterization of the mouse von Willebrand factor receptor GPIb-IX with novel monoclonal antibodies. *Blood* 2000, 95:886–893.
177. May F, Hagedorn I, Pleines I, Bender M, Vögtle T, Eble J, Elvers M, Nieswandt B: CLEC-2 is an essential platelet-activating receptor in hemostasis and thrombosis. *Blood* 2009, 114:3464–3472.
178. Mombaerts P, Iacomini J, Johnson RS, Herrup K, Tonegawa S, Papaioannou VE: RAG-1-deficient mice have no mature B and T lymphocytes. *Cell* 1992, 68:869–877.
179. Sommer C, Straehle C, Kothe U, Hamprecht FA: Ilastik. Interactive learning and segmentation toolkit. Piscataway, NJ, IEEE, 2011, pp. 230–233.
180. Schindelin J, Arganda-Carreras I, Frise E, Kaynig V, Longair M, Pietzsch T, Preibisch S, Rueden C, Saalfeld S, Schmid B, Tinevez J-Y, White DJ, Hartenstein V, Eliceiri K, Tomancak P, Cardona A: Fiji. An open-source platform for biological-image analysis. *Nature methods* 2012, 9:676–682.
181. Braeuninger S, Kleinschnitz C, Nieswandt B, Stoll G: Focal cerebral ischemia. Edited by Gibbins JM, Mahaut-Smith MP. New York, Humana Pr, 2012, pp. 29–42.
182. Stegner D, vanEeuwijk JMM, Angay O, Gorelashvili MG, Semeniak D, Pinnecker J, Schmithausen P, Meyer I, Friedrich M, Dütting S, Brede C, Beilhack A, Schulze H, Nieswandt B, Heinze KG: Thrombopoiesis is spatially regulated by the bone marrow vasculature. *Nature communications* 2017, 8:127.
183. Yen JC, Chang FJ, Chang S: A new criterion for automatic multilevel thresholding. *IEEE transactions on image processing : a publication of the IEEE Signal Processing Society* 1995, 4:370–378.
184. Gorelashvili MG, Angay O, Stegner D, Heinze KG: Three-dimensional imaging and simulations of cell-vessel interactions in murine bone marrow, in preparation.
185. Rashidi NM, Scott MK, Scherf N, Krinner A, Kalchschmidt JS, Gounaris K, Selkirk ME, Roeder I, Lo Celso C: In vivo time-lapse imaging shows diverse niche engagement by quiescent and naturally activated hematopoietic stem cells. *Blood* 2014, 124:79–83.
186. Bendall L: Extracellular molecules in hematopoietic stem cell mobilisation. *International journal of hematology* 2017, 105:118–128.
187. Sauter RJ, Sauter M, Reis ES, Emschermann FN, Nording H, Ebenhöch S, Kraft P, Münzer P, Mauler M, Rheinlaender J, Madlung J, Edlich F, Schäffer TE, Meuth SG, Düerschmied D, Geisler T, Borst O, Gawaz M, Kleinschnitz C, Lambris JD, Langer HF: A Functional Relevance of the Anaphylatoxin Receptor C3aR for Platelet Function and Arterial Thrombus Formation Marks an Intersection Point Between Innate Immunity and Thrombosis. *Circulation* 2018.

188. Baeten KM, Akassoglou K: Extracellular matrix and matrix receptors in blood-brain barrier formation and stroke. *Developmental neurobiology* 2011, 71:1018–1039.
189. Clarkson BDS, Ling C, Shi Y, Harris MG, Rayasam A, Sun D, Salamat MS, Kuchroo V, Lambris JD, Sandor M, Fabry Z: T cell-derived interleukin (IL)-21 promotes brain injury following stroke in mice. *The Journal of experimental medicine* 2014, 211:595–604.
190. Gelderblom M, Gallizioli M, Ludewig P, Thom V, Arunachalam P, Rissiek B, Bernreuther C, Glatzel M, Korn T, Arumugam TV, Sedlacik J, Gerloff C, Tolosa E, Planas AM, Magnus T: IL-23 (Interleukin-23)-Producing Conventional Dendritic Cells Control the Detrimental IL-17 (Interleukin-17) Response in Stroke. *Stroke* 2018, 49:155–164.
191. Bardehle S, Krüger M, Buggenthin F, Schwausch J, Ninkovic J, Clevers H, Snippert HJ, Theis FJ, Meyer-Luehmann M, Bechmann I, Dimou L, Götz M: Live imaging of astrocyte responses to acute injury reveals selective juxtavascular proliferation. *Nature neuroscience* 2013, 16:580–586.
192. Fumagalli S, Coles JA, Ejlerskov P, Ortolano F, Bushell TJ, Brewer JM, Simoni M-G de, Dever G, Garside P, Maffia P, Carswell HV: In vivo real-time multiphoton imaging of T lymphocytes in the mouse brain after experimental stroke. *Stroke* 2011, 42:1429–1436.
193. Fumagalli S, Ortolano F, Simoni M-G de: A close look at brain dynamics. Cells and vessels seen by in vivo two-photon microscopy. *Progress in neurobiology* 2014, 121:36–54.
194. Lugo-Hernandez E, Squire A, Hagemann N, Brenzel A, Sardari M, Schlechter J, Sanchez-Mendoza EH, Gunzer M, Faissner A, Hermann DM: 3D visualization and quantification of microvessels in the whole ischemic mouse brain using solvent-based clearing and light sheet microscopy. *Journal of cerebral blood flow and metabolism : official journal of the International Society of Cerebral Blood Flow and Metabolism* 2017, 37:3355–3367.
195. Nieswandt B, Kleinschnitz C, Stoll G: Ischaemic stroke. A thrombo-inflammatory disease? *The Journal of physiology* 2011, 589:4115–4123.
196. Torsney E, Charlton R, Parums D, Collis M, Arthur HM: Inducible expression of human endoglin during inflammation and wound healing in vivo. *Inflamm. res.* 2002, 51:464–470.
197. Victora GD, Schwickert TA, Fooksman DR, Kamphorst AO, Meyer-Hermann M, Dustin ML, Nussenzweig MC: Germinal center dynamics revealed by multiphoton microscopy with a photoactivatable fluorescent reporter. *Cell* 2010, 143:592–605.
198. Arcizet D, Meier B, Sackmann E, Rädler JO, Heinrich D: Temporal analysis of active and passive transport in living cells. *Physical review letters* 2008, 101:248103.
199. Gorelashvili M, Emmert M, Hodeck KF, Heinrich D: Amoeboid migration mode adaption in quasi-3D spatial density gradients of varying lattice geometry. *New J. Phys.* 2014, 16:75012.

7 Appendix

7.1 Abbreviations

[Ca ²⁺]	intracellular calcium ion
2PM	two-photon microscopy
3D	three-dimensional
ADP	adenosine diphosphate
AF	autofluorescence
ANOVA	analysis of variance
ATP	adenosine triphosphate
BA	bone-associated
BABB	benzyl alcohol benzyl benzoate
BBB	blood brain barrier
BM	bone marrow
BW	body weight
CEACAM1	carcinoembryonic antigen-related cell adhesion molecule 1
CLEC2	C-type lectin-like receptor 2
CLH	contralateral hemisphere
CLP	common lymphoid progenitor
CMP	common myeloid progenitor
CNS	central nervous system
CSF	cerebrospinal fluid
CXCL	C-X-C-chemokine ligand
CXCR	C-X-C-chemokine receptor type
DAMPs	danger associated molecular patterns

DCs	dendritic cells
Dia	diaphysis
DMS	demarcation membrane system
dNTP	deoxynucleotide triphosphates
DTM	distance transformation map
ECM	extracellular matrix
ECs	endothelial cells
EDTA	Ethylendiaminetetraacetic acid
ELP	early lymphoid progenitor
Epi	femur epiphysis
FCS	Fetal calf serum
FGF4	fibroblast growth factor 4
FLI1	Friend leukemia integration 1 transcription factor
fps	frames per second
FXII	factor XII
G-CSF	granulocyte colony-stimulating factor
GLC	granulocyte lineage cell
GMP	granulocyte/monocyte progenitor
GPCRs	G protein-coupled receptors
GPs	glycoproteins
h	hour
HSCs	hematopoietic stem cells
I/R	ischemia reperfusion
ICAM1	intercellular adhesion molecule 1

IL	interleukin
ILH	ipsilateral hemisphere
ITAM	immunoreceptor tyrosine-based activation motif
LLC	lymphoid lineage cell
LT-HSC	long-term hematopoietic stem cell
LSFM	light sheet fluorescence microscopy
ly6G	lymphocyte antigen 6 complex locus G6D
Mac1	macrophage-1 antigen
MCA	middle cerebral artery
MEP	megakaryocyte-erythrocyte progenitors
min	minute
MIP	maximum intensity projection
MK	megakaryocytes
Mpl	myeloproliferative leukemia virus oncogene
MPP	multipotent progenitor
MSD	mean squared displacement
NAN	not a number
NBA	non-bone associated
NET	neutrophil extracellular trap
ns	non-significant
NVA	non vessel-associated
OCW	open cranial window
OPO	optical parametric oscillator
PBS	phosphate buffered saline

PEACAM1	platelet-endothelial cell adhesion molecule 1
Pf4	platelet factor 4
PFA	paraformaldehyde
Prob-EV	probability for entering the vessel lumen
PS	phosphatidylserine
PSGL1	P-selectin glycoprotein ligand 1
RBC	red blood cell
ROS	release of reactive oxygen species
rt-PA	recombinant tissue-type plasminogen activator
s	second
SCF	stem cell factor
SD	standard deviation
SDS	sodium dodecyl sulfate
Ster	sternum
ST-HSC	short-term hematopoietic stem cell
Thr	thrombus
TLRs	toll-like receptors
tMCAO	transient middle cerebral occlusion
TMR	tetramethylrhodamine
TNF	tumor necrosis factor
TPO	thrombopoietin
Treg	regulatory T cells
TTC	2,3,5-triphenyltetrazolium chloride
TxA ²	thromboxane A ₂

VA	vessel-associated
VCAM1	vascular cell adhesion molecule 1
vWF	von Willebrand factor
SDF1	stromal cell-derived factor 1
TF	tissue factor

7.2 Algorithm codes

The algorithms use the following function `isborder.m`:

```
function [x]=isborder(y,z)
if y<z+1 & y>0
    x=y;
else x=0;
end
```

7.2.1 Original algorithm code for static simulation of spatial cell distribution

The simulations were performed by defining the needed parameters and respective folders, including the template image stacks, in the matlab file `simulate.m`. `simulate.m` was built in a modular way and uses further algorithms indicated in orange color, the codes of which are presented below. All entries showed in blue represent examples. All entries in green are annotations of the code.

7.2.1.1 Simulate.m

```
for m=1:10 %number of planned simulations
    ncell=700; %number of simulated cells; ncell must be 0 modulo number of different
    cell shapes;
    numcelltemplate=20; %number of used cell templates; numbercellshape must be 0
    modulo numbercelltemplate

    cellfname1=['G:\Bibliotheken\Documents\MKSimulation\MKmigration_old\Simulation_mid
    dle\cellpool\mergedcellpool\']; %folder containing tiff image sequences of cell
    templates

    folderpath1=['G:\Bibliotheken\Documents\MKSimulation\MKmigration\StaticSimul\Simul
    ations\']; %main folder for saving simulation results
    folderpath2=['simulation_20170517_artV_realMK']; %subfolder for saving simulation
    results
    folderpath3=[' ' num2str(m) ''];
    folderpath=[folderpath1 folderpath2 folderpath3];
    mkdir(folderpath);
    numbercellshape=20; %number of different cell shapes which normally equals
    numbercelltemplate
    aXY=0.5; %voxel size in X and Y directions
    aZ=2; %voxel size in Z direction
    savesimulationdata=0; %if value 1 tiff image sequence of simulation is saved
    MKadjusted=3;

    dtfname =
    'G:\Bibliotheken\Documents\MKSimulation\MKmigration\StaticSimul\Templates\Distance
    Crop.tif';
    loadfiles
    randomcells_overlap
    clear

end
```

7.2.1.2 loadfiles.m

```

%-----
% load the distance transformation map stack
%-----
dtstack0=tiffread2(dtfname);
for k = 1:length(dtstack0)
    dtstack1=dtstack0(k);
    DTStack(:, :, k) = dtstack1.data;
end
ImStack=DTStack<=0; % 1 inside the vessel, 0 outside the vessel
[x,y,z]=ind2sub(size(DTStack), find(DTStack>0)); %coordinates of voxels outside
the vessels
D=[x,y,z]; %coordinates of voxels inside the vessel; will be changed during cell
generation->voxels outside the vessels - cells outside the vessels
clear x y z dtstack0 dtstack1 k
%%
[x,y,z]=ind2sub(size(DTStack), find(DTStack<0));
C=[x,y,z]; %coordinates of voxels inside the vessels, needed for cell at vessels
generation
clear x y z
lenX=length(DTStack(1, :, 1));
lenY=length(DTStack(:, 1, 1));
lenZ=length(DTStack(1, 1, :));
ImX=lenX; ImY=lenY; ImZ=lenZ;
ImStackMov=zeros(lenY, lenX, lenZ) ;
%%
%-----
% load the cell stacks
%-----
cellStack=[];
lencX=[];
lencY=[];
lencZ=[];
for i=1:numcelltemplate %number of different cells in the pool
    cellfname=[cellfname1 'cell' num2str(i+10) '.tif'];
    infocell = imfinfo(cellfname);
    cellStack1 = [];
    numberOfImages = length(infocell);
    for k = 1:numberOfImages
        currentImage = imread(cellfname, k, 'Info', infocell);
        cellStack1(:, :, k) = currentImage;
        cellStack1(:, :, k) = cellStack1(:, :, k)/max(max(cellStack1(:, :, k)));
    end
    [x,y,z]=ind2sub(size(cellStack1), find(cellStack1)); %positions of 1 pixels of
cell stack
    eval(['B' num2str(10+i) '(:, :, :)=x,y,z;'])
    eval(['cellStack' num2str(10+i) '(:, :, :)=cellStack1;'])
    lencX(i)=length(cellStack1(1, :, 1));
    lencY(i)=length(cellStack1(:, 1, 1));
    lencZ(i)=length(cellStack1(1, 1, :));
end
clear k currentImage info cellfname infocell x y z cellStack1 numberOfImages
currentImage cellStack i

```

7.2.1.3 randomcells_overlap.m

```

%%
%=====
% Create cells in a random way
%=====

% define the shape of each cell
randhelp3=[1:20];
randhelp1=[9 9 9 9 9 9 9 9 9 9 9 9 9 9 9 9 9 9 9 9]; %Volume distribution adjusted
randhelp2=[6 6 6 6 6 6 6 6 6 6 6 6 6 6 6 6 6 6 6 6]; % Diameter distribution
adjusted
numberofblocks=ncell/numbercellshape;
sa=[];
for i=1:numberofblocks
    if MKadjusted==1
        sa=[sa, randhelp1(randperm(20))];
    elseif MKadjusted==2
        sa=[sa, randhelp2(randperm(20))];
    else
        sa=[sa, randhelp3(randperm(20))];
    end
end
%%
%-----
% start: create a point outside the vessels
%-----
disves=nan(ncell,1);
cellstartpos0=nan(3,ncell);
for i=1:ncell
    i
    tic
    helpstartpos1=10^7; %for vessel-cell interaction; the number is here higher than
any cell volume; enables starting the while-loop
    helpstartpos2=10^7; %for cell-cell interaction; the number is here higher than
any cell volume; enables starting the while-loop
    Cint=0; %Voxel volume of the cell, which is calculated later; value 0 enables
starting the while-loop
    eval(['B=B' num2str(sa(i)+10) ';' ]);
    eval(['cellStack=cellStack' num2str(10+sa(i)) ';' ]);
    while helpstartpos1>0 || helpstartpos2>Cint*0.03 %helpstartpos=0 => start
position is found
        try
            cellstartpos0(:,i)= D(randi([1 length(D)]),:); % creates a random point in the
Vessel space

%to avoid cells outside the vessel space:
            minx=cellstartpos0(1,i);
            maxx=isborder(cellstartpos0(1,i)+lencX(sa(i))-1,ImX);
            miny=cellstartpos0(2,i);
            maxy=isborder(cellstartpos0(2,i)+lencY(sa(i))-1,ImY);
            minz=cellstartpos0(3,i);
            maxz=isborder(cellstartpos0(3,i)+lencZ(sa(i))-1,ImZ);
            if maxx==0 || maxy==0 || maxz==0 %=>cell is partially outside the stack

```

```

helpstartpos1=10^7; %for vessel-cell interaction; the number is here higher than
any cell volume
helpstartpos2=10^7; %for cell-cell interaction
else
help1=DTStack(miny:maxy,minx:maxx,minz:maxz); %part of the Vessel space
colocalizing with the cell at t=0
[x,y,z]=ind2sub(size(help1), find(help1<=0)); %finds the values larger 0 in help1
help2=[x,y,z]; %coordinates of values larger 0 in help1
help3=ImStackMov(miny:maxy,minx:maxx,minz:maxz); %part of the cell stack
colocalizing with the cell at t=0
[x,y,z]=ind2sub(size(help3), find(help3));
help4=[x,y,z]; %coordinates of values larger 0 in help3
clear x y z
helpstartpos1= sum(ismember(B(:,:,,:),help2,'rows')); %checks if vessel and cell
colocalize
helpstartpos2= sum(ismember(B(:,:,,:),help4,'rows')); %checks if cell and cell
colocalize
Cint=sum(sum(sum(cellStack))); %
end
catch
disp('error')
end
end
ImStackMov(miny:maxy,minx:maxx,minz:maxz)=ImStackMov(miny:maxy,minx:maxx,minz:maxz
)+cellStack(:,:,:).*10*i;
%build disves
cellStack1=cellStack;
cellStack1(cellStack1==0)=NaN;
helpDTStack=DTStack(miny:maxy,minx:maxx,minz:maxz).*cellStack1 ;
disves(i,1)=min(min(min(helpDTStack)));
%change D
ImStack(miny:maxy,minx:maxx,minz:maxz)=ImStack(miny:maxy,minx:maxx,minz:maxz)+ImSt
ackMov(miny:maxy,minx:maxx,minz:maxz);
[x,y,z]=ind2sub(size(ImStack), find(ImStack==0)); %positions of 1 pixels of
vessel stack
D=[x,y,z];
toc
end
%%
%-----
%save the images if needed
%-----
if savesimulationdata==1
for j=1:lenZ
outputFileName = [folderpath '\image_T1001_Z' , num2str(1000+j) ,'.tif']
imwrite(ImStackMov(:, :, j), outputFileName, 'WriteMode',
'append','Compression','none');
end
end
save([folderpath '\simulation1.mat'])

```

7.2.2 Original algorithm code for dynamic simulation of cell migration

The simulation was performed by defining the needed parameters and respective folders, where the template images were stored, in the matlab file simulate.m. simulate.m was built in a modular way and uses further algorithms indicated in orange color, the codes of which are presented below. All entries showed in blue represent examples. All entries in green are annotations of the code.

7.2.2.1 Simulate.m

```

folderpath1=['G:\Bibliotheken\Documents\MKSimulation\MKmigration\MigrationSimul\Si
mulations\20170531ctrl_3h\']; %main folder for saving the simulation results
folderpath2=['simulation_20170531_migr'];%subfolder for saving simulation results
cellfname=['G:\Bibliotheken\Documents\MKSimulation\MKmigration\MigrationSimul\Temp
lates\HSC.tif']; %tiff containing the artificial HSC image
dtfname =
'G:\Bibliotheken\Documents\MKSimulation\MKmigration\MigrationSimul\Templates\DTMKv
essel.tif'; %tiff containing the DTM of MK+Vasculature
dtfname1 =
'G:\Bibliotheken\Documents\MKSimulation\MKmigration\MigrationSimul\Templates\DTves
sel.tif'; %tiff containing the DTM of Vasculature

stepnumber=30000; %number of simulated steps

loadfiles
for m=1:200
    folderpath3=[' ' num2str(m) ''];
    folderpath=[folderpath1 folderpath2 folderpath3];
    mkdir(folderpath);
    p_walk=0.5; %probability to keep walking after vessel contact
    meanvel=3; %mean migration velocity in [ $\mu\text{m}/10 \text{ min}$ ]
    stdvel=2; %standard deviation of migration velocity in [ $\mu\text{m}/10 \text{ min}$ ]
    chemotaxis=1; %1 for chemotaxis, 0 for random walk
    chemf=0.1; %parameter for chemotaxis strength
    neededparameters
    randomcell
    Chemotaxis2
    clear ans cellcat cellpos cellstartpos0 disves disvesMKves gradx grady gradz
    help1 help2 help3 helpDTStack1 helpstartpos1 i m maxx maxy maxz minx miny minz
    stepx stepy stepz
end

```

7.2.2.2 loadfiles.m

```

%-----
% load the distance transformation map stack for vessel and cells
%-----
dtstack0=tiffread2(dtfname);
for k = 1:length(dtstack0)
    dtstack1=dtstack0(k);
    DTStack(:, :, k) = dtstack1.data;
end
[x,y,z]=ind2sub(size(DTStack), find(DTStack>0)); %coordinates of voxels outside
the vessels
D=[x,y,z]; %coordinates of voxels outside the vesselMK
clear x y z dtstack0 dtstack1 k
lenX=length(DTStack(1, :, 1));
lenY=length(DTStack(:, 1, 1));
lenZ=length(DTStack(1, 1, :));
ImX=lenX; ImY=lenY; ImZ=lenZ;
%%
%-----
% load the distance transformation map stack for vessels only
%-----
dtstack0=tiffread2(dtfname1);
for k = 1:length(dtstack0)
    dtstack1=dtstack0(k);
    DTStack1(:, :, k) = dtstack1.data;
end
clear x y z dtstack0 dtstack1 k
%%
%-----
% load the cell stacks
%-----
lencX=[];
lencY=[];
lencZ=[];
infocell = imfinfo(cellfname);
cellStack1 = [];
numberOfImages = length(infocell);
for k = 1:numberOfImages
    currentImage = imread(cellfname, k, 'Info', infocell);
    cellStack1(:, :, k) = currentImage;
    cellStack1(:, :, k) = cellStack1(:, :, k)/max(max(cellStack1(:, :, k)));
end
[x,y,z]=ind2sub(size(cellStack1), find(cellStack1)); %positions of 1 pixels of
cell stack
B11(:, :, :)= [x,y,z];
cellStack11(:, :, :)=cellStack1;
lencX=length(cellStack1(1, :, 1));
lencY=length(cellStack1(:, 1, 1));
lencZ=length(cellStack1(1, 1, :));
clear k currentImage info cellfname infocell x y z cellStack1 numberOfImages
currentImage cellStack i

```

7.2.2.3 neededparameters.m

```
%%
%=====
% needed parameters
%=====
%  $\mu\text{m}/\text{pixel}$  in X-Y plane
aXY=0.5;
%  $\mu\text{m}/\text{pixel}$  in Z plane
aZ=2;
%velocity in pixel/10min
meanvelMKxy=meanvel/aXY;
%velocity in pixel/10min
meanvelMKz=meanvel/aZ;
%velocity standard deviation in pixel/5min
stdvelMK=stdvel/aXY;
stdvelMKz=stdvel/aZ;
%experiment time, where one step corresponds to 10 min
t=[1:stepnumber];
```

7.2.2.4 randomcell.m

```
%%
B=B11;
cellStack=cellStack11;
%-----
% start: create a point outside the vessels
%-----
disves=[];
cellstartpos0=nan(3,1);
helpstartpos1=10^7; %for vessel-cell interaction; the number is here higher than
any cell volume; enables starting the while-loop
while helpstartpos1>0 %helpstartpos=0 => start position is found
try
cellstartpos0(:)= D(randi([1 length(D)]),:); % creates a random point in the
Vessel space
%to avoid cells outside the vessel space:
minx=cellstartpos0(1);
maxx=isborder(cellstartpos0(1)+lencX-1,ImX);
miny=cellstartpos0(2);
maxy=isborder(cellstartpos0(2)+lencY-1,ImY);
minz=cellstartpos0(3);
maxz=isborder(cellstartpos0(3)+lencZ-1,ImZ);
if maxx==0 || maxy==0 || maxz==0 %=>cell is partially outside the stack
helpstartpos1=10^7; %for vessel-cell interaction; the number is here higher than
any cell volume
helpstartpos2=10^7; %for cell-cell interaction
else
help1=DTStack1(miny:maxy,minx:maxx,minz:maxz); %part of the VesselMK space
colocalizing with the cell at t=0
[x,y,z]=ind2sub(size(help1), find(help1==0)); %finds zeros
help2=[x,y,z]; %coordinates of values larger 0 in help1
clear x y z
helpstartpos1= sum(ismember(B(:,:,,:),help2,'rows')); %checks if vessel and cell
colocalize
end
```



```

catch
disp('error')
end
end
%build disves
cellStack1=cellStack;
cellStack1(cellStack1==0)=NaN;
helpDTStack1=DTStack1(miny:maxy,minx:maxx,minz:maxz).*cellStack1 ;
disves(1)=min(min(min(helpDTStack1)));

```

7.2.2.5 Chemotaxis2.m

```

%%
%=====
% cell migration
%=====
cellpos=zeros(3,length(t));
cellpos(:,1)=cellstartpos0;
cellcat(1)=0;% >0 if releasing pp, 0 if moving
for i=2:max(t)
if cellcat(i-1)==0
cellcat(i)=0;
B=B11;
cellStack=cellStack11;
stepx=normrnd(meanvelMKxy,stdvelMK)*(-1+2*(rand>.5));
stepy=normrnd(meanvelMKxy,stdvelMK)*(-1+2*(rand>.5));
stepz=normrnd(meanvelMKz,stdvelMK)*(-1+2*(rand>.5));
gradx=(DTStack1(cellpos(1,i-1)+lencX)-DTStack1(cellpos(1,i-1)))*chemf;
grady=(DTStack1(cellpos(2,i-1)+lencY)-DTStack1(cellpos(2,i-1)))*chemf;
gradz=(DTStack1(cellpos(3,i-1)+lencZ)-DTStack1(cellpos(3,i-1)))*chemf;
cellpos(1,i)=ceil(cellpos(1,i-1)+stepx+gradx);
cellpos(2,i)=ceil(cellpos(2,i-1)+stepy+grady);
cellpos(3,i)=ceil(cellpos(3,i-1)+stepz+gradz);
minx=cellpos(1,i);
maxx=isborder(cellpos(1,i)+lencX-1,ImX);
miny=cellpos(2,i);
maxy=isborder(cellpos(2,i)+lencY-1,ImY);
minz=cellpos(3,i);
maxz=isborder(cellpos(3,i)+lencZ-1,ImZ);
if maxx==0 | maxy==0 | maxz==0 | minx<1 | miny<1 | minz<1
cellpos(:,i)=cellpos(:,i-1);
disves(i)=disves(i-1);
else
cellStack1=cellStack;
cellStack1(cellStack1==0)=NaN;
help1=DTStack(miny:maxy,minx:maxx,minz:maxz).*cellStack1; %for MK_VESSEL
help3=DTStack1(miny:maxy,minx:maxx,minz:maxz).*cellStack1;
disves(i)=min(min(min(help3)));
disvesMKves(i)=min(min(min(help1)));
if disvesMKves(i)==0 && disves(i)>0 %if cell meets MK
cellpos(:,i)=cellpos(:,i-1) ; %move the cell to the last position
disves(i)=disves(i-1);
elseif disvesMKves(i)==0 && disves(i)==0 %if the cell meets a vessel
cellcat(i)=probstop(p_walk); %probability to keep walking
end

```

```
end
elseif cellcat(i-1)==1
cellpos(:,i)=cellpos(:,i-1);
disves(i)=disves(i-1);
cellcat(i)=1;
end
end
save([folderpath '\simulation1.mat'], 'aXY', 'aZ', 'cellcat', 'cellpos', 'chemf',
'chemotaxis', 'disves', 'm', 'meanvelMKxy', 'meanvelMKz', 'meanvel', 'p_walk',
'stdvel', 'stdvelMK', 'stdvelMKz', 'stepnumber')
```

7.3 Acknowledgements

The present work was accomplished in the group of Dr. David Stegner at the Institute of Experimental Biomedicine, Department I, University Hospital Würzburg. Throughout the period of my work on the thesis (2014-2018), many people supported and helped me, whom I would like to thank:

My primary supervisor, Dr. David Stegner, for giving me the opportunity to work in his group, for his courage, trust, guidance, constant support and valuable discussions.

My secondary supervisor, Prof. Dr. Katrin Heinze, for her constant support, fruitful discussions and great scientific ideas.

My supervisor, Prof. Dr. Guido Stoll, for his support, for giving the insight into clinical research and for fruitful discussions.

My supervisor, Prof. Dr. Bernhard Nieswandt, for helpful suggestions, critical input and, of course, for giving me the opportunity to work at the institute for experimental biomedicine.

Dr. Michael Schuhmann and Oguzhan Angay for fruitful collaboration, their support and valuable contributions.

Dr. Dr. Katharina Remer for critical input, valuable discussions and for her help as a veterinarian.

The Bio-Imaging Center of the RVZ for providing the microscopes and technical support. I would like to particularly thank Jürgen Pinnecker for his brilliant ideas and for constantly improving the light sheet fluorescence microscopes.

The research assistants, Dominik Köck, Patrick Schmitthausen, Thomas Müller and Jan-Hagen Krohn, for their help to perform image processing.

The technicians and animal caretakers, especially Stefanie Hartmann, Eva Stepien-Bötsch and Richard Taylor, for their excellent technical assistance.

The secretaries, Kerstin Siegmann and Elke Hauk, for their organizational support.

The Graduate School of Life sciences for providing the opportunity to take part in the transferable skills program and for enabling me to participate in different international conferences.

All current and former members of the institute for the unique working atmosphere, for their help and shearing their knowledge. I would like to thank Judith van Eeuwijk for teaching me much about biology and the fruitful collaboration. I also thank Katharina, Inga, Vanessa, Sarah for carefully proofreading the manuscript.

My current colleagues at Zeiss Microscopy GmbH, especially Dr. Yilmaz Niyaz, who have supported and encouraged me to finalize the thesis.

Last but not least, I am more than grateful to all of my friends for supporting and encouraging me since many years and for always standing by my side. I would like to particularly thank Johannes, Reinhard, Eva, Birgit, Antonia and Clara.

7.4 Publications

7.4.1 Original articles

„Three-dimensional imaging and simulations of cell-vessel interactions in murine bone marrow“, **M. Gorelashvili**, O.Angay, D. Stegner, K.G. Heinze, in preparation.

„Thrombopoiesis is spatially regulated by the bone marrow vasculature“, D. Stegner, J. van Eeuwijk, O. Angay, **M. Gorelashvili**, D. Semeniak, J. Pinnecker, P. Schmithausen, I. Meyer, M. Friedrich, S. Dütting, C. Brede, A. Beilhack, H. Schulze, B. Nieswandt, K. Heinze, *Nat. Comm.* 8:127 (2017)

„A Cdc42/RhoA regulatory circuit downstream of glycoprotein Ib guides transendothelial platelet biogenesis“, S. Dütting, F. Gaits-Iacovoni, D.Stegner, M.Popp, A. Antkowiak, J. van Eeuwijk, P. Nurden, S. Stritt, T. Heib, K. Aurbach, O. Angay, D. Cherpokova, N. Heinz, A. A. Baig, **M. Gorelashvili**, F. Gerner, K. Heinze, J. Ware, G. Krohne⁷, Z. Ruggeri, A. T. Nurden, H. Schulze, U. Modlich, I. Pleines, C. Brakebusch, B. Nieswandt, *Nat. Comm.* 8:15838 (2017)

7.4.2 Oral presentations

“Light sheet fluorescence microscopy (LSFM) and subsequent quantitative structural analysis of megakaryocytes in intact murine bone”. ECTH: European Congress on Thrombosis and Hemostasis, The Hague, The Netherlands. September 2016.

Oral presentation with distinction

7.4.3 Poster presentations

“Light Sheet Fluorescence Microscopy (LSFM) and subsequent quantitative structural analysis of intact murine bone”. EMBO/EMBL symposium „Seeing is Believing - Imaging the Processes of Life“, Heidelberg, Germany. October 2015.

“Light-microscopic analyses of cellular interactions in the ischemic brain”. 9th international Symposium “Eureka!”, Würzburg, Germany. October 2014.

7.5 Curriculum vitae

Name: Maximilian Georg Gorelashvili
 Address: Seestraße 14, 89522 Heidenheim (Germany)
 Phone: +49 178 467 8485
 E-Mail: m.gorelashvili@outlook.com
 Date of birth: 09.07.1987 (Kutaisi, Georgia)

Experience

02/2018 to present **Application specialist for light microscopy**
 Carl Zeiss Microscopy GmbH, Zeiss Microscopy Customer Center Europe (Oberkochen, Germany)
 04/2014-12/2017 **Research assistant**
 University hospital Würzburg and Institute of experimental biomedicine (University of Würzburg)

Education

10/2014 to present **Doctoral studies**
 University of Würzburg, Graduate School of Life Sciences
 Focus of the studies: vascular medicine, fluorescence microscopy
 Title of the thesis: „Investigation of megakaryopoiesis and the acute phase of ischemic stroke by advanced fluorescence microscopy“
 Supervisors: Dr. David Stegner, Prof. Dr. Katrin Heinze
 10/2011-04/2014 **Physics (Master of Science)**
 Ludwig-Maximilians University Munich. Final grade: 1.6
 Master thesis: „Cell migration strategies and cellular force generation in quasi 3D pillar arrays“; Supervisor: Prof. Dr. Erich Sackmann (TU München) and Prof. Dr. Doris Heinrich (LMU München)
 10/2007-10/2011 **Physics (Bachelor of Science)**
 Ludwig-Maximilians University Munich. Final grade: 2.8
 Bachelor thesis: „Uptake and transport of magnetic particles in living cells“; Supervisor: Prof. Dr. Doris Heinrich (LMU München)
 02/2002-06/2006 **Higher School Certificate**
 Maria-Theresia grammar school, Munich. Final grade: 1.3
 09/1993-09/2001 Classical grammar school Kutaisi (Georgia), Final grade: 1.0

Würzburg, June 2018

Maximilian Georg Gorelashvili

Affidavit

I hereby declare that my thesis, entitled “Investigation of megakaryopoiesis and the acute phase of ischemic stroke by advanced fluorescence microscopy”, is the result of my own work. I did not receive any help or support from commercial consultants. All sources and/or materials applied are listed and specified in the thesis.

Furthermore, I confirm that this thesis has not yet been submitted as part of another examination process neither in identical nor in similar form.

Heidenheim, June 2018

Maximilian Georg Gorelashvili

Eidesstaatliche Erklärung

Hiermit erkläre ich an Eides statt, die Dissertation “Untersuchungen der Megakaryopoese und der akuten Phase des ischämischen Schlaganfalls” eigenständig, d.h. insbesondere selbstständig und ohne Hilfe eines kommerziellen Promotionsberaters, angefertigt und keine anderen als die von mir angegebenen Quellen und Hilfsmittel verwendet zu haben.

Ich erkläre außerdem, dass die Dissertation weder in gleicher noch in ähnlicher Form bereits in einem anderen Prüfungsverfahren vorgelegen hat.

Heidenheim, Juni 2018

Maximilian Georg Gorelashvili